Doctoral theses at NTNU, 2023:280

Kittinat Taweesintananon

Distributed Acoustic Sensing and 4D Seismic Time-Strain Inversion for Subsurface Monitoring

Doctoral thesis

NTNU
Norwegian University of Science and Technology
Thesis for the Degree of
Philosophiae Doctor
Faculty of Information Technology and Electrical Engineering
Department of Electronic Systems

NTNU
Norwegian University of
Science and Technology

Kittinat Taweesintananon

Distributed Acoustic Sensing and 4D Seismic Time-Strain Inversion for Subsurface Monitoring

Thesis for the Degree of Philosophiae Doctor

Trondheim, September 2023

Norwegian University of Science and Technology
Faculty of Information Technology and Electrical Engineering
Department of Electronic Systems

NTNU
Norwegian University of
Science and Technology

NTNU
Norwegian University of Science and Technology

Thesis for the Degree of Philosophiae Doctor

Faculty of Information Technology and Electrical Engineering
Department of Electronic Systems

ISBN 978-82-326-7260-8 (printed ver.)
ISBN 978-82-326-7259-2 (electronic ver.)
ISSN 1503-8181 (printed ver.)
ISSN 2703-8084 (online ver.)

Doctoral theses at NTNU, 2023:280

Printed by NTNU Grafisk senter

Abstract

Subsurface monitoring plays an important role in utilising subsurface resources and preventing geologic hazards. This thesis comprises dissemination of the research in using seismic methods for subsurface monitoring. Here I demonstrate various applications of ocean-bottom fibre-optic distributed acoustic sensing (DAS) technology to marine seismic exploration and subsurface monitoring using active and passive seismic sources. These include conventional marine seismic sources, whale vocalisations and subsurface shear-wave resonance. In addition, I develop a new time-lapse (4D) seismic method based on traveltime, called "4D seismic time-strain inversion," to monitor the time-lapse changes in geophysical properties of the subsurface. This method can determine the subsurface changes without prior knowledge nor assumption about geomechanical properties in the field of interest. All the research work done in this thesis could contribute to the advancement of fibre-optic DAS and 4D seismic technologies for subsurface monitoring.

Sammendrag

Undergrunns overvåking spiller en viktig rolle i utnytting av ressurser under overflaten og for å forhindre geologiske farer. Denne oppgaven inneholder forskningen på bruk av seismiske metoder for overvåking av undergrunnen. Her demonstrerer jeg ulike anvendelser av havbunns fiber-optisk distribuert akustisk sensing (DAS) teknologi til marin seismisk utforskning og undergrunns overvåking ved bruk av aktive og passive seismiske kilder. Dette inkluderer konvensjonelle marine seismiske kilder, hvalvokaliseringer og undergrunns skjærbølgeresonans. I tillegg, utvikler jeg en ny 4D-seismikk metode basert på reisetid, kalt "4D seismic time-strain inversion," for å overvåke tidsforløp endringene i geofysiske egenskaper til undergrunnen. Denne metoden kan bestemme endringer i undergrunnen uten noen forkunnskaper, eller antakelser, om de geomekaniske egenskapene til feltet av interesse. Alt forskningsarbeidet som er gjort i denne oppgaven kan bidra til å fremme fiber-optiske DAS og 4D-seismiske teknologier for undergrunns overvåking.

Acknowledgements

This PhD thesis is a collection of my research that was conducted at the Acoustics Group, Department of Electronic Systems, Faculty of Information Technology and Electrical Engineering, Norwegian University of Science and Technology (NTNU), from February 2020 to March 2023. The research was conducted under the supervision of Professor Martin Landrø (NTNU), and the co-supervision of Professor Børge Arntsen (NTNU). The work was funded by the Research Council of Norway (RCN) and the sponsors of the Geophysics and Applied Mathematics in Exploration and Safe production Project (GAMES; RCN grant no. 294404), and the SFI Centre for Geophysical Forecasting (CGF; RCN grant no. 309960). In addition, I received financial support from PTT Exploration and Production Public Company Limited (PTTEP) to pursue the PhD at NTNU.

The research was conducted in collaboration with many people, who deserve acknowledgements from me. I would like to express my deepest appreciation to my supervisor, Professor Martin Landrø (NTNU), for his invaluable patience, feedback and guidance on conducting good scientific research. I am extremely grateful to the PhD programme and defence committee, who generously provide expertise and feedback. This endeavour would not have been possible without the support from all the aforementioned funders, especially PTTEP, my employer, who allowed me to pursue the PhD at NTNU.

I am also grateful to my cohort members at the Acoustics Group and CGF for their academic discussion, entertainment activities, and generous support. Many thanks to all the co-authors and reviewers of my research dissemination included in this thesis for their constructive feedback, discussion and contributions. Special thanks to the following high-impact contributors: Jan Kristoffer Brenne (Alcatel Submarine Networks, Inc.) for Paper I; Léa Bouffaut (Cornell University, USA) for Paper II; Professor John Robert Potter (NTNU) and Ethan F. Williams (University of Washington, USA) for Paper III; Sirikarn Narongsirikul (ConocoPhillips Norge) and Per Gunnar Folstad (ConocoPhillips Norge) for Paper IV. Thanks should also go to Robin André Rørstadbotnen, Umedzhon Kakhkhorov and many other classmates at NTNU for entertainment and moral support.

Lastly, I would be remiss in not mentioning my family: my parents for their invaluable support in developing my education and lifelong learning attitudes; my spouse for always giving me moral support and making my life easier; and my child for arriving to the family.

Contents

Figures

Acronyms

CGF SFI Centre for Geophysical Forecasting. vii, xv, 17

DAS distributed acoustic sensing. iii, v, 1, 3–5, 7–10, 17–22, 25–27, 29, 41, 61, 77

HDF5 Hierarchical Data Format 5. 10, 11

NMO normal move-out. 22

NTNU Norwegian University of Science and Technology. vii, xv, 17

OSGW ocean surface gravity wave. 7, 21

PhD philosophiae doctor. vii, 17

PTTEP PTT Exploration and Production Public Company Limited. vii, 17

RCN Research Council of Norway. vii, xv, 17

SFI sentre for forskningsdrevet innovasjon. vii, xiii, xv, 17

SNR signal-to-noise ratio. 8

VTI vertical transverse isotropic. 19, 22, 27, 95

Glossary

SFI Centre for Geophysical Forecasting The SFI Centre for Geophysical Forecasting (CGF) is a joint enterprise funded by the Research Council of Norway (RCN), industrial partners and Norwegian University of Science and Technology (NTNU). It is a Research-based Innovation Centre (sentre for forskningsdrevet innovasjon (SFI)), selected by the RCN for support in June 2020 and opening in December 2020. vii, xiii, xv, 17

4D seismic Time-lapse seismic (also called four-dimensional (4D) seismic) is referred to as the method in which a seismic survey is repeated over a given area in order to monitor subsurface changes caused by petroleum production, CO_2 injection, etc. Time is the fourth dimension of 4D seismic data. iii, v, 1, 4, 5, 11–15, 19, 22, 27, 29, 30, 95

Chapter 1

Introduction

1.1 Motivation

Subsurface monitoring is an application of geophysics. It is used to investigate the changes under the solid surface of the earth. Therefore, subsurface monitoring plays an important role in utilising subsurface resources and preventing geologic hazards. It also plays an important role in serving society and achieving the 17 United Nations (UN) Sustainable Development Goals (SDGs) [1].

For decades, subsurface monitoring has been conducted extensively in mining and petroleum exploration industry to improve the efficiency in production. In recent years, it has also become engaged in hydrogen and CO_2 storage, enhanced petroleum recovery, geothermal resource management, underground water resource management, nuclear waste disposal management, and many other near-surface investigations.

Subsurface monitoring can be done by using geophysical tools such as well logging tools, downhole monitoring tools, subsurface fluid sampling, tracer analysis, seismic imaging methods, high-precision gravity methods, or electrical techniques. Typically, the main purposes are to track the movement and pathways of fluids through subsurface reservoirs, to track associated pressure changes and other physical property changes in the reservoirs, and to define the reservoir boundaries.

This thesis focuses on the use of seismic methods for subsurface monitoring. Here, I demonstrate various applications of fibre-optic distributed acoustic sensing (DAS) to marine seismic exploration, which is the basis of subsurface monitoring. In addition, I develop a method that uses the traveltimes in time-lapse seismic data to monitor subsurface changes. This method is called "4D seismic time-strain inversion."

1.2 Literature Review

1.2.1 Marine seismic exploration

Near-surface seismic imaging is essential for investigating shallow gas, weak layers, faults, and other potential subsurface geological hazards. These elements can adversely affect offshore activities such as drilling operations, offshore platform and wind farm construction, and pipeline surveys. The oil and gas industry uses near-surface information to improve the images of deeper structures and to reduce risks in exploration and production. To accurately investigate near-surface irregularities, ultrahigh-resolution reflection seismic data acquisition and processing techniques have been developed [2].

Marine seismic data can be recorded either by hydrophone streamers towed behind sailing vessels or by seismic receivers deployed on the seafloor. Seismic reflections from near-surface structures are strongest at the receivers with short offsets from the source. To acquire near-offset seismic data, we may place the source over the streamer spread, which requires separate vessels for sources and streamers [3]. Another solution is to minimise the distance between sources and dense streamers [2, 4]. However, the latter solution requires shortening the streamer length for operation safety. The lack of far offset information consequently causes high uncertainty in velocity model building. On the other hand, short offsets and dense receiver spacing in streamers result in high stacking fold and narrow imaging bins for near-surface imaging. Hence, when combined with high-frequency seismic sources, the vertical and horizontal resolution becomes significantly higher than conventional broadband seismic data.

Seabed seismic acquisition has been growing in the marine seismic market for its advantages over towed streamer techniques. The physics of seabed seismic acquisition is more advantageous than towed streamer acquisition for the following reasons [5]. First, seafloor receivers have lower noise level than towed streamers. Second, there are no limits to the offsets and azimuths between sources and receivers, except for source-vessel considerations. Long offsets and wide azimuths in the data can significantly improve the accuracy of seismic velocity models and the seismic illumination of complex structures. Third, pressure and shear waves are both recorded, so a seafloor receiver geometry can provide high-quality images even in areas with strong amplitude absorption in the presence of gas. Finally, there are fewer effects from the sea surface ghosts that limit the frequency bandwidth of the seismic data and, hence, the image resolution.

Ocean bottom cables and ocean bottom nodes are common recording systems in the seabed seismic market. The node system is a blind recording system, as it acquires data internally and exports the data later. In addition, nodes are powered by internal batteries which requires an effective power management plan during the operation. In contrast, data recorded by ocean bottom cables can be viewed on a real-time basis. Traditional cable systems for seabed seismic acquisition are bulky electronic networks. However, the electrical cables can be replaced with fibre-optic sensing cables, while maintaining the recording performance [6]. In addition to

the real-time monitoring feature, a key advantage of fibre-optic sensing systems is that no electronic and electrical power components are required at the sensing points giving unsurpassed reliability for permanently installed sensing systems.

1.2.2 Distributed acoustic sensing for subsurface exploration

Distributed acoustic sensing (DAS) is a technology that uses fibre-optic cables for acoustic measurements. It has been applied to military defence, engineering structure monitoring and petroleum exploration [7]. DAS transforms a fibre-optic cable into a densely sampled sensor array. The cable itself is the sensing element without additional transducers in the optical path. Laser pulses transmitted into the fibre are continuously reflected to the interrogator due to the Rayleigh backscattering process inherent to all optical fibres. The phase of the backscattered light is reconstructed within the interrogator typically for each meter of the fibre. As the phase of the reflected optical light is proportional to the strain of the fibre, the distributed strain modulation across a fibre segment (termed the gauge length) can be computed. Therefore, DAS can sense seismic waves that modulate the extensional strain of the fibre segment [8]. Its seismic response is somewhat similar to the inline component of conventional point accelerometers. In other words, it is mainly sensitive to seismic waves creating strain along the cable direction [9, 10].

Over the past decade, many applications of DAS have been studied and introduced to the applied seismology community and the petroleum industry. Daley *et al.* [11] demonstrate a field test of DAS seismic acquisition of borehole seismic data and land surface seismic data. Additionally, Dean *et al.* [12] discuss its applications to marine seismic acquisition. Lumens [13] studies various applications of DAS in oil and gas wells. In addition to borehole applications, DAS can be applied to fibre-optic telecommunication cables deployed on the ground and seafloor. Many case studies of DAS using onshore telecommunication infrastructure have been conducted for passive seismic monitoring such as earthquake detection [14–17], near-surface soil studies [18, 19], ambient noise analysis [20–22], urban traffic monitoring [23, 24], glacier flow monitoring [25], and other seismic activities [26]. Moreover, it can monitor seismic waves from controlled sources to study and prevent onshore geohazards [27]. In addition to onshore environments, DAS in subsea fibre-optic telecommunication cables can detect ocean waves, microseisms, earthquakes [28, 29], and near-surface geological structures and faults [30].

DAS can be used as surface seismic receivers in subsurface exploration. Bakulin *et al.* [31] and Urosevic *et al.* [32] demonstrate the potential applications of DAS to land seismic exploration. A comprehensive review of the recent DAS technology for land surface seismic surveys is given in Bakulin *et al.* [33]. Nevertheless, the applications of DAS to produce subsurface seismic images in a marine environment have not been widely presented. It is important to acquire manifold and diverse examples to verify that DAS can be used for subsurface seismic explor-

ation in any environment. This statement could be demonstrated by comparing the marine seismic images from DAS with those from other conventional seismic methods. The validity of DAS in marine seismic exploration has the potential in the seabed seismic market.

1.2.3 4D seismic methods for subsurface monitoring

Time-lapse (also called 4D) seismic analysis has evolved as an essential integrity of subsurface reservoir management in many regions since the early 1990s. In the petroleum industry, 4D seismic is employed as a primary surveillance tool to optimise the field-development plan and to improve energy efficiency in operation and production. It is the process of using two or more seismic surveys acquired in the same area to find changes that occur over time [5]. Subsurface changes due to petroleum production or fluid substitution cause different responses of amplitude and traveltime in the seismic data acquired at different times. The 4D seismic responses are well depicted in Chadwick *et al.* [34, Figure 1] and Landrø [35, Figure 19.6].

Most 4D seismic time-shifts are measured from a pair of successive poststack seismic volumes (baseline and monitor data) on a trace-by-trace basis using cross-correlation methods [36] or nonlinear inversion [37]. It is important to measure poststack time-shifts both inside and outside reservoirs. A significant observation of the time-shifts up to 20 ms caused by the overburden stretching above compacting reservoirs was reported at Ekofisk, where the seabed was sinking for a few meters [38]. The subsidence of the seabed and the subsurface layers could cause instability to the production platforms and other facilities attached to the seabed, which is an element of hazards. Therefore, 4D seismic time-shift analysis can play an important role in hazard management and field operation. Moreover, 4D seismic time-shifts are a robust and stable seismic attribute effectively used to evaluate reservoir dynamics due to production [39].

4D seismic time-shifts are on the spot, because seismic interpretations are done in the time domain of the seismic volumes, all of which have been migrated with one common velocity model. Time-shift analysis using one common velocity model in seismic migration is widely performed, because it has a lower computational cost and less uncertainty than migrating each of the seismic volumes with its individually-updated velocity model [39]. Although data-fitting velocity modelling methods such as 4D full-waveform inversion can possibly provide high-resolution estimates of the 4D change, they are computationally expensive and subject to improvement on reducing artefacts caused by non-repeatability of the survey [40].

1.3 Aim of the Thesis

This thesis aims to demonstrate the use of fibre-optic DAS technology for subsurface seismic exploration and monitoring in marine environment. The thesis

also aims to develop and demonstrate a new traveltime-based 4D seismic method for subsurface monitoring. These two demonstrations could contribute to the advancement of fibre-optic sensing technology and to the development of the scientific knowledge of subsurface monitoring.

1.4 Structure of the Thesis

This thesis is a collection of research articles. It is designed and written in such a way that it presents the overall coherence of all the articles and situates their results in the wider context.

Chapter 2 covers the necessary background that forms the methodological and theoretical framework of the thesis. It serves as the introductory chapter for the newcomers to the research areas of fibre-optic sensing and subsurface monitoring.

Chapter 3 sums up and integrates the contribution of the thesis as a whole.

Chapter 4 thoroughly discusses the contribution of the thesis as a whole.

Chapter 5 draws the overall conclusion of the thesis. It also presents an outlook of the research and development of fibre-optic DAS for subsurface monitoring.

Chapter 2

Background

2.1 Fibre-Optic Distributed Acoustic Sensing

2.1.1 Ocean-bottom distributed acoustic sensing

Distributed acoustic sensing (DAS) is a technology that can exploit the optical fibre in standard telecommunication cables as an extended spatial array of acoustic sensors [8]. Over 1.3 million kilometres of subsea telecommunication cables have been deployed around the Earth. Many optical fibres in these cables, often 'spares', are not currently used for telecommunication. It is possible to repurpose these unused 'dark' fibres to serve as ocean-bottom distributed acoustic sensors to measure, among other signals, dynamic strains caused by ocean-bottom pressure fluctuations. DAS measures the strain fluctuations at each sensing element of an optical fibre. A DAS interrogator can measure the strain data along the fibre with a length up to 171 km in a controlled experiment [41]. In addition, DAS measures data with a spatial sampling interval of as little as 1 m, which creates arrays of many tens of thousands of sensors at relatively low cost.

DAS in subsea fibre-optic telecommunication cables can measure pressure fluctuations at the ocean bottom, originating from a variety of sources [42]. DAS in ocean-bottom fibre-optic cables can also detect ocean surface gravity wave (OSGW)'s, microseisms and earthquakes [28, 30]. Furthermore, Williams *et al.* [29] demonstrate that DAS can record the seismic waves from a distant earthquake, OSGW, and Scholte waves.

The strain of a fibre section is a function of its particle motion along the fibre [43]. Based on Newton's second law of motion, the particle acceleration along the fibre can be induced by the force endowed with the pressure changes with distance (i.e., a pressure gradient) along the fibre [44, Chapter 10]. Based on Hooke's law in elastic media, the strain of the fibre section is proportional to that component of the pressure gradient projected along the direction of the fibre [45, Chapter 1]. The transfer function between seafloor displacements and pressure fields associated with OSGWs, which is called the seafloor compliance, is discussed in Crawford *et al.* [46]. Therefore, pressure changes in space and time are detect-

able by DAS at the seafloor, providing they cause strains above the detection limit (due to noise) in the order of 1 nε (nano-strain unit).

2.1.2 Principle of DAS measurement

Most DAS systems are based on phase-sensitive optical time domain reflectometry (φ-OTDR), because the phase change in Rayleigh backscattered light has a linear relationship with the strains of the optical fibre in response to the acoustic wave [8]. Typically, a DAS system uses a single-mode fibre as the sensing fibre. In this thesis, we use this type of fibre in standard subsea fibre-optic telecommunication cables for DAS measurement. However, the Rayleigh backscattered light in this type of fibre could be weak resulting in poor signal-to-noise ratio (SNR). The improvement of the SNR of DAS measurement is an ongoing research topic, which is beyond the scope of this thesis.

To perform DAS measurement, we connect one end of an optical fibre to a DAS interrogator. The interrogation is performed by sending frequency swept light pulses into the sensing fibre which are backscattered at inherent anomalies from the whole fibre length due to Rayleigh backscattering. The interrogator measures the time differentiated phase change of the backscattered response from one sweep for each sampled fibre position (see Figure 2.1).

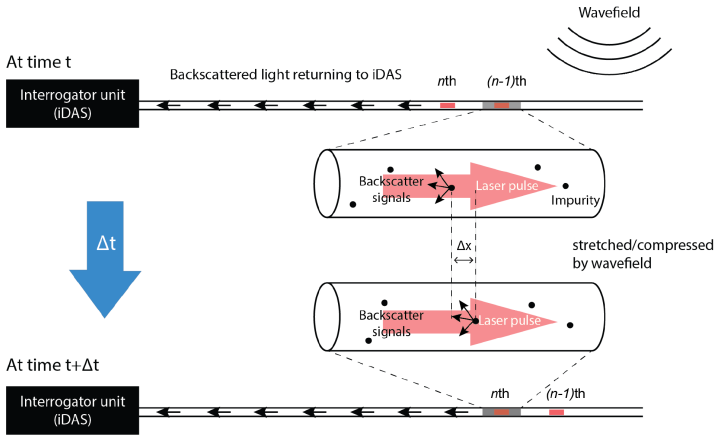

Figure 2.1: Principle of DAS. Rayleigh backscattering occurs at anomalies in the optical fibre which can be shifted by the surrounding wavefield. The phase changes of successive pulses are recorded by the DAS interrogator (retrieved from [26]).

The phase of a backscattered light pulse travelling in a fibre section is defined in radians as

$$\phi = 2\pi\left(\frac{L_o}{\lambda_o}\right), \tag{2.1}$$

where L_o and λ_o are the two-way optical travel-distance and the wavelength of

the light pulse in free space (vacuum), respectively.

We recall that the refractive group index n_g of an optical medium is defined as the ratio of the speed of light in vacuum to that in the medium:

$$n_g \equiv \frac{c}{v_{\text{ph}}} = \frac{L_o}{L}\,, \tag{2.2}$$

where c is the speed of light in vacuum, v_{ph} is the speed of light in the fibre, and L is the two-way travel-distance of the light in the fibre. Given x is the length of the fibre section associated with the two-way travel-distance L, we can write $L \approx 2x$. Here, we neglect the fibre birefringence and consider a linearly polarised beam. Hence,

$$L_o \approx 2n_g x = 2\left(\frac{c}{v_{\text{ph}}}\right)x\,, \tag{2.3}$$

We see from Equation (2.1) that a phase change is fundamentally caused by an optical path change in vacuum. Given the light with a constant wavelength λ_o in vacuum, we derive the phase change across the gauge length ($x = L_G$) from Equation (2.1) and rearrange it with Equation (2.3) as follows:

$$\Delta\phi = \frac{2\pi}{\lambda_o}\Delta L_o \approx \frac{4\pi n_g L_G}{\lambda_o}\left(\frac{\Delta L_o}{L_o}\right). \tag{2.4}$$

Therefore, the phase change of the light travelling across the gauge length L_G in a optical fibre is proportional to the relative change in the optical path length in vacuum.

From Equation (2.3), we derive the relative change in the optical path length in vacuum as

$$\frac{\Delta L_o}{L_o} \approx \varepsilon_{xx} - \frac{\Delta v_{\text{ph}}}{v_{\text{ph}}}\,, \tag{2.5}$$

where $\varepsilon_{xx} \equiv \Delta x/x$ is the longitudinal strain of the fibre section across the gauge length. Here, Equation (2.5) implies that the change in the optical path length in vacuum is caused by the changes in either the physical length of the fibre or the speed of light in the fibre.

Because the phase velocity of light depends on the dielectric tensor of the fibre, Equation (2.5) for a uniform and isotropic material can be described by the Pockel photoelastic constants (P_{11}, P_{12} and P_{44}) as follows [9, 47].

$$\frac{\Delta L_o}{L_o} = \varepsilon_{xx} - \frac{n_g^2}{2}\left[\left(P_{11} - P_{44}\right)\varepsilon_\perp + P_{12}\varepsilon_{xx}\right], \tag{2.6}$$

where $\varepsilon_\perp$ is the transverse fibre strain, and $P_{12} = P_{11} - 2P_{44}$. This equation implies that the DAS signal based on a phase change method is caused by either the longitudinal strain ε_{xx} or the transverse strain $\varepsilon_\perp$ of the fibre section.

For very small transverse stress ($\sigma_\perp \to 0$) in the optical fibre, the transverse strain $\varepsilon_\perp$ depends on the longitudinal strain ε_{xx} by Poisson effect [9]:

$$\varepsilon_\perp = \varepsilon_{\perp,1} + \varepsilon_{\perp,2} \approx -2\nu\varepsilon_{xx}\,, \tag{2.7}$$

where ν is the Poisson's ratio of the fibre material. Applying Equation (2.7) to Equation (2.6) in this limit, the relative change of the optical path in vacuum $\Delta L_o/L_o$ is approximately proportional to the longitudinal strain ε_{xx}, i.e.,

$$\frac{\Delta L_o}{L_o} \approx \zeta \varepsilon_{xx} \,, \tag{2.8}$$

where ζ is the stain-optic coefficient defined by

$$\zeta = 1 - \frac{n_g^2}{2} \left[P_{12} - \nu (P_{11} + P_{12}) \right] . \tag{2.9}$$

In this limit, we rewrite Equation (2.4) using the relation in Equation (2.8). Then, the optical phase change is approximately proportional to the longitudinal strain [8, 48]:

$$\Delta\phi \approx \left(\frac{4\pi n_g \zeta L_G}{\lambda_o} \right) \varepsilon_{xx} \,. \tag{2.10}$$

Rearranging Equation (2.10), we can approximately compute the longitudinal strain of the fibre section from the corresponding phase change by

$$\varepsilon_{xx} = \left(\frac{\lambda_o}{4\pi n_g \zeta L_G} \right) \Delta\phi \,. \tag{2.11}$$

The linear relationship in Equation (2.11) is currently the commonly accepted expression for converting the phase change into the longitudinal strain. This approximation works well in most applications. However, we discuss the precise formula based on Equations (2.4) and (2.6) in detail in Paper I.

2.1.3 DAS data format

Continuously DAS recordings are saved to files every 10 seconds with file names `hhmmss.hdf5`, where `hhmmss` is the start time of recording. The time differentiated phase change data are stored as scaled integer values in a 2D array of time and channel indices in Hierarchical Data Format 5 (HDF5) file format[1]. The data are scaled and phase wrapped to be `int32` format. The time differentiated phase change data ($\Delta\dot{\phi}$) is the spatial change over the gauge length of the derivative of the phase with respect to recording time:

$$\Delta\dot{\phi} = \dot{\phi}_{x+L_G/2} - \dot{\phi}_{x-L_G/2} \,. \tag{2.12}$$

Therefore, the integration of the time differentiated phase change data along the time axis is required to determine the spatial phase change ($\Delta\phi$) over a fibre segment and, hence, the axial strain through the Equation (2.11). The integration is computed by

$$\Delta\phi = \int_0^t \Delta\dot{\phi} \, dt \,. \tag{2.13}$$

[1] See `https://portal.hdfgroup.org/display/HDF5/Introduction+to+HDF5`

In most cases, three processing steps below are needed to convert the time differentiated phase change data stored in HDF5 file format into the spatial phase change over a fibre segment:

1. Convert the stored integer values into radians by scaling them with $\pi/2^{29}$.
2. Unwrap the phase along the spatial axis by changing the absolute phase jumps greater than 4π to the 8π complement. Note that the stored phase is usually wrapped at $\pm 4\pi$, where all $\Delta\dot{\phi}$ values outside the range $[-4\pi, 4\pi)$ are wrapped to be within this range.
3. Integrate the data along the time axis by doing a cumulative summation along the time axis as in the Equation (2.13).

Then, we may convert the spatial phase change over a fibre segment into the longitudinal strain using Equation (2.11) for further studies.

2.2 4D Seismic Methods for Subsurface Monitoring

2.2.1 4D seismic

4D seismic is referred to as the method in which a seismic survey is repeated over a given area in order to monitor subsurface changes caused by petroleum production, CO_2 injection, etc. Here calendar time represents the fourth dimension. By this definition, a repeated 2D seismic survey is classified as a 4D seismic survey. A brief overview of 4D seismic can be found in Landrø [35].

4D seismic analysis has evolved as an essential integrity of subsurface reservoir management in many regions since the early 1990s. In the petroleum industry, 4D seismic is employed as a primary surveillance tool to optimise the field-development plan and to improve energy efficiency in operation and production. It is the process of using two or more seismic surveys acquired in the same area to find subsurface changes that occur over time [5].

Subsurface changes due to petroleum production or fluid substitution cause different responses of amplitude and traveltime in the seismic data acquired at different times. These 4D seismic responses are well depicted in Chadwick *et al.* [34, Figure 1] and Landrø [35, Figure 19.6]. Therefore, we can divide the analysis of 4D seismic data into two categories: (1) the detection of seismic amplitude changes, and (2) the detection of seismic traveltime changes (time-shifts).

As discussed in Landrø [35], the 4D amplitude-based method is widely used in practice because of its robustness. However, the 4D traveltime-based method (4D time-shift method) is attractive, because the 4D time-shift is proportional to the change in pay thickness. Hence, the 4D time-shift method gives a direct quantitative result. Both amplitude and time-shift methods are complementary in that the amplitude measurement locally determines the changes close to an interface of two layers, whereas the time-shift measurement determines the average changes over an interval layer [35].

Because the accuracy of 4D seismic has been improved, we can measure small

time-shifts between two seismic traces with an accuracy of a fraction of a millisecond. These time-shifts are a reliable and informative seismic attribute that is related to the subsurface changes caused by petroleum production [49]. Therefore, the 4D time-shift method is increasingly a method of choice. Comprehensive reviews of the 4D seismic poststack time-shift method and its application can be found in MacBeth *et al.* [49] and MacBeth *et al.* [39], respectively. More value could be added by extending the analysis to prestack time-shift analysis.

2.2.2 4D seismic time-shifts

Most 4D seismic time-shifts are measured from a pair of successive poststack seismic volumes (baseline and monitor data) on a trace-by-trace basis using cross-correlation [36] or nonlinear inversion [37]. It is important to measure poststack time-shifts both inside and outside reservoirs. A significant observation of the time-shifts up to 20 ms caused by the overburden stretching above compacting reservoirs was reported at Ekofisk, where the seabed had been sinking over 8 m [38]. The subsidence of the seabed and the subsurface layers could cause instability to the production platforms and other facilities attached to the seabed, which is an element of hazards. Therefore, 4D seismic time-shift analysis can play an important role in hazard management and field operation. Moreover, 4D seismic time-shifts are a robust and stable seismic attribute effectively used to evaluate reservoir dynamics due to production [39].

4D seismic time-shifts are on the spot, because seismic interpretations are done in the time domain of the seismic volumes, all of which have been migrated with one common velocity model. Time-shift analysis using one common velocity model in seismic migration is widely performed, because it has a lower computational cost and less uncertainty than migrating each of the seismic volumes with its individually-updated velocity model [39]. Although data-fitting velocity modelling methods such as 4D full-waveform inversion can possibly provide high-resolution estimates of the 4D change, they are computationally expensive and subject to improvement on reducing artefacts caused by non-repeatability of the survey [40].

In 4D seismic, a time-shift of a reflection event is defined as the difference between its two-way traveltimes measured from baseline and monitor data. According to MacBeth *et al.* [49, Equation 1a and 1b], we usually assume that the monitor data $m(t)$ are approximately a time-shifted version of the baseline data $b(t)$:

$$m(t) \approx b(t-\tau) + \Delta s(t-\tau) + n(t), \tag{2.14}$$

where $\tau \equiv f(t)$ is a time-dependent time-shift function, $\Delta s(t)$ is a signal for time-lapse amplitude changes, and $n(t)$ is non-repeatable noise. Note that we use the notation τ as the time-shift that is different from Δt used in MacBeth *et al.* [49, Equation 1a and 1b]. In this thesis, Equation (2.14) implies that the traveltime of an event in the baseline data is lengthened by τ to match the time of the same event in the monitor data. For time-lapse changes in a homogeneous isotropic

layer with a fixed top (zero time-shift at the top), the time-shift of the bottom simply equals the change in the two-way traveltime (time thickness) of the layer.

2.2.3 From time-shifts to time strains

A 4D time-shift is a cumulative effect of subsurface changes from the surface down to a particular depth. To study the properties of each subsurface rock interval in the stratified isotropic layers shown in Figure 2.2, we have to convert time-shifts into time strains, which are an interval seismic attribute. Here, a time strain is defined as the fractional time-lapse change in the two-way traveltime (time thickness) of the corresponding layer. For a thin layer of thickness dz in the multi-layer model (Figure 2.2b), its time strain is derived by taking the time derivative of the time-shift volume [36, 37]:

$$\frac{\Delta(dt)}{dt} = \frac{\partial \tau}{\partial t}, \tag{2.15}$$

where τ is the time-dependent time-shift attribute, and dt is the two-way traveltime of the thin layer.

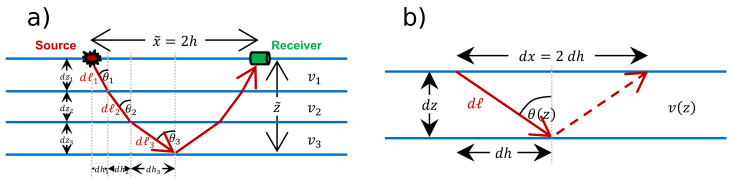

Figure 2.2: Schematic diagram of 4D time-shift analysis in stratified layers: (a) a surface seismic survey on a pile of homogeneous layers, and (b) a single homogeneous layer in microscale (retrieved from Paper IV).

2.2.4 Effect of subsurface changes on time strains

Fundamentally, a traveltime change of a layer is caused by changes in the seismic velocity and the thickness of the layer. Landrø and Stammeijer [50] propose an approximate solution for normal incidence to estimate the 4D time thickness change from the thickness and velocity changes of a homogeneous flat layer:

$$\frac{\Delta(dt)}{dt} \approx \frac{\Delta(dz)}{dz} - \frac{\Delta v}{v}, \tag{2.16}$$

where dt represents the normal-incident two-way traveltime (time thickness), dz represents the layer thickness, and v represents the seismic velocity of the layer. Therefore, the term $\Delta(dt)/dt$ is the time strain of the layer. Similarly, $\Delta(dz)/dz$ and $\Delta v/v$ are referred to as thickness strain and velocity strain, respectively. Time strain is measurable from 4D seismic data, making up a set of observed data, while

thickness and velocity strains are the two parameters that must be solved in Equation (2.16). Equation (2.16) implies that a positive change in the time thickness is caused by either an increase of the thickness or a decrease of the velocity. Note that this equation is valid for vertical wave propagation in a single horizontal layer, where the relative changes are sufficiently small, i.e., $\Delta(dz)/dz \ll 1$ and $\Delta v/v \ll 1$.

Interpretations of 4D time-shifts are usually simplified by either neglecting displacement changes (strains) or assuming a linear relation of thickness and velocity strains [51]. Assuming that the fractional change in the velocity is proportional to the fractional change in the thickness, i.e., $\Delta v/v = -R\,\Delta(dz)/dz$, Equation (2.16) could be simplified to

$$\frac{\Delta(dt)}{dt} \approx (1+R)\,\frac{\Delta(dz)}{dz}\,, \tag{2.17}$$

where R is a positive dimensionless dilation factor [52, 53]:

$$R \equiv -\frac{\Delta v/v}{\Delta(dz)/dz}\,. \tag{2.18}$$

Here, the dilation factor R of a layer is defined as the negative velocity strain divided by the thickness strain of the layer. Then, we can simplify the time strain formula to be proportional to the thickness strain.

R factor depends on the lithology. Hatchell and Bourne [52] suggest that the R factor ranges from 4 to 6 for non-reservoir rocks in extension and from 1 to 3 for reservoir rocks under compression. However, several studies suggest that the R factor also varies with stress conditions [54, 55]. Because the R factor depends on the physical properties of rocks, the R factor is not a constant. Therefore, both R factor and thickness strain $\Delta(dz)/dz$ are the two parameters in Equation (2.17). Thus, Equations (2.16) and (2.17) have the same number of parameters to be solved. That is, the use of R factor does not reduce the number of variables in computation. Unless the accurate model of the R factor of a rock is given, the linear relationship between the thickness and velocity strains does not reduce the complexity of the problem.

2.2.5 Time-shift variation with offset

We can measure and analyse 4D seismic time-shifts in prestack and poststack time domains. In the poststack domain, the processed seismic data are assumed to be zero-offset and associated with vertical ray paths. However, multi-offset seismic data are normally acquired in 4D seismic surveys. The 4D time-shifts in such prestack seismic data are offset (angle) dependent. Therefore, they provide more information for subsurface characterisation than zero-offset time-shifts.

Landrø and Stammeijer [50] and Røste *et al.* [56] propose models to describe time-shift variation with offset in homogeneous isotropic media. Moreover, prestack seismic time-shift analysis has the advantage of interpretation over poststack analysis [57]. In practice, prestack seismic time-shifts can be used to estimate

the 4D velocity changes through time-shift tomography [58, 59]. Moreover, they can be used together with 4D amplitude analysis to estimate both thickness and velocity changes [60].

In our understandings, no methods based on time-shifts only have been proposed to estimate the thickness and velocity changes independently. In addition, most of the 4D seismic methods for estimating thickness and velocity changes have been developed only based on isotropic media with little heterogeneity. In fact, we should incorporate the heterogeneity and anisotropy in the subsurface into 4D models, because both of them can significantly affect the time-shift variation with offset [61, 62].

Chapter 3

Contributions

3.1 Summary

The research work that constitutes this thesis was conducted at the Acoustics Group, Department of Electronic Systems, Faculty of Information Technology and Electrical Engineering, Norwegian University of Science and Technology (NTNU), from February 2020 to March 2023. It was conducted under the supervision of Professor Martin Landrø (NTNU), and the co-supervision of Professor Børge Arntsen (NTNU). The work was funded by the Research Council of Norway (RCN) and the sponsors of the Geophysics and Applied Mathematics in Exploration and Safe production Project (GAMES; RCN grant no. 294404), and the SFI Centre for Geophysical Forecasting (CGF; RCN grant no. 309960). In addition, I received financial support from PTT Exploration and Production Public Company Limited (PTTEP) to pursue the PhD at NTNU.

This chapter summarises the research work that constitutes this thesis. The thesis comprises four research articles listed in Section 3.2. My contributions to each individual article are also described. Other results of my research dissemination, which are not attached to this thesis, are listed in Section 3.3.

This thesis contributes to the advancement of two research areas that are associated with subsurface monitoring: (1) the use of fibre-optic DAS technology for subsurface seismic exploration and monitoring in marine environment, and (2) the traveltime-based 4D seismic method for subsurface monitoring. An overview of the research articles and their contributions to the two research areas are given in the later sections in this chapter.

3.2 List of Publications

The list below contains the key research articles recently published or in peer-review that constitute this thesis. These research articles are reproduced and attached to the end of this thesis.

Paper I: K. Taweesintananon, M. Landrø, J. K. Brenne and A. Haukanes, 'Distrib-

uted acoustic sensing for near-surface imaging using submarine telecommunication cable: A case study in the Trondheimsfjord, Norway,' en, *GEOPHYSICS*, vol. 86, no. 5, B303–B320, Sep. 2021, ISSN: 0016-8033, 1942-2156. DOI: 10.1190/geo2020-0834.1. [Online]. Available: https://library.seg.org/doi/10.1190/geo2020-0834.1 (visited on 03/05/2022)

Summary: Taweesintananon et al. compare the near-surface seismic images from a hydrophone array and distributed acoustic sensing (DAS) applied to a submarine telecommunication cable in Trondheimsfjord, Norway. Their study shows enormous potential of DAS applications for marine seismic exploration.

Contributions: M.L. and J.K.B. conceived and designed the experiment. K.T., M.L. and A.H. collected data. K.T. developed methodology, processed data and prepared visualisations. K.T. and M.L. analysed the data with support from J.K.B. M.L. validated research outputs, acquired funding, and managed the project. K.T. wrote the original draft of the manuscript. All the authors conducted review and editing of the manuscript.

Paper II: L. Bouffaut, K. Taweesintananon, H. J. Kriesell, R. Rørstadbotnen, J. R. Potter, M. Landrø, S. E. Johansen, J. K. Brenne, A. Haukanes, O. Schjelderup and F. Storvik, 'Eavesdropping at the speed of light: Distributed acoustic sensing of baleen whales in the Arctic,' en, *Frontiers in Marine Science*, vol. 9, p. 901 348, 2022. DOI: 10.3389/fmars.2022.901348. [Online]. Available: https://www.frontiersin.org/articles/10.3389/fmars.2022.901348/full (visited on 01/07/2022)

Summary: Bouffaut et al. present the first case of wildlife monitoring using distributed acoustic sensing (DAS). By repurposing the globally-available infrastructure of subsea telecommunication fibre-optic cables, they show that DAS can (1) record vocalising baleen whales along a 120 km fibre-optic cable with a sensing point every 4 m, from a protected fjord area out to the open ocean; (2) estimate the 3D position of a vocalising whale for animal density estimation; and (3) exploit whale non-stereotyped vocalisations to provide fully-passive conventional seismic records for subsurface exploration.

Contributions: L.B. wrote the manuscript, read and approved by all co-authors. L.B. and H.J.K. conducted the acoustic data analysis; L.B. designed and produced most of the results shown in the manuscript, interpreted together with H.J.K., M.L. and J.R.P.; K.T. and M.L. produced and wrote about the subsurface exploration results and interpretation. L.B., K.T. and R.A.R. developed data handling and processing routines. M.L., J.K.B., A.H., S.E.J., O.S., and F.S. conceived the experiment. A.H. and F.S. collected the DAS data. All authors contributed to the article and approved the submitted version.

Paper III: K. Taweesintananon, M. Landrø, J. R. Potter, S. E. Johansen, R. A.

Rørstadbotnen, L. Bouffaut, H. J. Kriesell, J. K. Brenne, A. Haukanes, O. Schjelderup and F. Storvik, 'Distributed acoustic sensing of ocean-bottom seismo-acoustics and distant storms: A case study from Svalbard, Norway,' *GEOPHYSICS*, vol. 88, no. 3, B135–B150, May 2023, ISSN: 0016-8033. DOI: 10.1190/geo2022-0435.1. [Online]. Available: https://doi.org/10.1190/geo2022-0435.1 (visited on 29/04/2023)

Summary: Taweesintananon et al. review the mechanisms of ocean-bottom vibrations recorded by distributed acoustic sensing (DAS) in a submarine telecommunication fibre-optic cable in Svalbard, Norway. They show that ocean-bottom DAS data can be used to map near-surface geologic structure and to trace ocean swells back to their storm origins as far as 13,000 km away from the cable.

Contributions: M.L., S.E.J., J.K.B., A.H., O.S. and F.S. conceived and designed the experiment. A.H. and F.S. collected data. K.T. processed data and prepared the visualisations. K.T. and M.L. analysed data with support from J.R.P., S.E.J., R.A.R., L.B. and H.J.K. M.L. and J.R.P. validated research outputs, acquired funding, and managed the project. K.T. wrote the original draft of the manuscript. All the authors conducted review and editing of the manuscript.

Paper IV: K. Taweesintananon, M. Landrø, S. Narongsirikul and P. G. Folstad, 'Angle-dependent 4D seismic time-strain inversion for estimating subsurface thickness and velocity changes,' en, Unpublished manuscript, Trondheim, Norway, 2023

Summary: Taweesintananon et al. propose a method to estimate thickness and velocity strains simultaneously from angle-dependent 4D seismic time strains. The method is applicable for elliptical vertical transverse isotropic (VTI) media.

Contributions: K.T. conceived and designed the research methods. S.N. and P.G.F. collected field data. K.T. processed the data and prepared the visualisations. K.T. and M.L. analysed the data with support from S.N. and P.G.F. M.L. validated the research outputs, acquired funding, and managed the project. K.T. wrote the original draft of the manuscript. All the authors reviewed and edited the manuscript.

3.3 List of Other Results

The list below contains my research dissemination that is not reproduced nor attached to this thesis.

1. R. A. Rørstadbotnen, J. Eidsvik, L. Bouffaut, M. Landrø, J. Potter, K. Taweesintananon, S. Johansen, F. Storevik, J. Jacobsen, O. Schjelderup, S. Wienecke, T. A. Johansen, B. O. Ruud, A. Wuestefeld and V. Oye, 'Simultaneous tracking of multiple whales using two fiber-optic cables in the Arctic,'

Frontiers in Marine Science, vol. 10, p. 1 130 898, 2023, ISSN: 2296-7745. DOI: 10.3389/fmars.2023.1130898. [Online]. Available: https://www.frontiersin.org/articles/10.3389/fmars.2023.1130898

2. M. Landrø, L. Bouffaut, H. J. Kriesell, J. R. Potter, R. A. Rørstadbotnen, K. Taweesintananon, S. E. Johansen, J. K. Brenne, A. Haukanes, O. Schjelderup and F. Storvik, 'Sensing whales, storms, ships and earthquakes using an Arctic fibre optic cable,' *Scientific Reports*, vol. 12, no. 1, p. 19 226, Nov. 2022, ISSN: 2045-2322. DOI: 10.1038/s41598-022-23606-x. [Online]. Available: https://doi.org/10.1038/s41598-022-23606-x
3. R. A. Rørstadbotnen, M. Landrø, K. Taweesintananon, L. Bouffaut, J. Potter, S. E. Johansen, H. J. Kriesell, J. K. Brenne, A. Haukanes, O. Schjelderup and F. Storvik, 'Analysis of a local earthquake in the Arctic using a 120 km long fibre-optic cable,' en, in *83rd EAGE Annual Conference & Exhibition*, ser. Conference Proceedings, vol. 2022, Madrid, Spain: European Association of Geoscientists & Engineers, 2022, pp. 1–5. DOI: 10.3997/2214-4609.202210404. [Online]. Available: https://www.earthdoc.org/content/papers/10.3997/2214-4609.202210404
4. K. Taweesintananon, M. Landrø, S. Narongsirikul and P. G. Folstad, 'Angle-variant 4D seismic time-shift analysis for velocity change and subsurface strain estimation,' en, in *83rd EAGE Annual Conference & Exhibition*, ser. Conference Proceedings, vol. 2022, Madrid, Spain: European Association of Geoscientists & Engineers, 2022, pp. 1–5. DOI: 10.3997/2214-4609.202210437. [Online]. Available: https://www.earthdoc.org/content/papers/10.3997/2214-4609.202210437

3.4 Ocean-Bottom DAS for Subsurface Exploration and Monitoring

3.4.1 Use of active seismic sources

Paper I extensively describes the principle of DAS interrogation for fibre-optic strain measurement. It also shows that DAS in a straight fibre-optic cable is sensitive to both longitudinal and transverse strains of the cable. This concept is against the commonly accepted practice of the fibre-optic sensing industry, in which only longitudinal strains attribute to the optical phase changes interrogated by DAS and DAS in a straight fibre-optic cable is not sensitive to broadside P-waves (inducing transverse strains in the cable) that are propagating in the perpendicular direction to the cable axis. In Paper I, we show that broadside P-waves associated with transverse strains in the cable become significant and must not be negligible for high-frequency waves ($>$ 100 Hz in this case).

In addition, Paper I discusses the procedures and demonstrates how to produce subsurface seismic images from ocean-bottom (seabed) DAS recording data of active marine seismic sources. It compares the seismic images from the seabed DAS data with the seismic images from a single-channel hydrophone streamer towed

near the sea surface. The comparison confirms the potential of using seabed DAS for subsurface seismic imaging. In my understanding, Paper I is the first research article that demonstrates such a potential of marine subsurface seismic imaging using active seismic sources and DAS receiver arrays deployed on the earth's surface.

Prior to the publication of Paper I, there were several research articles discussing DAS applications to seismic imaging from borehole seismic data. There were also articles that used DAS deployed on the earth's surface for passive seismic monitoring in land and marine environment. A few articles used DAS as surface seismic receivers in land surface seismic exploration. However, DAS applications to produce subsurface seismic images in marine environment had not been widely presented nor published. Therefore, Paper I advances the fibre-optic sensing industry with the verification that DAS can be used for subsurface seismic exploration not only in land environment but also in marine environment. The validity of DAS in marine seismic exploration given in Paper I could pave the potential growth of DAS technology in the seabed seismic market.

3.4.2 Use of passive seismic sources

Paper II demonstrates another seabed DAS application for subsurface seismic exploration. Here, vocalising baleen whales were used as fully-passive marine seismic sources for DAS data recording. As shown in Paper II, whales frequently behave like marine vibrators, because whale vocalisations have similar characteristics to the wave trains in time-variant frequency sweeps of vibroseis used in land seismic surveys. Therefore, it is possible to obtain conventional seismic records from whale vocalisations using the same process as land vibroseis data.

The key requirement of using whale vocalisations for subsurface imaging is to determine the seismic source parameters, i.e., the position and the time that a whale starts vocalising. With some constraints discussed in Paper II, the source position and start time can be estimated approximately from the direct arrival times of the whale vocalisation to the seabed DAS receiver array. When the source position and start time of a whale vocalisation are known, we can process and produce conventional seismic records from whale vocalisations as shown in Paper II. With sufficient amount of such seismic records, we could further obtain subsurface seismic images using a conventional seismic data processing techniques for seabed seismic data.

3.4.3 Use of shear-wave resonances

In addition to marine seismic sources discussed in Paper I and Paper II, seabed DAS can measure the ocean-bottom vibrations excited by many types of sources. Paper III reviews the mechanisms of ocean-bottom vibrations recorded by seabed DAS in Svalbard, Norway. Some mechanisms are related to the loading pressure changes caused by OSGWs, which help us identify their storm origins up to 13,000 km distant from the fibre-optic cable. Some excitation mechanisms are

associated with the subsurface layers below the seabed. The signals corresponding to these mechanisms could be used for subsurface characterisation.

Paper III shows that we can use shear-wave resonances within the near-surface low-velocity layers as recorded by seabed DAS to map the geologic structures of these layers. The shear-wave resonance signals used for this structural mapping are fully passive and generated from natural phenomena. Hence, Paper III demonstrates another DAS application for subsurface exploration and monitoring using shear-wave resonances to map the near-surface geologic structures.

3.5 4D Seismic Time-Strain Inversion for Subsurface Monitoring

In a 4D seismic analysis, the time-shift of a certain seismic reflection event is caused by the changes in the seismic velocity and the depth of the corresponding reflector. An interpretation of 4D seismic time-shifts is normally simplified by neglecting displacement changes (strains) or assuming a linear relation of thickness and velocity strains. Paper IV goes beyond these assumptions and proposes a least-squares optimisation method to simultaneously estimate the thickness and velocity strains in elliptical vertical transverse isotropic (VTI) media from angle-dependent 4D seismic time strains.

To determine subsurface changes from 4D seismic time-shifts, we have to know the angle-dependent relation between time strains and the changes in thickness and interval velocity of a rock layer. In Paper IV, we extend the procedure used in Taweesintananon *et al.* [69] to derive the angle-dependent time-strain equation in anisotropic media. Here, we simplify the equation for elliptical VTI media, so that we can approximately estimate the angle-dependent normal move-out (NMO) time strain from the three parameters describing subsurface changes: thickness strain, vertical velocity strain, and time-lapse change of the ε parameter. Using this equation, we can establish an inverse problem to infer these subsurface changes by minimising the misfit between the observed NMO time strain and their estimated NMO time strain. In this inverse problem, we define NMO time strains as the data, whereas the three subsurface change parameters are the model parameters. The observed NMO time strain data are angle-dependent, so the time strain measurements must be made on NMO-corrected (migrated) seismic images at different incidence angles, which are called "angle stacks." In Paper IV, we formulate the inverse problem as a regularised convex least-squares optimisation problem on a trace-by-trace basis, in which all the constraints are defined based on the zero-offset NMO time strain equation. The convex optimisation requires no initial model to determine the solution at the global minima.

In Paper IV, we propose the method called "4D seismic time-strain inversion" to estimate the thickness strains, velocity strains and changes in anisotropic parameters simultaneously from angle-dependent 4D seismic time strains. The computation is done without prior knowledge in stress paths and geomechanics in the

survey area. We apply the method to both synthetic and field seismic data. As discussed in Paper IV, we believe that these time-strain inversion results can describe the subsurface changes based on fluid types, fluid saturation, stress, mechanical processes, chemical processes, etc. The results are the basis of many other attributes for geomechanics studies and field management. Thus, we see that our method has high potential in many other applications for subsurface monitoring.

Chapter 4

Discussion

4.1 DAS for Subsurface Exploration and Monitoring

The advantages of fibre-optic DAS technology for subsurface monitoring are discussed as follows. DAS is a linear array of strain sensors along a fibre-optic cable. In field experiment, the receiver spacing of DAS could be as small as 1 m. Therefore, the spatial resolution of DAS recording data is relatively high in comparison with the use of conventional seismic point sensors in practice.

Moreover, the temporal resolution of DAS is comparable to conventional seismic recording system. Unless the disk space for data storage is limited, the DAS recording can be performed continuously at the same time sampling interval as or even smaller than the conventional seismic data acquisition, in which 2 ms time sampling interval is typical for petroleum exploration.

All the measurement and the power supplies to the sensing elements are controlled by one DAS interrogator that is connected to one end of the cable. Once the fibre-optic cable and DAS recording system are installed, the maintenance of the system only occurs at the interrogator. This is one of the key advantages of DAS over other conventional seismic point sensors in which more efforts are needed to operate the power supplies connected to the groups of sensors deployed in the field. Hence, DAS recording system is probably a method of choice for long-period continuously seismic recording with high spatial and temporal resolutions.

The only drawback of DAS recording system is the sensitivity to broadside P-wave propagation. The commonly accepted practice in the fibre-optic sensing industry is to neglect the DAS response to transverse strains, that is, the sensitivity to the broadside P-wave propagation is negligible. Paper I shows that this assumption is incorrect for the DAS response to high-frequency P-waves (> 100 Hz). In Paper I, we show that DAS in a straight fibre-optic cable deployed on the seafloor can sense the broadside P-wave propagation from a high-frequency marine seismic source. These broadside P-wave signals are not negligible in the DAS recording data. The data can be processed further to construct subsurface seismic images used for subsurface exploration and monitoring.

4.2 Use of Natural Sources for Subsurface Imaging

As discussed above, we can process and construct seismic images from the data acquired by using a seabed DAS array as the receivers and a marine impulsive seismic source as the sources. We may generalise this DAS application for subsurface seismic imaging using other types of seismic sources.

In Paper II, we initiate the idea of using whale vocalisations as the seismic sources together with a seabed DAS array as the seismic receivers. However, whale vocalisations are usually not impulsive. Here, we find that some of the whale vocalisations are time-variant in frequency and generate similar frequency-swept wave trains to the vibroseis signals used in land surface seismic exploration. Accordingly, we consider whales as natural marine seismic vibrators. Then, we apply the same data processing technique as in vibroseis-based land surface seismic exploration to the DAS data from whale vocalisations. Finally, we obtain conventional seismic recording profiles from individual whale vocalisations recorded by seabed DAS. Like conventional seismic survey, these seismic profiles can be processed further to construct subsurface seismic images and used for subsurface exploration and monitoring.

The key requirements of using whale vocalisations for subsurface imaging are discussed as follows. First, the spatial location and the start time of each whale vocalisation must be known. These source parameters may be estimated by travel-time inversion of the direct arrival of the whale-vocalised seismic waves to the DAS array. Second, the source wave train of each whale vocalisation must be known. This source wave train could be obtained by stacking the whale-vocalised seismic data after time-delay correction for the direct arrival followed by the removal of source seismic ghosts. Third, the source wave trains of whale vocalisation must have frequency variation with time, so that conventional seismic profiles can be constructed by the cross-correlation between the source wave trains and the DAS data. In Paper II, the data processing techniques used to meet these requirements require human intervention such as picking of the time of direct arrivals and determining the source locations. Hence, data processing techniques should be further studied and developed to meet all these requirements without human intervention. Then, I hope that we can find effective data processing techniques to process the DAS data and construct the subsurface seismic images from whale vocalisations in the near future.

Shear-wave resonances in low-velocity layers can be another type of sources for subsurface imaging. Paper III demonstrates this application using the shear-wave resonances recorded by DAS in a seabed fibre-optic cable in the Isfjord, Svalbard. The shear-wave resonances can be measured only in association with a low-velocity layer with strong velocity contrasts to the upper and lower layers. This geologic setting is presented in the Isfjord, in which low-velocity shallow glacimarine sediments were deposited on a consolidated bedrock. The use of shear-wave resonances for subsurface characterisation is probably applicable only in marine environment, in which the oceanic dynamics are continuous and

sufficiently strong. The seismic waves caused by oceanic dynamics are the key energy contributors to the shear-wave resonances underneath the water column. In contrast, the shear-wave resonances could be hardly observed in land surface DAS measurement, because the impact of continuous atmospheric dynamics on the solid earth is much lower.

4.3 4D Seismic Time-Strain Inversion for Subsurface Monitoring

Paper IV greatly contributes to the advancement and development of the scientific knowledge of 4D seismic methods for subsurface monitoring. In Paper IV, I develop mathematical formulae of the angle-dependent 4D seismic time strains into a new traveltime-based 4D seismic method to determine the subsurface changes in elliptical VTI media. The new method is called "4D seismic time-strain inversion." As shown in Paper IV, preliminary results of this method are promising and reveal high potential in commercialisation.

The 4D seismic time-strain inversion method presented in Paper IV is a trace-by-trace operation, and it is developed based on one-dimensional (1D) velocity model. That is, it assumes that there is no lateral variation of velocity and thickness of the subsurface layers around the seismic reflection points. The presence of lateral velocity variation may cause errors in fitting the angle-dependent time strain data in time-strain inversion. Paper IV illustrates such errors in the case of two-dimensional (2D) synthetic data. The development of the 4D seismic time-strain inversion method to handle more complicated velocity models could be a challenging research area for the upcoming years.

As discussed in Paper IV, 4D seismic time-strain inversion requires accurate measurement of the 4D seismic time-shifts and, hence, the corresponding time strains. A small error in 4D seismic time-shift estimation may cause a large error in the successive 4D seismic time-strain inversion. Therefore, the research and development in the 4D seismic time-shift measurement are still required to improve the accuracy of 4D seismic time-shift measurement and reduce uncertainty in 4D seismic time-strain inversion.

Chapter 5

Conclusion

5.1 Summary

This thesis clearly demonstrates the applications of seabed fibre-optic DAS technology to subsurface monitoring. It also develops and demonstrates a new traveltime-based 4D seismic method, called "4D seismic time-strain inversion," for subsurface monitoring. All the work done in this thesis contributes to the advancement of fibre-optic DAS and 4D seismic technologies for subsurface monitoring.

5.2 Technology Outlook

Fibre-optic DAS technology could be used in an enormous number of seismo-acoustic applications, thanks to its detectability of the waves in broadband frequency ranges and its high spatial resolution discussed in Paper III. Although this thesis focuses on subsurface monitoring, I foresee a great opportunity of fibre-optic DAS technology in a wide range of applications which include, but not limited to, subsurface exploration and monitoring, earthquake monitoring, storm monitoring, geohazard monitoring, infrastructure monitoring, land and marine traffic monitoring, land and marine wildlife monitoring, medical imaging, and acoustic engineering.

Nevertheless, we shall not avoid the fact that DAS in straight fibre-optic cables is not measurement of full wavefields, and that it is more sensitive to longitudinal strains than transverse strains of the cables. The partial measurement of full wavefields is probably one of the key challenges and obstacles for DAS technology to be mature. I believe more attentions should be paid on the development of DAS to sense full seismo-acoustic wavefields while maintaining their other advantages of high spatial resolution and large dimension of the linear sensing arrays.

On the other hand, angle-dependent 4D seismic time-strain inversion presented in Paper IV would raise awareness to all geophysicists who have been working on 4D seismic for subsurface monitoring. This method can determine the subsurface changes without prior knowledge nor assumption on geomechanical proper-

ties in the field. It is easy to implement this method for field data. I hope Paper IV can attract many geophysicists to review their 4D seismic interpretation and to re-evaluate their 4D seismic data sets using 4D seismic time-strain inversion.

Bibliography

[1] M. A. Capello, A. Shaughnessy and E. Caslin, 'The Geophysical Sustainability Atlas: Mapping geophysics to the UN Sustainable Development Goals,' en, *The Leading Edge*, vol. 40, no. 1, pp. 10–24, Jan. 2021, ISSN: 1070-485X. DOI: 10.1190/tle40010010.1. [Online]. Available: https://doi.org/10.1190/tle40010010.1 (visited on 01/02/2023).

[2] O. Monrigal, I. de Jong and H. Duarte, 'An ultra-high-resolution 3D marine seismic system for detailed site investigation,' en, *Near Surface Geophysics*, vol. 15, no. 4, pp. 335–345, Aug. 2017, ISSN: 15694445, 18730604. DOI: 10.3997/1873-0604.2017025. [Online]. Available: http://doi.wiley.com/10.3997/1873-0604.2017025 (visited on 31/08/2020).

[3] V. Vinje, J. E. Lie, V. Danielsen, P. E. Dhelie, R. Siliqi, C.-I. Nilsen, E. Hicks and A. Camerer, 'Shooting over the seismic spread,' en, *First Break*, vol. 35, no. 6, p. 8, Jun. 2017.

[4] Y. Thomas, B. Marsset, G. Westbrook, C. Grail, L. Géli, P. Henry, G. Çifçi, A. Rochat and H. Saritas, 'Contribution of high-resolution 3D seismic near-seafloor imaging to reservoir-scale studies: Application to the active North Anatolian Fault, Sea of Marmara,' en, *Near Surface Geophysics*, vol. 10, no. 4, pp. 291–301, Aug. 2012, ISSN: 15694445, 18730604. DOI: 10.3997/1873-0604.2012019. [Online]. Available: http://doi.wiley.com/10.3997/1873-0604.2012019 (visited on 03/09/2020).

[5] M. Landrø and L. Amundsen, *Introduction to exploration geophysics with recent advances*, en. Bivrost Geo, 2018, OCLC: 1060774435, ISBN: 978-82-303-3763-9.

[6] J. Langhammer, M. Eriksrud and H. Nakstad, 'Performance characteristics of 4C fiber optic ocean bottom cables for permanent reservoir monitoring,' en, in *SEG Technical Program Expanded Abstracts 2010*, Society of Exploration Geophysicists, Jan. 2010, pp. 66–70. DOI: 10.1190/1.3513871. [Online]. Available: http://library.seg.org/doi/abs/10.1190/1.3513871 (visited on 16/09/2020).

[7] Y. Wang, H. Yuan, X. Liu, Q. Bai, H. Zhang, Y. Gao and B. Jin, 'A Comprehensive Study of Optical Fiber Acoustic Sensing,' en, *IEEE Access*, vol. 7, pp. 85 821–85 837, 2019, ISSN: 2169-3536. DOI: 10.1109/ACCESS.2019.

2924736. [Online]. Available: https://ieeexplore.ieee.org/document/8744553/ (visited on 22/05/2020).

[8] A. H. Hartog, *An introduction to distributed optical fibre sensors*, en, 1st ed. CRC Press, May 2017, ISBN: 978-1-315-11901-4. DOI: 10.1201/9781315119014. [Online]. Available: https://www.taylorfrancis.com/books/9781482259582 (visited on 04/11/2020).

[9] B. Kuvshinov, 'Interaction of helically wound fibre-optic cables with plane seismic waves,' *Geophysical Prospecting*, vol. 64, no. 3, pp. 671–688, May 2016, Publisher: John Wiley & Sons, Ltd, ISSN: 0016-8025. DOI: 10.1111/1365-2478.12303. [Online]. Available: https://doi.org/10.1111/1365-2478.12303 (visited on 25/01/2021).

[10] B. Papp, D. Donno, J. E. Martin and A. H. Hartog, 'A study of the geophysical response of distributed fibre optic acoustic sensors through laboratory-scale experiments: Geophysical response of fibre optic sensors,' en, *Geophysical Prospecting*, vol. 65, no. 5, pp. 1186–1204, Sep. 2017, ISSN: 00168025. DOI: 10.1111/1365-2478.12471. [Online]. Available: http://doi.wiley.com/10.1111/1365-2478.12471 (visited on 26/08/2020).

[11] T. M. Daley, B. M. Freifeld, J. Ajo-Franklin, S. Dou, R. Pevzner, V. Shulakova, S. Kashikar, D. E. Miller, J. Goetz, J. Henninges and S. Lueth, 'Field testing of fiber-optic distributed acoustic sensing (DAS) for subsurface seismic monitoring,' en, *The Leading Edge*, vol. 32, no. 6, pp. 699–706, Jun. 2013, ISSN: 1070-485X, 1938-3789. DOI: 10.1190/tle32060699.1. [Online]. Available: http://library.seg.org/doi/10.1190/tle32060699.1 (visited on 09/06/2020).

[12] T. Dean, T. Brice, A. Hartog, E. Kragh, D. Molteni and K. O'Connell, 'Distributed vibration sensing for seismic acquisition,' *The Leading Edge*, vol. 35, no. 7, pp. 600–604, Jul. 2016, Publisher: Society of Exploration Geophysicists, ISSN: 1070-485X. DOI: 10.1190/tle35070600.1. [Online]. Available: https://doi.org/10.1190/tle35070600.1 (visited on 13/09/2020).

[13] P. Lumens, 'Fibre-optic sensing for application in oil and gas wells,' en, Phd Thesis 1 (Research TU/e / Graduation TU/e), Technische Universiteit Eindhoven, Eindhoven, 2014. [Online]. Available: https://doi.org/10.6100/IR769555 (visited on 22/05/2020).

[14] B. Biondi, E. Martin, S. Cole, M. Karrenbach and N. Lindsey, 'Earthquakes analysis using data recorded by the Stanford DAS array,' en, in *SEG Technical Program Expanded Abstracts 2017*, Houston, Texas: Society of Exploration Geophysicists, Aug. 2017, pp. 2752–2756. DOI: 10.1190/segam2017-17745041.1. [Online]. Available: http://library.seg.org/doi/10.1190/segam2017-17745041.1 (visited on 26/08/2020).

[15] J. B. Ajo-Franklin, S. Dou, N. J. Lindsey, I. Monga, C. Tracy, M. Robertson, V. Rodriguez Tribaldos, C. Ulrich, B. Freifeld, T. Daley and X. Li, 'Distributed Acoustic Sensing Using Dark Fiber for Near-Surface Characterization and Broadband Seismic Event Detection,' en, *Scientific Reports*, vol. 9, no. 1, p. 1328, Dec. 2019, ISSN: 2045-2322. DOI: 10.1038/s41598-018-36675-8. [Online]. Available: http://www.nature.com/articles/s41598-018-36675-8 (visited on 07/06/2020).

[16] C. Yu, Z. Zhan, N. J. Lindsey, J. B. Ajo-Franklin and M. Robertson, 'The Potential of DAS in Teleseismic Studies: Insights From the Goldstone Experiment,' en, *Geophysical Research Letters*, vol. 46, no. 3, pp. 1320–1328, Feb. 2019, ISSN: 0094-8276, 1944-8007. DOI: 10.1029/2018GL081195. [Online]. Available: https://onlinelibrary.wiley.com/doi/abs/10.1029/2018GL081195 (visited on 26/08/2020).

[17] M. R. Fernández-Ruiz, M. A. Soto, E. F. Williams, S. Martin-Lopez, Z. Zhan, M. Gonzalez-Herraez and H. F. Martins, 'Distributed acoustic sensing for seismic activity monitoring,' en, *APL Photonics*, vol. 5, no. 3, p. 030 901, Mar. 2020, ISSN: 2378-0967. DOI: 10.1063/1.5139602. [Online]. Available: http://aip.scitation.org/doi/10.1063/1.5139602 (visited on 07/06/2020).

[18] S. Dou, N. Lindsey, A. M. Wagner, T. M. Daley, B. Freifeld, M. Robertson, J. Peterson, C. Ulrich, E. R. Martin and J. B. Ajo-Franklin, 'Distributed Acoustic Sensing for Seismic Monitoring of The Near Surface: A Traffic-Noise Interferometry Case Study,' en, *Scientific Reports*, vol. 7, no. 1, p. 11 620, Dec. 2017, ISSN: 2045-2322. DOI: 10.1038/s41598-017-11986-4. [Online]. Available: http://www.nature.com/articles/s41598-017-11986-4 (visited on 22/05/2020).

[19] G. Fang, Y. E. Li, Y. Zhao and E. R. Martin, 'Urban Near-Surface Seismic Monitoring Using Distributed Acoustic Sensing,' en, *Geophysical Research Letters*, vol. 47, no. 6, Mar. 2020, ISSN: 0094-8276, 1944-8007. DOI: 10.1029/2019GL086115. [Online]. Available: https://onlinelibrary.wiley.com/doi/abs/10.1029/2019GL086115 (visited on 26/08/2020).

[20] J. Ajo-Franklin, N. Lindsey, T. Daley, B. Freifeld, M. Robertson, C. Ulrich, S. Dou, E. Martin and A. Wagner, 'A Field Test of Distributed Acoustic Sensing for Ambient Noise Recording,' en, in *SEG Technical Program Expanded Abstracts 2015*, New Orleans, Louisiana: Society of Exploration Geophysicists, Aug. 2015, pp. 2620–2624. DOI: 10.1190/segam2015-5926936.1. [Online]. Available: http://library.seg.org/doi/10.1190/segam2015-5926936.1 (visited on 26/08/2020).

[21] E. R. Martin, C. M. Castillo, S. Cole, P. S. Sawasdee, S. Yuan, R. Clapp, M. Karrenbach and B. L. Biondi, 'Seismic monitoring leveraging existing telecom infrastructure at the SDASA: Active, passive, and ambient-noise analysis,' en, *The Leading Edge*, vol. 36, no. 12, pp. 1025–1031, Dec. 2017,

ISSN: 1070-485X, 1938-3789. DOI: 10.1190/tle36121025.1. [Online]. Available: https://library.seg.org/doi/10.1190/tle36121025.1 (visited on 26/08/2020).

[22] E. R. Martin, F. Huot, Y. Ma, R. Cieplicki, S. Cole, M. Karrenbach and B. L. Biondi, 'A Seismic Shift in Scalable Acquisition Demands New Processing: Fiber-Optic Seismic Signal Retrieval in Urban Areas with Unsupervised Learning for Coherent Noise Removal,' en, *IEEE Signal Processing Magazine*, vol. 35, no. 2, pp. 31–40, Mar. 2018, ISSN: 1053-5888. DOI: 10.1109/MSP.2017.2783381. [Online]. Available: http://ieeexplore.ieee.org/document/8310692/ (visited on 26/08/2020).

[23] S. Kowarik, M.-T. Hussels, S. Chruscicki, S. Münzenberger, A. Lämmerhirt, P. Pohl and M. Schubert, 'Fiber Optic Train Monitoring with Distributed Acoustic Sensing: Conventional and Neural Network Data Analysis,' en, *Sensors*, vol. 20, no. 2, p. 450, Jan. 2020, ISSN: 1424-8220. DOI: 10.3390/s20020450. [Online]. Available: https://www.mdpi.com/1424-8220/20/2/450 (visited on 26/08/2020).

[24] N. J. Lindsey, S. Yuan, A. Lellouch, L. Gualtieri, T. Lecocq and B. Biondi, 'City-Scale Dark Fiber DAS Measurements of Infrastructure Use During the COVID-19 Pandemic,' en, *Geophysical Research Letters*, vol. 47, no. 16, Aug. 2020, ISSN: 0094-8276, 1944-8007. DOI: 10.1029/2020GL089931. [Online]. Available: https://onlinelibrary.wiley.com/doi/abs/10.1029/2020GL089931 (visited on 26/08/2020).

[25] F. Walter, D. Gräff, F. Lindner, P. Paitz, M. Köpfli, M. Chmiel and A. Fichtner, 'Distributed acoustic sensing of microseismic sources and wave propagation in glaciated terrain,' en, *Nature Communications*, vol. 11, no. 1, p. 2436, Dec. 2020, ISSN: 2041-1723. DOI: 10.1038/s41467-020-15824-6. [Online]. Available: http://www.nature.com/articles/s41467-020-15824-6 (visited on 13/09/2020).

[26] T. Zhu, J. Shen and E. R. Martin, 'Sensing Earth and environment dynamics by telecommunication fiber-optic sensors: An urban experiment in Pennsylvania, USA,' en, *Solid Earth*, vol. 12, no. 1, pp. 219–235, Jan. 2021, ISSN: 1869-9529. DOI: 10.5194/se-12-219-2021. [Online]. Available: https://se.copernicus.org/articles/12/219/2021/ (visited on 22/04/2021).

[27] J. Ajo-Franklin, S. Dou, T. Daley, B. Freifeld, M. Robertson, C. Ulrich, T. Wood, I. Eckblaw, N. Lindsey, E. Martin and A. Wagner, 'Time-lapse surface wave monitoring of permafrost thaw using distributed acoustic sensing and a permanent automated seismic source,' en, in *SEG Technical Program Expanded Abstracts 2017*, Houston, Texas: Society of Exploration Geophysicists, Aug. 2017, pp. 5223–5227. DOI: 10.1190/segam2017-17774027.1. [Online]. Available: http://library.seg.org/doi/10.1190/segam2017-17774027.1 (visited on 26/08/2020).

[28] A. Sladen, D. Rivet, J. P. Ampuero, L. De Barros, Y. Hello, G. Calbris and P. Lamare, 'Distributed sensing of earthquakes and ocean-solid Earth interactions on seafloor telecom cables,' en, *Nature Communications*, vol. 10, no. 1, p. 5777, Dec. 2019, ISSN: 2041-1723. DOI: 10.1038/s41467-019-13793-z. [Online]. Available: http://www.nature.com/articles/s41467-019-13793-z (visited on 22/05/2020).

[29] E. F. Williams, M. R. Fernández-Ruiz, R. Magalhaes, R. Vanthillo, Z. Zhan, M. González-Herráez and H. F. Martins, 'Distributed sensing of microseisms and teleseisms with submarine dark fibers,' en, *Nature Communications*, vol. 10, no. 1, p. 5778, Dec. 2019, ISSN: 2041-1723. DOI: 10.1038/s41467-019-13262-7. [Online]. Available: http://www.nature.com/articles/s41467-019-13262-7 (visited on 07/06/2020).

[30] N. J. Lindsey, T. C. Dawe and J. B. Ajo-Franklin, 'Illuminating seafloor faults and ocean dynamics with dark fiber distributed acoustic sensing,' en, *Science*, vol. 366, no. 6469, pp. 1103–1107, Nov. 2019, ISSN: 0036-8075, 1095-9203. DOI: 10.1126/science.aay5881. [Online]. Available: https://www.sciencemag.org/lookup/doi/10.1126/science.aay5881 (visited on 26/08/2020).

[31] A. Bakulin, I. Silvestrov and R. Pevzner, 'Surface Seismic with DAS Changes Land Acquisition,' en, in *SPE Middle East Oil and Gas Show and Conference*, Manama, Bahrain: Society of Petroleum Engineers, 2019. DOI: 10.2118/194950-MS. [Online]. Available: http://www.onepetro.org/doi/10.2118/194950-MS (visited on 20/12/2020).

[32] M. Urosevic, A. Bona, S. Ziramov, R. Pevzner, K. Tertyshnikov, R. Martin, J. Dwyer, D. Felding, C. Guarin and A. Foley, 'Seismic Exploration of Mineral Resources in Western Australia with Distribute Acoustic Sensing,' en, in *25th European Meeting of Environmental and Engineering Geophysics*, The Hague, Netherlands, European Association of Geoscientists & Engineers, 2019, pp. 1–5. DOI: 10.3997/2214-4609.201902377. [Online]. Available: https://www.earthdoc.org/content/papers/10.3997/2214-4609.201902377 (visited on 19/01/2021).

[33] A. Bakulin, I. Silvestrov and R. Pevzner, 'Surface seismics with DAS: An emerging alternative to modern point-sensor acquisition,' *The Leading Edge*, vol. 39, no. 11, pp. 808–818, Nov. 2020, Publisher: Society of Exploration Geophysicists, ISSN: 1070-485X. DOI: 10.1190/tle39110808.1. [Online]. Available: https://doi.org/10.1190/tle39110808.1 (visited on 25/01/2021).

[34] A. Chadwick, G. Williams, N. Delepine, V. Clochard, K. Labat, S. Sturton, M.-L. Buddensiek, M. Dillen, M. Nickel, A. L. Lima, R. Arts, F. Neele and G. Rossi, 'Quantitative analysis of time-lapse seismic monitoring data at the Sleipner CO2 storage operation,' en, *The Leading Edge*, vol. 29, no. 2, pp. 170–177, Feb. 2010, ISSN: 1070-485X, 1938-3789. DOI: 10.1190/1.

3304820. [Online]. Available: https://library.seg.org/doi/10.1190/1.3304820 (visited on 25/11/2021).

[35] M. Landrø, '4D seismic,' in *Petroleum geoscience: From sedimentary environments to rock physics*, K. Bjørlykke, Ed., Berlin, Heidelberg: Springer Berlin Heidelberg, 2015, pp. 489–514, ISBN: 978-3-642-34132-8. [Online]. Available: https://doi.org/10.1007/978-3-642-34132-8_19.

[36] N. Hodgson, 'Inversion for reservoir pressure change using overburden strain measurements determined from 4D seismic,' en, PhD thesis, Heriot-Watt University, Edinburgh, Scotland, Jan. 2009. [Online]. Available: http://hdl.handle.net/10399/2320.

[37] J. Rickett, L. Duranti, T. Hudson, B. Regel and N. Hodgson, '4D time strain and the seismic signature of geomechanical compaction at Genesis,' *The Leading Edge*, vol. 26, no. 5, pp. 644–647, May 2007, ISSN: 1070-485X. DOI: 10.1190/1.2737103. [Online]. Available: https://doi.org/10.1190/1.2737103 (visited on 27/06/2022).

[38] J. Guilbot and B. Smith, '4-D constrained depth conversion for reservoir compaction estimation: Application to Ekofisk Field,' en, *The Leading Edge*, vol. 21, no. 3, pp. 302–308, Mar. 2002, ISSN: 1070-485X, 1938-3789. DOI: 10.1190/1.1463782. [Online]. Available: http://library.seg.org/doi/10.1190/1.1463782 (visited on 07/02/2020).

[39] C. MacBeth, M.-D. Mangriotis and H. Amini, 'Review Paper: Post-stack 4D seismic time-shifts: Interpretation and evaluation,' en, *Geophysical Prospecting*, vol. 67, no. 1, pp. 3–31, Dec. 2019, ISSN: 0016-8025, 1365-2478. DOI: 10.1111/1365-2478.12688. [Online]. Available: https://onlinelibrary.wiley.com/doi/abs/10.1111/1365-2478.12688 (visited on 02/05/2020).

[40] W. Zhou and D. Lumley, 'Central-difference time-lapse 4D seismic full-waveform inversion,' *GEOPHYSICS*, vol. 86, no. 2, R161–R172, Mar. 2021, ISSN: 0016-8033. DOI: 10.1190/geo2019-0834.1. [Online]. Available: https://doi.org/10.1190/geo2019-0834.1 (visited on 28/06/2022).

[41] O. H. Waagaard, E. Rønnekleiv, A. Haukanes, F. Stabo-Eeg, D. Thingbø, S. Forbord, S. E. Aasen and J. K. Brenne, 'Real-time low noise distributed acoustic sensing in 171 km low loss fiber,' en, *OSA Continuum*, vol. 4, no. 2, pp. 688–701, Feb. 2021, ISSN: 2578-7519. DOI: 10.1364/OSAC.408761. [Online]. Available: https://www.osapublishing.org/abstract.cfm?URI=osac-4-2-688 (visited on 11/01/2022).

[42] M. Landrø, L. Bouffaut, H. J. Kriesell, J. R. Potter, R. A. Rørstadbotnen, K. Taweesintananon, S. E. Johansen, J. K. Brenne, A. Haukanes, O. Schjelderup and F. Storvik, 'Sensing whales, storms, ships and earthquakes using an Arctic fibre optic cable,' *Scientific Reports*, vol. 12, no. 1, p. 19 226, Nov. 2022, ISSN: 2045-2322. DOI: 10.1038/s41598-022-23606-x. [Online]. Available: https://doi.org/10.1038/s41598-022-23606-x.

[43] I. Lior, A. Sladen, D. Mercerat, J.-P. Ampuero, D. Rivet and S. Sambolian, 'Strain to ground motion conversion of distributed acoustic sensing data for earthquake magnitude and stress drop determination,' *Solid Earth*, vol. 12, no. 6, pp. 1421–1442, Jun. 2021, ISSN: 1869-9529. DOI: 10.5194/se-12-1421-2021. [Online]. Available: https://se.copernicus.org/articles/12/1421/2021/.

[44] R. Stull, *Practical meteorology: An algebra-based survey of atmospheric science*, en, Version 1.02b. Vancouver, Canada: University of British Columbia, 2017, ISBN: 978-0-88865-283-6. [Online]. Available: https://www.eoas.ubc.ca/books/Practical_Meteorology/.

[45] E. Robein, *Velocities, time-imaging and depth-imaging: Principles and methods*, en, 3rd ed. European Association of Geoscientists & Engineers, 2010, ISBN: 978-94-6282-014-2. [Online]. Available: https://www.earthdoc.org/content/books/9789462820142.

[46] W. C. Crawford, S. C. Webb and J. A. Hildebrand, 'Seafloor compliance observed by long-period pressure and displacement measurements,' *Journal of Geophysical Research: Solid Earth*, vol. 96, no. B10, pp. 16 151–16 160, Sep. 1991, ISSN: 0148-0227. DOI: 10.1029/91JB01577. [Online]. Available: https://doi.org/10.1029/91JB01577 (visited on 08/09/2022).

[47] Bakku, Sudhish Kumar, 'Fracture characterization from seismic measurements in a borehole,' en, PhD, Massachusetts Institute of Technology, Department of Earth, Atmospheric, and Planetary Sciences, 2015. [Online]. Available: http://hdl.handle.net/1721.1/97331.

[48] A. Bertholds and R. Dandliker, 'Determination of the individual strain-optic coefficients in single-mode optical fibres,' *Journal of Lightwave Technology*, vol. 6, no. 1, pp. 17–20, Jan. 1988, ISSN: 1558-2213. DOI: 10.1109/50.3956.

[49] C. MacBeth, H. Amini and S. Izadian, 'Review paper: Methods of measurement for 4D seismic post-stack time shifts,' *Geophysical Prospecting*, vol. 68, no. 9, pp. 2637–2664, Nov. 2020, ISSN: 0016-8025. DOI: 10.1111/1365-2478.13022. [Online]. Available: https://doi.org/10.1111/1365-2478.13022 (visited on 27/06/2022).

[50] M. Landrø and J. Stammeijer, 'Quantitative estimation of compaction and velocity changes using 4D impedance and traveltime changes,' en, *GEOPHYSICS*, vol. 69, no. 4, pp. 949–957, Jul. 2004, ISSN: 0016-8033, 1942-2156. DOI: 10.1190/1.1778238. [Online]. Available: https://library.seg.org/doi/10.1190/1.1778238 (visited on 07/02/2020).

[51] P. K. T. Nguyen, 'Estimation of time-lapse velocity changes from time-lapse seismic data,' en, PhD thesis, Heriot-Watt University, Edinburgh, Scotland, Aug. 2018. [Online]. Available: http://hdl.handle.net/10399/3969.

[52] P. J. Hatchell and S. J. Bourne, 'Measuring reservoir compaction using time-lapse timeshifts,' in *SEG Technical Program Expanded Abstracts 2005*, ser. Expanded Abstracts, Society of Exploration Geophysicists, Jan. 2005, pp. 2500–2503. DOI: 10.1190/1.2148230. [Online]. Available: https://doi.org/10.1190/1.2148230 (visited on 03/04/2020).

[53] T. Røste, A. Stovas and M. Landrø, 'Estimation of layer thickness and velocity changes using 4D prestack seismic data,' in *67th EAGE Conference & Exhibition*, ser. Conference Proceedings, cp-1-00583: European Association of Geoscientists & Engineers, Jun. 2005, pp. 1–4, ISBN: 2214-4609. DOI: 10.3997/2214-4609-pdb.1.C010. [Online]. Available: https://www.earthdoc.org/content/papers/10.3997/2214-4609-pdb.1.C010.

[54] A. P. Bathija, M. L. Batzle and M. Prasad, 'An experimental study of the dilation factor,' *GEOPHYSICS*, vol. 74, no. 4, E181–E191, Jul. 2009, ISSN: 0016-8033. DOI: 10.1190/1.3137060. [Online]. Available: https://doi.org/10.1190/1.3137060 (visited on 28/06/2022).

[55] R. M. Holt, A. Bauer and A. Bakk, 'Stress-path-dependent velocities in shales: Impact on 4D seismic interpretation,' *GEOPHYSICS*, vol. 83, no. 6, MR353–MR367, Nov. 2018, ISSN: 0016-8033. DOI: 10.1190/geo2017-0652.1. [Online]. Available: https://doi.org/10.1190/geo2017-0652.1 (visited on 28/06/2022).

[56] T. Røste, A. Stovas and M. Landrø, 'Estimation of layer thickness and velocity changes using 4D prestack seismic data,' en, *GEOPHYSICS*, vol. 71, no. 6, S219–S234, Nov. 2006, ISSN: 0016-8033, 1942-2156. DOI: 10.1190/1.2335657. [Online]. Available: http://library.seg.org/doi/10.1190/1.2335657 (visited on 31/03/2020).

[57] S. Izadian and C. MacBeth, 'Measurement, interpretation and value of pre-stack time-shifts in a North Sea dataset,' in *83rd EAGE Annual Conference & Exhibition*, ser. Conference Proceedings, vol. 2022, Madrid, Spain: European Association of Geoscientists & Engineers, 2022, pp. 1–5. DOI: 10.3997/2214-4609.202210714. [Online]. Available: https://www.earthdoc.org/content/papers/10.3997/2214-4609.202210714.

[58] I. Dvorak, C. MacBeth and H. Amini, 'Evaluating 4D overburden velocity perturbation for the Shearwater Field via pre-stack time-shift inversion,' en, in *80th EAGE Conference and Exhibition*, ser. Conference Proceedings, vol. 2018, Copenhagen, Denmark: European Association of Geoscientists & Engineers, Jun. 2018, pp. 1–5, ISBN: 2214-4609. DOI: 10.3997/2214-4609.201800699. [Online]. Available: http://www.earthdoc.org/publication/publicationdetails/?publication=92086 (visited on 09/10/2020).

[59] S. Izadian and C. MacBeth, 'Exploring value in pre-stack time-shifts with Ekofisk PRM data,' en, in *82nd EAGE Annual Conference & Exhibition*, ser. Conference Proceedings, vol. 2021, Amsterdam, The Netherlands, European Association of Geoscientists & Engineers, 2021, pp. 1–5. DOI: 10.3997/

2214-4609.202112553. [Online]. Available: https://www.earthdoc.org/content/papers/10.3997/2214-4609.202112553 (visited on 04/10/2021).

[60] A. Ghaderi and M. Landrø, 'Estimation of thickness and velocity changes of injected carbon dioxide layers from prestack time-lapse seismic data,' en, *GEOPHYSICS*, vol. 74, no. 2, O17–O28, Mar. 2009, ISSN: 0016-8033, 1942-2156. DOI: 10.1190/1.3054659. [Online]. Available: http://library.seg.org/doi/10.1190/1.3054659 (visited on 18/02/2020).

[61] J. Herwanger, E. Palmer and C. R. Schiøtt, 'Anisotropic velocity changes in seismic time-lapse data,' en, in *SEG Technical Program Expanded Abstracts 2007*, ser. Expanded Abstracts, Society of Exploration Geophysicists, Jan. 2007, pp. 2883–2887. DOI: 10.1190/1.2793065. [Online]. Available: http://library.seg.org/doi/abs/10.1190/1.2793065 (visited on 17/09/2020).

[62] J. V. Herwanger and S. A. Horne, 'Linking reservoir geomechanics and time-lapse seismics: Predicting anisotropic velocity changes and seismic attributes,' en, *GEOPHYSICS*, vol. 74, no. 4, W13–W33, Jul. 2009, ISSN: 0016-8033, 1942-2156. DOI: 10.1190/1.3122407. [Online]. Available: http://library.seg.org/doi/10.1190/1.3122407 (visited on 12/02/2020).

[63] K. Taweesintananon, M. Landrø, J. K. Brenne and A. Haukanes, 'Distributed acoustic sensing for near-surface imaging using submarine telecommunication cable: A case study in the Trondheimsfjord, Norway,' en, *GEOPHYSICS*, vol. 86, no. 5, B303–B320, Sep. 2021, ISSN: 0016-8033, 1942-2156. DOI: 10.1190/geo2020-0834.1. [Online]. Available: https://library.seg.org/doi/10.1190/geo2020-0834.1 (visited on 03/05/2022).

[64] L. Bouffaut, K. Taweesintananon, H. J. Kriesell, R. Rørstadbotnen, J. R. Potter, M. Landrø, S. E. Johansen, J. K. Brenne, A. Haukanes, O. Schjelderup and F. Storvik, 'Eavesdropping at the speed of light: Distributed acoustic sensing of baleen whales in the Arctic,' en, *Frontiers in Marine Science*, vol. 9, p. 901 348, 2022. DOI: 10.3389/fmars.2022.901348. [Online]. Available: https://www.frontiersin.org/articles/10.3389/fmars.2022.901348/full (visited on 01/07/2022).

[65] K. Taweesintananon, M. Landrø, J. R. Potter, S. E. Johansen, R. A. Rørstadbotnen, L. Bouffaut, H. J. Kriesell, J. K. Brenne, A. Haukanes, O. Schjelderup and F. Storvik, 'Distributed acoustic sensing of ocean-bottom seismoacoustics and distant storms: A case study from Svalbard, Norway,' *GEOPHYSICS*, vol. 88, no. 3, B135–B150, May 2023, ISSN: 0016-8033. DOI: 10.1190/geo2022-0435.1. [Online]. Available: https://doi.org/10.1190/geo2022-0435.1 (visited on 29/04/2023).

[66] K. Taweesintananon, M. Landrø, S. Narongsirikul and P. G. Folstad, 'Angle-dependent 4D seismic time-strain inversion for estimating subsurface thickness and velocity changes,' en, Unpublished manuscript, Trondheim, Norway, 2023.

[67] R. A. Rørstadbotnen, J. Eidsvik, L. Bouffaut, M. Landrø, J. Potter, K. Taweesintananon, S. Johansen, F. Storevik, J. Jacobsen, O. Schjelderup, S. Wienecke, T. A. Johansen, B. O. Ruud, A. Wuestefeld and V. Oye, 'Simultaneous tracking of multiple whales using two fiber-optic cables in the Arctic,' *Frontiers in Marine Science*, vol. 10, p. 1 130 898, 2023, ISSN: 2296-7745. DOI: 10.3389/fmars.2023.1130898. [Online]. Available: https://www.frontiersin.org/articles/10.3389/fmars.2023.1130898.

[68] R. A. Rørstadbotnen, M. Landrø, K. Taweesintananon, L. Bouffaut, J. Potter, S. E. Johansen, H. J. Kriesell, J. K. Brenne, A. Haukanes, O. Schjelderup and F. Storvik, 'Analysis of a local earthquake in the Arctic using a 120 km long fibre-optic cable,' en, in *83rd EAGE Annual Conference & Exhibition*, ser. Conference Proceedings, vol. 2022, Madrid, Spain: European Association of Geoscientists & Engineers, 2022, pp. 1–5. DOI: 10.3997/2214-4609.202210404. [Online]. Available: https://www.earthdoc.org/content/papers/10.3997/2214-4609.202210404.

[69] K. Taweesintananon, M. Landrø, S. Narongsirikul and P. G. Folstad, 'Angle-variant 4D seismic time-shift analysis for velocity change and subsurface strain estimation,' en, in *83rd EAGE Annual Conference & Exhibition*, ser. Conference Proceedings, vol. 2022, Madrid, Spain: European Association of Geoscientists & Engineers, 2022, pp. 1–5. DOI: 10.3997/2214-4609.202210437. [Online]. Available: https://www.earthdoc.org/content/papers/10.3997/2214-4609.202210437.

Paper I

Citation information:

K. Taweesintananon, M. Landrø, J. K. Brenne and A. Haukanes, 'Distributed acoustic sensing for near-surface imaging using submarine telecommunication cable: A case study in the Trondheimsfjord, Norway,' en, *GEOPHYSICS*, vol. 86, no. 5, B303–B320, Sep. 2021, ISSN: 0016-8033, 1942-2156. DOI: 10.1190/geo2020-0834.1. [Online]. Available: https://library.seg.org/doi/10.1190/geo2020-0834.1 (visited on 03/05/2022)

Summary:

Taweesintananon et al. compare the near-surface seismic images from a hydrophone array and distributed acoustic sensing (DAS) applied to a submarine telecommunication cable in Trondheimsfjord, Norway. Their study shows enormous potential of DAS applications for marine seismic exploration.

Contributions:

M.L. and J.K.B. conceived and designed the experiment. K.T., M.L. and A.H. collected data. K.T. developed methodology, processed data and prepared visualisations. K.T. and M.L. analysed the data with support from J.K.B. M.L. validated research outputs, acquired funding, and managed the project. K.T. wrote the original draft of the manuscript. All the authors conducted review and editing of the manuscript.

GEOPHYSICS, VOL. 86, NO. 5 (SEPTEMBER-OCTOBER 2021); P. B303–B320, 20 FIGS.
10.1190/GEO2020-0834.1

Case History

Distributed acoustic sensing for near-surface imaging using submarine telecommunication cable: A case study in the Trondheimsfjord, Norway

Kittinat Taweesintananon[1], Martin Landrø[2], Jan Kristoffer Brenne[3], and Aksel Haukanes[3]

ABSTRACT

Distributed acoustic sensing (DAS) transforms submarine telecommunication cables into densely sampled seismic receivers. To demonstrate DAS applications for seismic imaging, we have used an optical cable on the seafloor in the Trondheimsfjord, Norway, to record seismic data generated by a controlled seismic source. The data are simultaneously recorded by a towed hydrophone array and the fiber-optic cable. Following our data processing methods, we can produce seismic images of the seafloor and underlying geologic structures from the hydrophone array and DAS data. We find that the hydrophone and DAS data have a comparable signal-to-noise ratio. Moreover, DAS images can be improved by using a seismic source that has sufficiently large energy within the frequency range matching the spatial resolution of DAS. The temporal resolution of the DAS images can be improved by minimizing the crossline offset between seismic sources and the DAS cable. The seismic images from DAS can be used to support geohazard analysis and various subsurface exploration activities.

INTRODUCTION

Near-surface seismic imaging is essential for investigating shallow gas, weak layers, faults, and other potential subsurface geologic hazards. These elements can adversely affect offshore activities such as drilling operations, offshore platform and wind farm construction, and pipeline surveys. The oil and gas industry uses near-surface information to improve the images of deeper structures and to reduce risks in exploration and production. To accurately investigate near-surface irregularities, ultrahigh-resolution reflection seismic data acquisition and processing techniques have been developed (Monrigal et al., 2017).

Marine seismic data can be recorded either by hydrophone streamers towed behind sailing vessels or by seismic receivers deployed on the seafloor. Seismic reflections from near-surface structures are strongest at the receivers with short offsets from the source. To acquire near-offset seismic data, we may place the source over the streamer spread, which requires separate vessels for sources and streamers (Vinje et al., 2017). Another solution is to minimize the distance between sources and dense streamers (Thomas et al., 2012; Monrigal et al., 2017). However, the latter solution requires shortening the streamer length for operation safety. The lack of far-offset information consequently causes high uncertainty in velocity model building. However, short offsets and dense receiver spacing in streamers result in high stacking fold and narrow imaging bins for near-surface imaging. Hence, when combined with high-frequency seismic sources, the vertical and horizontal resolution becomes significantly higher than conventional broadband seismic data.

Seabed seismic acquisition has been growing in the marine seismic market for its advantages over towed-streamer techniques. The physics of seabed seismic acquisition is more advantageous than towed-streamer acquisition for the following reasons (Landrø and Amundsen,

Manuscript received by the Editor 24 November 2020; revised manuscript received 26 April 2021; published ahead of production 15 June 2021; published online 18 August 2021.
[1]NTNU – Norwegian University of Science and Technology, Department of Electronic Systems, Faculty of Information Technology and Electrical Engineering, Trondheim 7491, Norway; PTT Exploration and Production Public Company Limited, Bangkok 10900, Thailand. E-mail: kittinat.taweesintananon@ntnu.no (corresponding author).
[2]NTNU – Norwegian University of Science and Technology, Department of Electronic Systems, Faculty of Information Technology and Electrical Engineering, Trondheim 7491, Norway. E-mail: martin.landro@ntnu.no.
[3]Alcatel Submarine Networks Norway AS, Vestre Rosten 77, Tiller 7075, Norway. E-mail: jan.kristoffer.brenne@asn.com; aksel.haukanes@asn.com.

DOI:10.1190/geo2020-0834.1

2018). First, seafloor receivers have a lower noise level than towed streamers. Second, there are no limits to the offsets and azimuths between sources and receivers, except for source-vessel considerations. Long offsets and wide azimuths in the data can significantly improve the accuracy of seismic velocity models and the seismic illumination of complex structures. Third, pressure and shear waves are recorded, so a seafloor receiver geometry can provide high-quality images even in areas with strong amplitude absorption in the presence of gas. Finally, there are fewer effects from the sea-surface ghosts that limit the frequency bandwidth of the seismic data and, hence, the image resolution.

Ocean-bottom cables and ocean-bottom nodes are common recording systems in the seabed seismic market. The node system is a blind recording system, because it acquires data internally and exports the data later. In addition, nodes are powered by internal batteries, which requires an effective power management plan during the operation. In contrast, data recorded by ocean-bottom cables can be viewed on a real-time basis. Traditional cable systems for seabed seismic acquisition are bulky electronic networks. However, the electrical cables can be replaced with fiber-optic sensing cables, while maintaining the recording performance (Langhammer et al., 2010). In addition to the real-time monitoring feature, a key advantage of fiber-optic sensing systems is that no electronic or electrical power components are required at the sensing points giving unsurpassed reliability for permanently installed sensing systems.

Distributed acoustic sensing (DAS) is an emerging technology that uses fiber-optic cables for acoustic measurements. It has been applied to military defense, engineering structure monitoring, and petroleum exploration (Wang et al., 2019). DAS transforms a fiber-optic cable into a densely sampled sensor array. The cable itself is the sensing element without additional transducers in the optical path. Laser pulses transmitted into the fiber are continuously reflected to the interrogator due to the Rayleigh backscattering process inherent to all optical fibers. The phase of the backscattered light is reconstructed within the interrogator typically for each meter of the fiber. Because the phase of the reflected optical light is proportional to the strain of the fiber, the distributed strain modulation across a fiber segment (called the gauge length) can be computed. Therefore, DAS can sense seismic waves that modulate the extensional strain of the fiber segment (Hartog, 2017). Its seismic response is somewhat similar to the inline component of conventional point accelerometers. In other words, it is mainly sensitive to seismic waves creating strain along the cable direction (Kuvshinov, 2016; Papp et al., 2017).

Over the past decade, many applications of DAS have been studied and introduced to the applied seismology community and the petroleum industry. Daley et al. (2013) demonstrate a field test of DAS seismic acquisition of borehole seismic data and land surface-seismic data. In addition, Dean et al. (2016) discuss its applications to marine seismic acquisition. Lumens (2014) studies various applications of DAS in oil and gas wells. In addition to borehole applications, DAS can be applied to fiber-optic telecommunication cables deployed on the ground and on the seafloor. Many case studies of DAS using onshore telecommunication infrastructure have been conducted for passive seismic monitoring such as earthquake detection (Biondi et al., 2017; Ajo-Franklin et al., 2019; Yu et al., 2019; Fernández-Ruiz et al., 2020), near-surface soil studies (Dou et al., 2017; Fang et al., 2020), ambient noise analysis (Ajo-Franklin et al., 2015; Martin et al., 2017, 2018), urban traffic monitoring (Kowarik et al., 2020; Lindsey et al., 2020), glacier flow monitoring (Walter et al., 2020), and other seismic activities (Zhu et al., 2021). Moreover, it can monitor seismic waves from controlled sources to study and prevent onshore geohazards (Ajo-Franklin et al., 2017). In addition to onshore environments, DAS in underwater telecommunication fibers can detect ocean waves, microseisms, earthquakes (Sladen et al., 2019; Williams et al., 2019), and near-surface geologic structures and faults (Lindsey et al., 2019).

DAS can be used as surface-seismic receivers in subsurface exploration. Bakulin et al. (2019) and Urosevic et al. (2019) demonstrate the potential applications of DAS to land seismic exploration. A comprehensive review of the recent DAS technology for land surface-seismic surveys is given in Bakulin et al. (2020). Nevertheless, the applications of DAS to produce subsurface-seismic images in a marine environment have not been widely presented. It is important to acquire multifold and diverse examples to verify that DAS can be used for subsurface-seismic exploration in any environment. This statement could be demonstrated by comparing the marine seismic images from DAS with those from other conventional seismic methods. The validity of DAS in marine seismic exploration has potential in the seabed seismic market.

This article demonstrates seabed seismic applications of DAS for near-surface seismic imaging. The experiment is done by using an existing submarine telecommunication cable in the Trondheimsfjord, Norway. We first use DAS to record seismic waves generated from a bubble gun towed near the sea surface. Then, we analyze and process the data to produce seismic images of the seafloor and its underlying geologic structures. Then, the results are compared to the seismic data simultaneously recorded by a conventional towed hydrophone array. Finally, we discuss the requirements and limitations of DAS for seabed seismic acquisition and subsurface imaging.

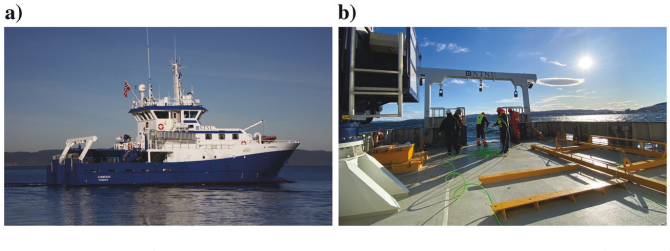

Figure 1. Photos of (a) NTNU's research vessel *Gunnerus* (photo courtesy of Port of Trondheim IKS) and (b) the crew in action to recover the HMS-620 BubbleGun source.

EXPERIMENTAL SETUP AND DATA ACQUISITION

We conduct a marine seismic survey in the Trondheimsfjord using NTNU's research vessel, the R/V *Gunnerus*, as shown in Figure 1. A single marine seismic source and a single-channel hydrophone streamer are towed behind the vessel. The seismic data from the streamer are recorded by the HMS-620 BubbleGun recording system with sub-bottom sonar interface software from National Instruments. Simultaneously, we record the seismic

data using an OptoDAS interrogator connected to a dark fiber in a seafloor telecommunication cable. The OptoDAS interrogator, which was developed by Alcatel Submarine Networks, is based on the use of linear frequency-modulated optical pulses (Waagaard et al., 2021). The DAS data are continuously recorded throughout the survey program. The map of the source line and DAS cable is shown in Figure 2.

The seismic recording system of the vessel consists of an HMS-620 Bubble Pulser electric seismic source and a short hydrophone streamer with 7 m of a single-channel array comprising 24 elements. The source and streamer are towed approximately 20 m behind the vessel's reference position, and they are separated by 10 m perpendicular to the sail line. The source and streamer depths are approximately 1 m below the sea surface. The recording time sampling interval is 0.25 ms, and the maximum recording time for each shot is 266.25 ms. The recording start time is synchronized with the gun firing time. The layout diagram of the source and streamer towed behind the vessel is shown in Figure 3.

The acoustic source energy is approximately 50 J, which is equivalent to 200 dB relative to the reference pressure 1 μPa at reference distance 1 m. The frequency bandwidth ranges from 350 to 1000 Hz at 10 dB down, in which the dominant frequency is approximately 600 Hz. The shot time interval, namely, the gun firing time interval, is set to 267.75 ms in the system. Our analysis shows that the actual shot time interval is slightly shorter than this value due to instrument errors. The actual shot time interval estimated by our calibration method is approximately 267.67 ms. The vessel is navigated as close to the DAS cable as possible. The vessel speed averages 2 knots to acquire high-density seismic data with minimal noise from the vessel's propulsion. Hence, the average shotpoint interval is approximately 0.275 m.

The DAS recording system is independent of the vessel's equipment. The OptoDAS interrogator is connected to one end of the telecommunication cable in Trondheim. The cable was already laid into the soft sediments at approximately 0–2 m below the seafloor of the Trondheimsfjord from Trondheim to Kvithylla. An SMF-28 single-mode silica fiber in the cable is used in our experiment. The interrogation is performed by sending frequency-swept light pulses into the sensing fiber. Then, the light pulses are backscattered at the inherent anomalies presented in the fiber due to Rayleigh backscattering. After receiving the backscattered pulses, the OptoDAS interrogator calculates the time-differentiated phase change of the backscattered response from consecutive sweeps for each sampled fiber position. Thereafter, the recorded time-differentiated phase change can be converted to the longitudinal strain of the corresponding fiber section. The DAS data are continuously recorded using a 0.44 ms time-sampling interval throughout the survey. The channel spacing is 2.04 m, whereas the gauge length is 4.08 m.

DAS recording system

In this experiment, we repeatedly send light pulses with a free-space wavelength (λ_o) of 1550 nm, in which the sampling period at the optical receiver ($\Delta\tau$) is 1×10^{-8} s. The spatial sampling interval (SSI) is defined by the sampling period as

$$\mathrm{SSI} = \left(\frac{c}{2n_g}\right)\Delta\tau, \tag{1}$$

where $c \approx 3 \times 10^8$ m/s is the speed of light in vacuum and $n_g \approx 1.47$ is the refractive group index of the SMF-28 fiber. Hence, SSI $\approx$ 1.02 m.

Let ϕ_x be the phase of the light backscattered from the spatial sampling location x, which can be expressed in radians as

$$\phi_x = \frac{4\pi n_g x}{\lambda_o}. \tag{2}$$

The interrogator extracts the rate of phase change between consecutive time samples associated with this location, namely, the time-differentiated phase ($\dot{\phi}_x$). In this study, the time-sampling interval (Δt) is 0.44 ms, which is defined by the cable length of 44 km. The SSI is decimated to the desired spatial resolution by applying a spatial moving average to the time-differentiated phase ($\dot{\phi}_{\mathrm{avg},x}$) around the location x. In this experiment, the resolution is calculated by averaging across four spatial samples ($N_{\mathrm{avg}} = 4$) to achieve a full width at half maximum ($L_W = N_{\mathrm{avg}} \times \mathrm{SSI}$), that is, $L_W \approx 4.08$ m. Then, the difference of the average time-differentiated phases between the two spatial locations separated by four spatial samples ($N_{\Delta\tau} = 4$) is defined as the time-differentiated phase change ($\Delta\dot{\phi}_x$):

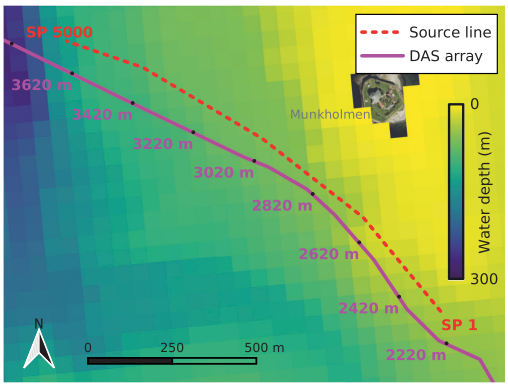

Figure 2. Source and receiver location map of the marine seismic survey in the Trondheimsfjord, Norway. The vessel route (the dashed red line) is controlled to be as close to the DAS receiver cable (the solid magenta line) as possible. The receiver positions are annotated as the distance along the DAS cable. The background water depth map is shown courtesy of the Kartverket (Norwegian Mapping Authority).

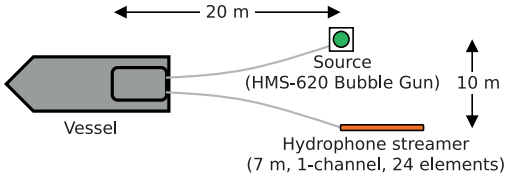

Figure 3. Top view of the acquisition layout. The source and the streamer are towed approximately 20 m behind the R/V *Gunnerus*. The diagram is not to scale.

$$\Delta\dot{\phi}_x = \dot{\phi}_{\text{avg},x+L_G/2} - \dot{\phi}_{\text{avg},x-L_G/2}, \tag{3}$$

where $L_G = N_{\Delta\tau} \times \text{SSI}$ is the gauge length; hence, $L_G \approx 4.08$ m. The gauge length is an acquisition parameter that affects the signal-to-noise ratio (S/N) and the spatial resolution of the raw DAS data (Dean et al., 2017).

The longitudinal strain rate ($\dot{\varepsilon}_{xx,x}$) of the fiber section can be derived from the time-differentiated phase change by

$$\dot{\varepsilon}_{xx,x} = \frac{\lambda_o}{4\pi n_g \zeta L_G}\Delta\dot{\phi}_x, \tag{4}$$

where ζ is the strain-optic coefficient described by

$$\zeta = 1 - \frac{n_g^2}{2}[P_{12} - \nu(P_{11} + P_{12})], \tag{5}$$

where P_{11} and P_{12} are the Pockel photoelastic constants and ν is the Poisson's ratio of the fiber material (Bertholds and Dandliker, 1988; Hartog, 2017). In this experiment, we use $\zeta \approx 0.78$ for the silica fiber.

Thus, the longitudinal strain ($\varepsilon_{xx,x}$) of the fiber section can be determined by integrating the strain rate along the time axis, that is,

$$\varepsilon_{xx,x} = \int_0^t \dot{\varepsilon}_{xx,x} dt. \tag{6}$$

In addition, the maximum number of recording channels is given by $\Delta t/\Delta\tau$, which is 44,000 channels along the cable length of 44 km. In this experiment, we extract only 10,500 channels sampled at every 2.04 m from 0 to 21 km from the optical circulator for recording the time-differentiated phase change data. The extracted subsections of the data are defined by the regions of interest. In this case, the channel spacing is larger than SSI by a factor of two.

Strain-optic relation

Equation 4 can easily mislead. Because a constant strain-optic coefficient is used, equation 4 implies that the time-differentiated phase change is merely a function of the longitudinal deformation of the fiber. In fact, the strain-optic coefficient defined in equation 5 is implicitly affected by the longitudinal and transverse deformations of the fiber. The phase of the light in radians is defined as

$$\phi = 2\pi\left(\frac{L_o}{\lambda_o}\right), \tag{7}$$

where L_o and λ_o are the optical path length and wavelength in free space, respectively. The optical path length is defined as

$$L_o = n_g L = \left(\frac{c}{v_{ph}}\right)L, \tag{8}$$

where c is the speed of light in vacuum, v_{ph} is the speed of light in the fiber, and L is the distance traveled by the light inside the zone in which the interference effects are observed. Equation 8 also suggests that the change in the optical path length is caused by the changes of either the physical length of the fiber or the phase velocity of the light. The relative change of an optical path can be written as

$$\frac{\Delta L_o}{L_o} = \varepsilon_L - \frac{\Delta v_{ph}}{v_{ph}}, \tag{9}$$

where $\varepsilon_L = \Delta L/L$ is the fiber strain in the direction of the light propagation (Kuvshinov, 2016).

For backscattering measurement, two-way propagation of light along the fiber axis gives $L \approx 2x$. Here, we neglect the fiber birefringence and consider a linearly polarized beam. Thus, the optical strain is approximately equal to the longitudinal strain: $\varepsilon_L \approx \varepsilon_{xx} = \Delta x/x$. Moreover, we see from equation 7 that a phase change is fundamentally caused by an optical path change. Given light with constant wavelength, the phase change across the gauge length ($x = L_G$) can be written as a function of the optical path change:

$$\Delta\phi = \frac{2\pi}{\lambda_o}\Delta L_o \approx \frac{4\pi n_g L_G}{\lambda_o}\left(\frac{\Delta L_o}{L_o}\right). \tag{10}$$

Because the phase velocity of light depends on the dielectric tensor of the fiber, equation 9 for a uniform and isotropic material can be described by the Pockel constants as follows (Bakku, 2015; Kuvshinov, 2016):

$$\frac{\Delta L_o}{L_o} = \varepsilon_{xx} - \frac{n_g^2}{2}[(P_{11} - P_{44})\varepsilon_\perp + P_{12}\varepsilon_{xx}], \tag{11}$$

where $\varepsilon_\perp$ is the transverse fiber strain and $P_{12} = P_{11} - 2P_{44}$. For the parameters given by Kuvshinov (2016), equation 11 reduces to

$$\frac{\Delta L_o}{L_o} \approx 0.7\varepsilon_{xx} - 0.2\varepsilon_\perp. \tag{12}$$

This equation implies that the DAS signal based on a phase change method results from the strains in any direction.

For very small transverse stress ($\sigma_\perp \to 0$), the transverse fiber strain depends on the longitudinal strain by the Poisson effect (Kuvshinov, 2016):

$$\varepsilon_\perp = \varepsilon_{\perp,1} + \varepsilon_{\perp,2} \approx -2\nu\varepsilon_{xx}. \tag{13}$$

Then, the relative change of the optical path in a fiber is proportional to the physical longitudinal strain, that is,

$$\frac{\Delta L_o}{L_o} \approx \zeta\varepsilon_{xx}. \tag{14}$$

In this limit, the optical phase change is proportional to the longitudinal strain as described by equation 4. The linear relationship in equation 14 is currently the commonly accepted expression for the length change. It is also the basis of all practical DAS applications, whereas equation 12 is not widely adopted.

DATA CHARACTERISTICS

The seismic data recorded by the single-channel streamer can be displayed as a common channel gather as shown in Figure 4.

The data are formed by summing a linear array of 24 hydrophone elements within a 7 m streamer length into one recording channel. The data contain direct and reflected compressional waves (P-waves). The direct wave as marked by "A" does not propagate through the subsurface. Therefore, only the reflected waves are used to image the seafloor and subsurface geologic structures. In Figure 4, two strong seismic reflections are observed: the seafloor reflection marked by "B" and the crystalline bedrock reflection marked by "C." The stratigraphy between the seafloor and the bedrock should be divided into two units as described by L'Heureux et al. (2009). The lower unit comprises deposits of Allerød and Younger Dryas age overlying bedrock. The upper unit comprises Holocene deposits of bioturbated clay, silty, and sandy sediments, and it is overlain by poorly sorted sand with anthropogenic drops at the seafloor. However, the base Holocene reflection is not clearly observed in our data.

In contrast, the DAS data are continuously recorded. Each seismic trace corresponds to an individual recording channel resulting from the strain demodulation across a fiber segment of 4 m gauge length, in which the channel spacing is 2 m. To derive shot records for further analysis, every continuously recorded seismic trace is edited and broken into several shorter traces associated with different shot numbers. This trace editing requires the precise gun firing time of each shot, which is determined by the calibration method discussed in the next section.

Typical seismic profiles derived from DAS contain obvious hyperbolic events generated by our seismic sources. The data also contain low-frequency signals, as shown in Figure 5a, that might include surface waves. However, our study focuses on the direct and reflected P-waves, because the other source-generated waves such as surface waves and converted waves are incomparable to the streamer data. A simple band-pass filter (160–960 Hz) can attenuate most of the undesired low-frequency contents and reveal the seismic signal directly propagating from the source as shown in Figure 5b. The direct wave is presented as a hyperbola on at least 40 recording channels (approximately 80 m of the cable). Reflected waves are barely observable in the shot profile, even after filtering. However, they can be enhanced and observed after supergathering as we will discuss. Because the DAS receivers are trenched into the seafloor, the direct wave can be used to image the seafloor topography. The waves reflected from the subsurface below the seafloor are used to image subsurface geologic structures.

Seismic response of DAS in straight fiber

To demonstrate the seismic response of DAS to the direct P-wave, we analyze the source directivity and receiver response. We assume that our source size is much smaller than the wavelength, such that the far-field from a point source can be used. Due to spherical divergence, the amplitude of the seismic wave traveling from a point source to a receiver decreases linearly with the travel distance (r). Moreover, we consider the effect of the source ghost on the propagating wavefield. The directivity of a harmonic source and its ghost can be combined with the spherical divergence to describe the propagating strain field as follows:

$$\varepsilon_{rr} = \frac{1}{r}\left[2\sin\left(\frac{2\pi f z_s}{v}\cos\phi\right)\right]\varepsilon_{\text{source}}, \tag{15}$$

where $\varepsilon_{\text{source}}$ is the strain field of frequency f generated by the seismic source at the depth z_s, v is the wave velocity in the water, and ϕ is the angle between the wave propagating direction and the vertical axis as shown in Figure 6 (Drijkoningen, 2003). For the source depth $z_s = 0.60$ m and the velocity $v = 1490$ m/s, the directivity of the source with the ghost associated with the square bracket in equation 15 is illustrated in Figure 7.

The P-waves generate strains parallel to the direction of the wave propagation. Hence, the impinging seismic waves induce strains in the cable, which are also transported from the buffer layer to the fiber core. Suppose a planar P-wave propagates along the r-axis that forms the grazing angle θ with the straight cable along the x-axis as shown in Figure 6. The only nonzero strain component carried by the wave is ε_{rr}. Therefore, the projection of this strain component onto the cable axis is equal to

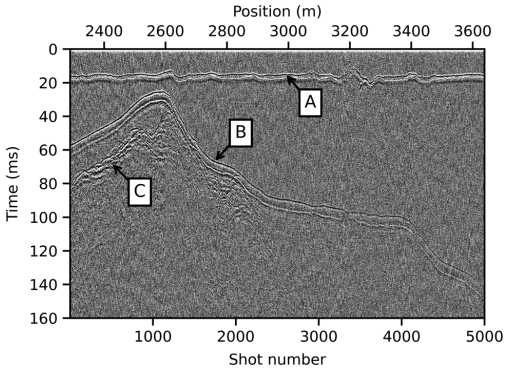

Figure 4. A common-channel seismic gather recorded by a towed single-channel streamer. It is also a common-offset gather at 10 m offset. Highlighted by the letters are the direct wave (A) and the reflections from the seafloor (B) and subsurface bedrock (C).

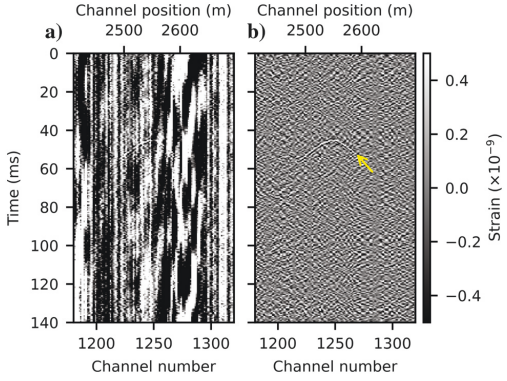

Figure 5. A shot profile (shot number 951 at 2546 m inline position) of multichannel DAS seismic records: (a) raw data and (b) data after applying a band-pass filter of 160–960 Hz for illustration. The yellow arrow indicates the direct wave from the source to the seabed receivers.

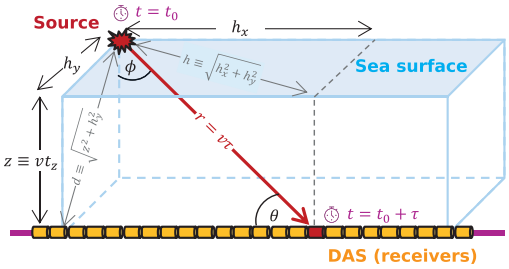

Figure 6. DAS recording system and its seismic source, where τ is the traveltime of direct wave propagation with velocity v from the source to a receiver at the inline offset h_x. At the receiver with zero inline offset ($h_x = 0$), the traveltime is shortest and equal to $\tau_{\{h_x=0\}} = d/v$, where d is the distance between the source and the DAS cable.

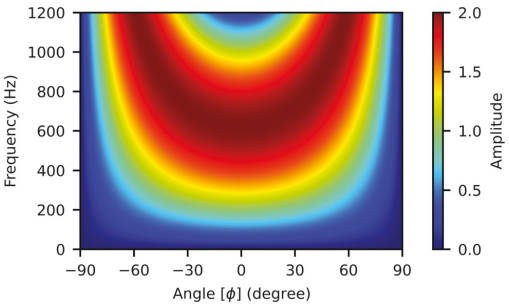

Figure 7. Amplitude directivity of a harmonic point source with ghost as a function of wave frequency and propagating angle from the vertical axis as defined in the square bracket in equation 15. The spherical divergence ($1/r$) is excluded in this plot. The source depth is 0.60 m below the sea surface, and the wave velocity is 1490 m/s.

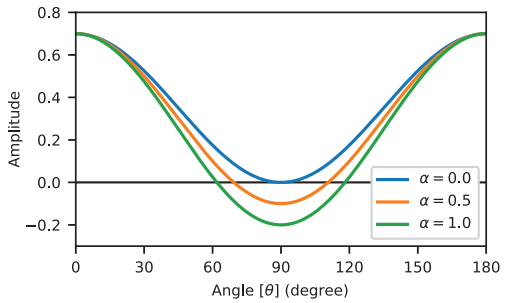

Figure 8. The optical point strain variation with the grazing angle of a plane wave impinging the DAS cable with different coupling coefficients (α) (see equation 20).

$$\varepsilon_{xx}^{(c)} = \varepsilon_{rr}\cos^2\theta. \tag{16}$$

However, the projection onto the normal axis to the cable is equal to

$$\varepsilon_{\perp}^{(c)} = \varepsilon_{rr}\sin^2\theta. \tag{17}$$

We now consider the anisotropic physical properties of a straight optical fiber embedded in a cable (elastic filler) as discussed by Kuvshinov (2016). Assuming that the fiber is perfectly coupled to the cable, the longitudinal deformation of the cable and fiber in response to longitudinal forces forms the isostrain loading condition. That is, the longitudinal strain ε_{xx} is transported from the cable to the fiber without losses:

$$\varepsilon_{xx}^{(f)} = \varepsilon_{xx}^{(c)}, \tag{18}$$

where the superscripts (f) and (c) denote the fiber and cable, respectively. In contrast, the forces perpendicular to the cable axis with perfect coupling form the isostress loading condition, that is, $\sigma_{\perp}^{(f)} = \sigma_{\perp}^{(c)}$. Hence, the transverse strain of the fiber is equal to the transverse strain of the cable multiplied by the ratio of the effective Young's modulus of the cable ($E^{(c)}$) to the effective Young's modulus of the fiber ($E^{(f)}$):

$$\varepsilon_{\perp}^{(f)} = \left(\frac{E^{(c)}}{E^{(f)}}\right)\varepsilon_{\perp}^{(c)} \equiv \alpha\varepsilon_{\perp}^{(c)}, \tag{19}$$

where α is referred to as the ratio $E^{(c)}/E^{(f)}$ implying the efficiency of the transverse strain transfer from a cable to the embedded fiber. The coupling coefficient α becomes one when the cable and fiber are made from the same material. However, the layered materials of the cable surrounding the fiber usually have a smaller effective Young's modulus than the fiber core.

Using equation 12 and the definitions of fiber strains discussed previously, we find that the relative change of an optical path in DAS varies with the grazing angle as

$$\frac{\Delta L_o}{L_o} \approx 0.7\varepsilon_{xx}^{(f)} - 0.2\varepsilon_{\perp}^{(f)} = (0.7\cos^2\theta - 0.2\alpha\sin^2\theta)\varepsilon_{rr}. \tag{20}$$

Figure 8 shows the responses of mapping the propagating strain field onto the optical path change as defined in the parentheses in equation 20 with different coupling coefficients (α). For nonzero coupling coefficients, this expression implies that the P-wave amplitudes become a small negative value (reverse polarity) when the grazing angle is near 90°. This agrees with the measurement done by Papp et al. (2017). It also supports our observation in Figure 5b that the amplitude of the direct P-wave does not fade toward the zero inline offset. Nevertheless, many studies assume that the effective Young's modulus of the cable materials is much smaller than the fiber ($\alpha \to 0$), so that the contribution of the transverse strain to the optical path change is negligible. Then, the optical path change is dominated by the $\cos^2\theta$ function (Mateeva et al., 2014; Kuvshinov, 2016). Therefore, they conclude that a P-wave arriving with an angle close to 90° will be poorly detected using DAS in a straight fiber.

The uses of the spatial moving average and the spatial phase change defined by gauge length form two field arrays for a recording channel of DAS. The recorded signal (A_{DAS}) is the average strain at each sensing element. The average strain at a DAS channel is related to the point strain, that is, the optical path change, through the combined array response:

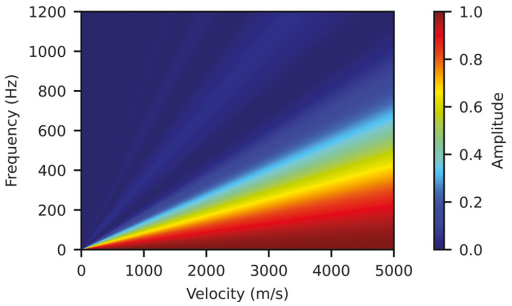

Figure 9. The variation of the DAS array response ($L_G = L_W = 4.08$ m) with the frequency and velocity of the wave propagating in the same direction as the fiber axis ($\theta = 0$).

$$A_{\mathrm{DAS}} = \left[\frac{\sin\left(\frac{k_x L_G}{2}\right)}{\frac{k_x L_G}{2}}\right]\left[\frac{\sin\left(\frac{k_x L_W}{2}\right)}{\frac{k_x L_W}{2}}\right]\left(\frac{\Delta L_o}{L_o}\right), \tag{21}$$

where k_x is the angular wavenumber along the fiber axis, L_G is the gauge length, and L_W is the pulse width (Bakulin et al., 2020). Given the grazing angle θ, we obtain $k_x = k\cos\theta = (2\pi f/v)\cos\theta$. Therefore, equation 21 can be rewritten as

$$A_{\mathrm{DAS}} = \left[\frac{\sin\left(\frac{\pi f L_G}{v}\cos\theta\right)}{\frac{\pi f L_G}{v}\cos\theta}\right]\left[\frac{\sin\left(\frac{\pi f L_W}{v}\cos\theta\right)}{\frac{\pi f L_W}{v}\cos\theta}\right]\left(\frac{\Delta L_o}{L_o}\right), \tag{22}$$

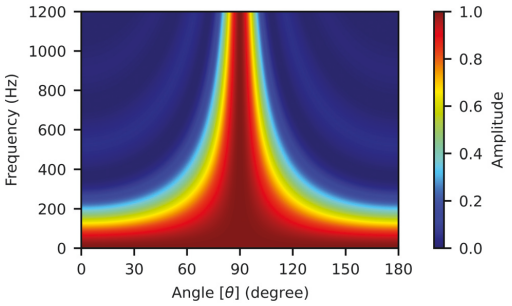

Figure 10. The variation of the DAS array response ($L_G = L_W = 4.08$ m) with the frequency and grazing angle of the wave in water, where $v = 1490$ m/s.

where f and v are the frequency and velocity of the wave, respectively. Figure 9 shows the variation of the DAS array response with the frequency and velocity of the wave propagating in the same direction as the fiber axis ($\theta = 0$). However, Figure 10 shows its variation with the frequency and grazing angle of the wave in the water, where $v = 1490$ m/s. In this experiment, we use $L_G = L_W = 4.08$ m. The combined response of the point strain response in equation 20 and the DAS array response in equation 22 is the product of the two responses. This product contributes to the total DAS receiver array response as illustrated in Figure 11.

Combining the response of the source and receiver arrays from equations 15, 20, and 22, we obtain the total directivity of the DAS system for a marine seismic survey as follows:

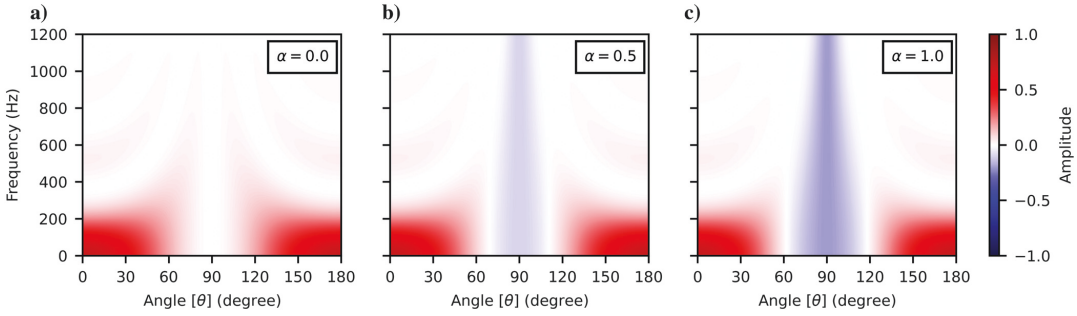

Figure 11. The total DAS receiver array response of the response to the strain field in Figure 8 and the DAS array response in Figure 10: (a) $\alpha = 0$, (b) $\alpha = 0.5$, and (c) $\alpha = 1$. Each plot is equivalent to the product of the point strain response with the associated coupling coefficient α in equation 20 and the DAS array response in equation 22.

$$A_{\mathrm{DAS}} \approx \left[\frac{\sin\left(\frac{\pi f L_G}{v}\cos\theta\right)}{\frac{\pi f L_G}{v}\cos\theta}\right]\left[\frac{\sin\left(\frac{\pi f L_W}{v}\cos\theta\right)}{\frac{\pi f L_W}{v}\cos\theta}\right] \times (0.7\cos^2\theta - 0.2\alpha\sin^2\theta) \times \frac{1}{r}\left[2\sin\left(\frac{2\pi f z_s}{v}\cos\phi\right)\right]\epsilon_{\mathrm{source}}. \quad (23)$$

We can further rearrange equation 23 to determine the DAS amplitude variation with the receiver depth z and the inline offset h_x at different crossline offsets h_y. Here, $d = \sqrt{z^2 + h_y^2}$, $r = \sqrt{h_x^2 + d^2}$, $h = \sqrt{h_x^2 + h_y^2}$, $\theta = \arctan(d/h_x)$, and $\phi = \arctan(h/z)$. For a wave frequency at 600 Hz and perfect coupling in the DAS cable ($\alpha = 1$), Figures 12 and 13 show different relative amplitude responses of DAS to the direct P-wave generated from a marine point source at 0.6 m depth, where the crossline offsets are 0 and 60 m, respectively. The amplitude responses at key water depths are also plotted at the bottom of each corresponding figure for clarity. For a wave with 600 Hz frequency and 1490 m/s velocity, we observe that the

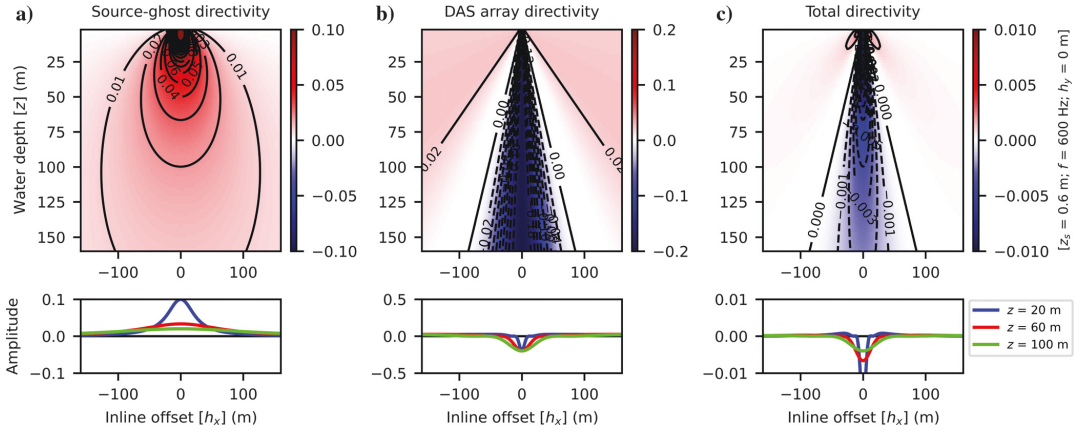

Figure 12. Responses of the DAS system in a straight fiber ($\alpha = 1$) to a spherical P-wave from a point source at 0 m crossline offset: (a) the array response of the source and its ghost with spherical divergence term applied, (b) the combined DAS array response to the strain field, and (c) the total response of the source and DAS arrays. The responses at key water depths are plotted at the bottom. The source is at 0.6 m depth and the wave propagates with 1490 m/s velocity at 600 Hz.

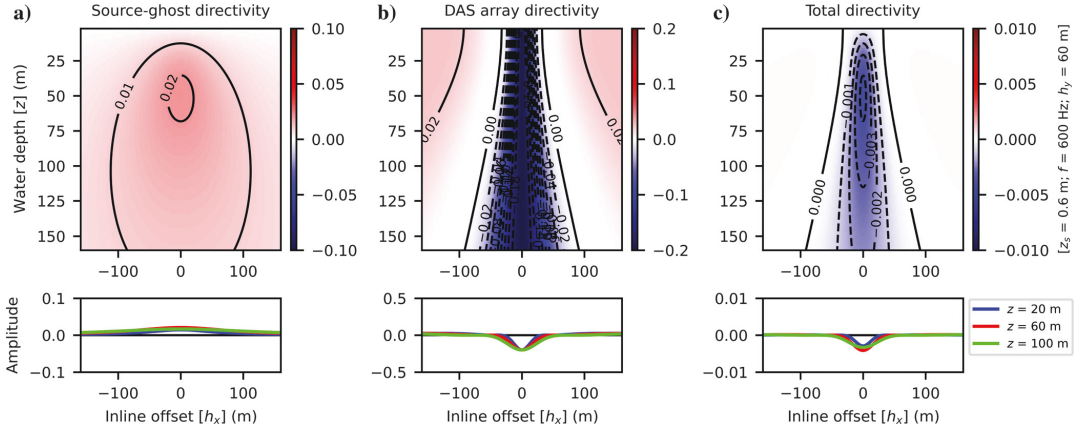

Figure 13. Responses of the DAS system in a straight fiber ($\alpha = 1$) to a spherical P-wave from a point source at 60 m crossline offset: (a) the array response of the source and its ghost with a spherical divergence term applied, (b) the combined DAS array response to the strain field, and (c) the total response of the source and DAS arrays. The responses at key water depths are plotted at the bottom. The source is at 0.6 m depth, and the wave propagates with 1490 m/s velocity at 600 Hz.

DAS receiver response negatively boosts the DAS amplitude at small inline offsets as shown in Figures 12b and 13b. However, it reduces the negative amplitude response at large inline offsets, in which the response is a positive side lobe. This variation is also observed in the total response of the combined source and DAS arrays in Figures 12c and 13c.

We now consider the DAS amplitude response corresponding to shot number 951 at the position of 2546 m as shown in Figure 5. At this position, the water depth is approximately 20 m and the cross-line offset is approximately 60 m. Figure 13c illustrates that the direct P-wave from this source position is presented at small inline offsets in the DAS data. The amplitude should fade toward the larger offsets until approximately a 40 m inline offset, at which the amplitude begins changing to the opposite polarity. At larger offsets, the amplitude continues in this reverse polarity and tends to increase gently with offsets.

Thanks to the reciprocity relation of the source and receiver, we can also observe this amplitude variation in a common-receiver gather from channel number 1251 at the position of 2555 m as plotted in Figure 14. Here, all of the seismic traces are associated with the same seabed condition at the receiver. Because the source signal is approximately identical for all of the shots, the amplitude variation of the direct wave in this receiver gather mainly depends on the propagation angle of the wave. In Figure 14b, we observe the polarity flips of the direct wave at the inline offsets of −47 and 56 m as marked by the green arrows. The inline offsets in which polarity flips occur are approximately 10 m larger than our estimate from Figure 13c. The discrepancy could result from the uncertainty of the source depth, wave frequency, velocity, and coupling coefficient parameters used in our calculation. The actual source depth depends on the sea state, whereas the actual wave is a multifrequency wave pulse. Moreover, the actual P-wave velocity of the media around the fiber may be higher than the velocity in the water used in our calculation. It is also difficult to determine a precise critical offset from the real data, because this is the point at which various types of waves including reflection, refraction, direct wave, and surface wave are juxtaposed. Because the amplitude of the direct P-wave in DAS is very small at this point, all of the other waves become dominant. Despite some deviations, our observations are generally described by equation 23.

Note that the amplitude response based on equation 23 depends on several factors including the dominant frequency of the signal being recorded and the physical properties of the telecommunication cable. This equation gives a possible explanation for the amplitude characteristics observed in our DAS data generated from a high-frequency seismic source. It is beyond the scope of this article to precisely determine the parameters, especially the coupling coefficient α, contributing to the amplitude response. For the further analysis in this article, we focus on the methods to produce subsurface images, for which the coupling between impinging seismic waves and the DAS recorded signals is irrelevant.

METHODS

As a key reference, the seismic image of the seafloor and the subsurface from the single-channel streamer data is obtained through the following processes:

1) Apply a static time shift to redatum the source and receiver to the sea surface.
2) Apply normal moveout (NMO) correction to correct the traveltime from arbitrary offsets to zero offset, in which the source and receiver are virtually at the same position. To be compared with the DAS data set, the NMO velocity from DAS data processing is used.
3) Mute the undesired direct wave.
4) Apply zero-offset time migration using the NMO velocity.

We also resample the streamer seismic data from 0.25 to 0.44 ms to match the time-sampling interval of the DAS data.

Calibration of DAS seismic data

In contrast to streamer data, DAS data are continuously recorded along the cable with many more recording channels. To extract a shot profile from this continuously recorded data, we need to know the precise gun firing time of the source. However, it is our limitation that synchronous sampling of the DAS and streamer recording systems was not used in our experiment. Therefore, we use the Coordinated Universal Time (UTC) time stamps of the gun firing from the recorded streamer data to tailor the continuously recorded DAS data into several shot profiles. Unfortunately, the streamer data are recorded in SEG-Y format, in which the time stamps are stored at the accuracy of 1 s only. In contrast, the recording time interval of the DAS data is 0.44 ms. Therefore, uncertainty exists in defining the exact time sample in the DAS data when the gun is fired from the given time stamp with lower precision. To overcome this challenge, we propose a data-driven method to estimate the start time of each shot record from the corresponding first-arrival time in our DAS data.

Assuming that the DAS receivers are on the seafloor, the first-arrival event at near offsets is the direct wave propagating from the source to DAS receivers as shown in Figure 6. Given time picks of the first arrival at the inline offset of $h_x = 0$ and any h_x, we can estimate the source-to-cable distance (d) and, then, the start UTC time of a DAS shot record (t_0) using the following expressions (see Appendix A for derivation):

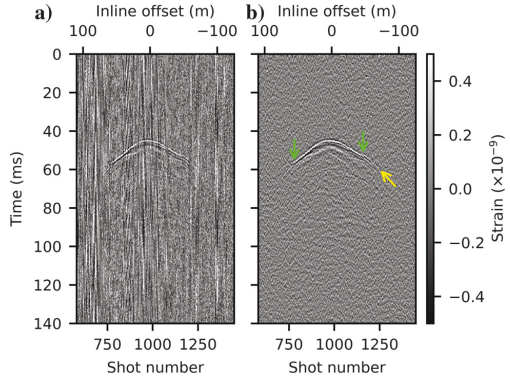

Figure 14. A common-receiver gather (channel number 1251 at the 2555 m inline position) of DAS seismic records: (a) raw data and (b) data after applying a band-pass filter of 160–960 Hz for illustration. The direct P-wave from consecutive shots to the receiver on the seafloor is indicated by the yellow arrow. Polarity flips of the direct arrival are highlighted by the green arrows.

$$d = \frac{v}{2\Delta\tau}\left(\frac{h_x^2}{v^2} - (\Delta\tau)^2\right) \tag{24}$$

and

$$t_0 = t_{\{h_x=0\}} - \tau_{\{h_x=0\}} = t_{\{h_x=0\}} - \frac{d}{v}, \tag{25}$$

where v is the P-wave velocity in the seawater, t is the picked UTC time at which the direct wave arrives at a receiver on the DAS cable, τ is the traveltime for the wave that propagates directly from the source to a receiver, and $\Delta\tau$ is the difference between τ at $h_x = 0$ and τ at any h_x. That is, $\Delta\tau = \tau_{\{h_x\}} - \tau_{\{h_x=0\}}$, where $\tau_{\{h_x=0\}} = d/v$ by definition. In this study, we assume the velocity in water to be constant at 1490 m/s. Using these expressions, we can derive the start UTC time of every shot and construct individual shot profiles of DAS.

It should be noted that equation 24 can determine the distance (d) between the source and DAS cable, even if no information of the source position is given. Consequently, equation 25 requires no source parameter to determine the gun firing time. Using this method, we find that the actual gun firing time interval is slightly shorter than the value we set to the shooting box. Moreover, given the water depth (z) of a receiver, we can estimate the crossline offset (h_y) using the expression:

$$h_y = \sqrt{d^2 - z^2}. \tag{26}$$

Therefore, with sufficient constraints from the recording geometry, it is possible to derive the positions and time of sources from DAS data by analyzing the traveltime of the direct wave. Then, we may use the signals from unknown sources for subsurface imaging, which should be studied further. Nevertheless, this article will focus on the DAS application using controlled seismic sources. Even if there are no time synchronization issues in the survey, our proposed method can still be used to calibrate the positions and times of the seismic sources.

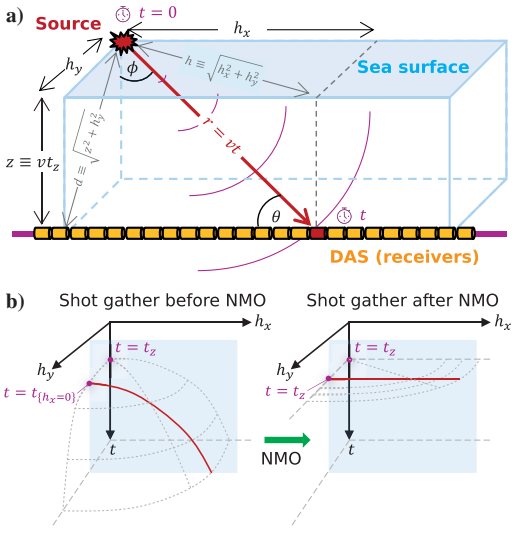

Figure 15. Description of NMO correction for the one-way traveltime of the direct wave in the DAS recording system: (a) the geometry of the direct wave and (b) the schematic plot of the direct wave in a shot gather before and after NMO correction. The NMO-corrected traveltime of the direct wave is equal to the one-way traveltime along the vertical axis to the seafloor.

DAS seismic processing

Given shot profiles recorded by DAS, we do preconditioning steps to enhance the S/N of the data followed by imaging steps. Because the receivers are located at the seafloor, the seismic images of the seafloor and its underlying subsurface structures are generated from different seismic events. The seafloor image, that is, the water depth topography, can be derived from the direct wave from the source to the receivers on the seafloor. However, the structural image below the seafloor can be derived from the corresponding seismic reflections. Hence, we require two different imaging methods to generate the complete subsurface image comprising seafloor topography and its underlying structures. The processing sequence for DAS data is summarized in Appendix B.

NMO correction for the direct wave

The direct wave from the source to the DAS receivers on the seafloor is illustrated in Figure 15. The NMO traveltime correction ($\Delta t_{\mathrm{NMO,direct}}$) is to map the traveltime (t_{direct}) of the direct wave event to t_z, which is the one-way traveltime for the vertical propagation distance of z. The NMO correction for the direct wave is

$$\Delta t_{\mathrm{NMO,direct}} \equiv t_{\mathrm{direct}} - t_z = \sqrt{t_z^2 + \frac{h^2}{v^2}} - t_z, \tag{27}$$

where $t_{\mathrm{direct}} = \sqrt{t_z^2 + (h^2/v^2)}$, $h \equiv \sqrt{h_x^2 + h_y^2}$, $h_y = \sqrt{d^2 - z^2}$, and z is the known water depth for the central receiver ($h_x = 0$). Thus, the correction will produce the one-way traveltime zero-offset seismic gather where the source is virtually right above the central receiver. Multiplying the time axis by two will convert the gather into two-way traveltime to be comparable with the seismic reflection data from the streamer.

In practice, we redatum the source and receivers to be at the sea surface prior to NMO correction to output the two-way traveltime seismic image. That is, the receiver static correction of t_z is added to the traveltime of the wavepath in Figure 15a. Then, the traveltime of the shot profile after redatuming to the sea surface is defined as

$$T_{\mathrm{direct}} \equiv t_{\mathrm{direct}} + t_z, \tag{28}$$

where t_{direct} is the one-way traveltime of the direct wave from the source to a receiver. Here, the NMO correction is to map the redatumed traveltime T_{direct} into the two-way traveltime for the vertical propagation distance from the source to the seafloor, i.e.,

$$T_z = 2t_z. \tag{29}$$

Hence, the NMO correction for the direct wave after redatuming to the sea surface is

$$\Delta T_{\mathrm{NMO,direct}} \equiv T_{\mathrm{direct}} - T_z = t_{\mathrm{direct}} - t_z = \Delta t_{\mathrm{NMO,direct}}. \tag{30}$$

Using equations 27 and 29, we can explicitly derive the NMO correction for redatumed traveltime of the direct wave in equation 30 as follows:

$$\Delta T_{\mathrm{NMO,direct}} = T_{\mathrm{direct}} - T_z = \sqrt{\frac{T_z^2}{4} + \frac{h^2}{v^2}} - \frac{T_z}{2}. \tag{31}$$

NMO correction for the reflected wave

After redatuming source and receivers to the sea surface, we can apply a conventional NMO correction to the reflected wave. The NMO correction for the two-way traveltime of the reflected wave can be written as follows:

$$\Delta T_{\mathrm{NMO,reflected}} = T_{\mathrm{reflected}} - T_z = \sqrt{T_z^2 + \frac{h^2}{v_{\mathrm{rms}}^2}} - T_z, \tag{32}$$

where $T_{\mathrm{reflected}}$ is the two-way traveltime of the reflected wave to the virtual receiver at the sea surface, T_z is the two-way traveltime for the vertical propagation distance from the source to the reflector, and v_{rms} is the root-mean-square (rms) velocity from the sea surface to the reflector. Velocity analysis is required to estimate proper velocities for different reflectors.

When the NMO correction for the direct wave using equation 31 is applied, the direct wave becomes flat in the common-shot gather; however, all of the subsurface reflections below the seafloor are overcorrected. On the other hand, the reflections will become flat if the NMO correction for the reflected wave in equation 32 is applied using the proper velocity. However, the direct wave would then be undercorrected.

NMO stretch

NMO correction causes an inevitable frequency distortion, namely, NMO stretching, especially for shallow events and at large offsets. As a result of stretching, seismic events are shifted to lower frequencies. The wavelet with a dominant period τ is stretched such that its period after NMO correction becomes τ_{NMO}, which is greater than τ. That is,

$$\tau_{\mathrm{NMO}} = \tau + \Delta\tau_{\mathrm{NMO}}. \tag{33}$$

Stretching is quantified by the change in the period of the wavelet divided by the initial dominant period, that is, $\Delta\tau_{\mathrm{NMO}}/\tau$. Hence, stretching for direct wave NMO correction for $\tau \ll T_z$ is quantified by

$$\frac{\Delta\tau_{\mathrm{NMO,direct}}}{\tau} \approx \frac{\Delta T_{\mathrm{NMO,direct}}}{T_z + \Delta T_{\mathrm{NMO,direct}}}, \tag{34}$$

where T_z is the two-way traveltime for the vertical propagation distance from the source to the seafloor and $\Delta T_{\mathrm{NMO,direct}}$ is given by equation 31. This equation implies that the NMO stretch can be increased by the decrease of the water depth and the increase of offset. The derivation of equation 34 is given in Appendix C.

However, stretching for reflected-wave NMO correction for $\tau \ll T_z$ is quantified by

$$\frac{\Delta\tau_{\mathrm{NMO,reflected}}}{\tau} \approx \frac{\Delta T_{\mathrm{NMO,reflected}}}{T_z}, \tag{35}$$

where T_z is two-way traveltime for the vertical propagation distance from the source to the reflector and $\Delta T_{\mathrm{NMO,reflected}}$ is given by equation 32. This expression is the same as NMO stretch for two-way traveltime reflections for any surface source and surface receiver (Yilmaz, 2001).

Temporal resolution

We now analyze a combined effect of the two DAS arrays associated with pulse width L_W and gauge length L_G on the temporal resolution of a plane wave propagating with velocity v and the grazing angle θ to the fiber axis. The effective fiber length of the combined array is the summation of the length of the two arrays, that is, $L_{\mathrm{effective}} = L_W + L_G$. Then, the arrival time of a plane wave at the two ends of this effective array is different by $\Delta\tau_{\mathrm{DAS}} = (L_{\mathrm{effective}} \cos\theta)/v$. A plane wave with a dominant period τ is transformed by DAS arrays to be extended along the time axis by this time delay. Hence, the ratio of the time delay to the dominant period of the wave is determined by

$$\frac{\Delta\tau_{\mathrm{DAS}}}{\tau} = \frac{f(L_G + L_W)}{v}\cos\theta, \tag{36}$$

where $f = 1/\tau$ is the dominant frequency of the wave and $\cos\theta = h_x/\sqrt{z^2 + h_x^2 + h_y^2}$. The ratio of the time delay to the wave period given by this equation may be interpreted as the stretching due to the DAS response, because it is similar to the definition of NMO stretching. DAS stretching vanishes at the zero inline offset, in which the wave propagates in the direction perpendicular to the fiber axis. Therefore, DAS stretching can be neglected for the data at nearly zero inline offset, whereas NMO stretching dominates the temporal resolution of the final images.

Image quality

The quality of an image can be evaluated by its S/N. Hence, we use the S/N to quantitatively compare the quality of the DAS and streamer images. In our analysis, S/N of the ith trace is defined as the ratio of the power of the signal ($P_{\mathrm{signal},i}$) within the trace to the average background noise power (P_{noise}) of the whole survey:

$$(\mathrm{S/N})_i = \frac{P_{\mathrm{signal},i}}{P_{\mathrm{noise}}} = \left(\frac{A_{\mathrm{signal},i}}{A_{\mathrm{noise}}}\right)^2, \tag{37}$$

where $A_{\mathrm{signal},i}$ is the rms amplitude of the samples within the signal window from the ith trace and A_{noise} is the rms amplitude of the samples within the background noise window from all of the traces. The ratio can be expressed in decibels (dB) as

$$(\mathrm{S/N})_{\mathrm{dB}} = 10\log_{10}(\mathrm{S/N}). \tag{38}$$

RESULTS AND DISCUSSION

The key seismic imaging from DAS data begins with NMO corrections. Figure 16 illustrates the results of NMO corrections for the direct wave and reflected waves in a super shot gather of the real data. The figure illustrates a supergather at shot number 2161, which is approximately at 2877 m distance on the cable, which is aligned with the horizontal axis in Figure 17. An offset trace in a supergather is derived by summing the seismic traces from nearby shots at the same offset bin. Supergathering can significantly enhance the S/N. However, it typically causes lower temporal resolution, because it stacks the waves with inconsistent phases. This supergathering technique is also applied to enhance the key seismic events for velocity analysis. The NMO corrections for the direct wave and reflected waves are carried out independently after noise attenuation, redatuming to the sea surface, and data regularization. The velocity models used in the NMO corrections are obtained by time-velocity scanning semblance analysis, in which the velocity in water is assumed to be 1490 m/s. Note that the minimum offset in this shot gather is approximately 30 m. Hence, the first arrivals in all of the existing traces in this gather are reflected waves, not the direct wave.

After NMO corrections are applied, we mute the data with severe NMO stretch at a far offset and stack all the traces below the mute function. Then, two stacked sections are derived, that is, one from direct wave and the other from reflected waves. After stacking the NMO-corrected gathers of DAS data, we combine the two stacked sections by summing the traces from the same shot. Then, we broaden the amplitude spectrum to be comparable with the reference seismic data from the streamer. We finally apply zero-offset time migration to the stacked data and compare the result with the image from streamer data in Figure 17. Figure 17a and 17b shows the migrated images from the streamer and DAS, respectively. The DAS image contains stronger high-frequency noise than the streamer image. The dominant frequency of the DAS image is also somewhat lower and the bandwidth is narrower than the streamer image.

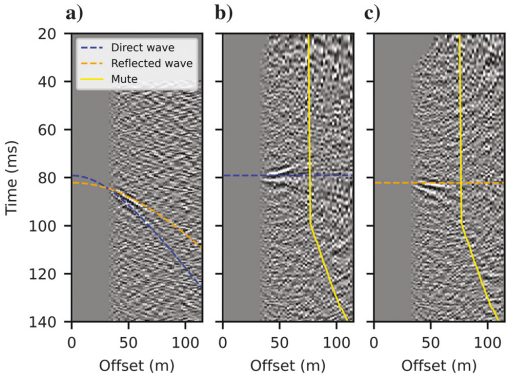

Figure 16. NMO corrections for the real DAS data set after redatuming to the sea surface and regularization. Supergathering the data from 21 shots around the shot number 2161, of which the position is approximately at 2877 m on the cable, is made to enhance the S/N for illustration: (a) a supershot gather sorted by regularized absolute horizontal offsets from the source to the DAS receivers. (b) The result of NMO correction for the direct wave. (c) The result of NMO correction for the reflected wave. The dashed blue line is the direct wave event and the dashed orange line is a key reflection event, which are estimated by the associated time-velocity picks. The solid yellow line is the external mute function to be applied before stacking the data along the offset.

We observe that the DAS image below the seafloor is contaminated by high-frequency noise, whereas the streamer image is somewhat cleaner. Therefore, we apply additional signal enhancement processing to the image by trace mixing of the surrounding 21 traces and applying a high-cut filter at 480 Hz. These additional steps are applied to the streamer and DAS images, and the results are shown in Figure 17c and 17d, respectively. After signal enhancement, the continuity of the seafloor images is improved, and the subsurface reflections in the images become obvious and easy to interpret. Key seismic reflections can be observed in both images as highlighted by the yellow arrows in the figures. However, the signal enhancement reduces the frequency bandwidth and, hence, the image resolution. Therefore, the trade-off between enhancing the signal and maintaining the frequency bandwidth should be carefully tested to optimize the DAS image quality.

The geologic image from streamer data results from seismic reflections, whereas the direct wave does not penetrate through any structure below the seafloor. However, the DAS seismic imaging uses the direct wave and reflections to construct the geologic image. Figure 17d illustrates that the seafloor and the underlying subsurface structures can be imaged from DAS seismic data by our processing sequence. The seafloor and subsurface image from DAS data is comparable to the reference image from streamer data in Figure 17c. Note that the DAS image represents the image at a different position from the streamer data, because their receiver positions are different. Therefore, the subsurface structures in the images from the streamer and DAS are slightly different.

We observe that the DAS image has low resolution in the shallowest part of the line between 2500 and 2700 m, in which the crossline offset is larger than the water depth. The primary reason is that our DAS data lack near-offset information, whereas the water depth is shallow at these locations. Therefore, the effect of NMO stretch becomes significant and causes a low dominant frequency content in the NMO result, especially for the water bottom event. Note that NMO stretch for the water bottom event depends on the water depth and offset according to equation 34. The stretch increases with the decrease of the water depth and the increase of the offset. Figure 18a illustrates the variations of water depth and minimum offset at different receiver positions. The minimum offset is the crossline offset (h_y) as illustrated in Figure 6. The source-to-cable distance (d) is also plotted in Figure 18a. In addition, Figure 18b shows the minimum stretch associated with the water bottom event. The minimum offset for the towed streamer is assumed to be 10 m throughout the survey. We observe that the minimum NMO stretch for DAS data is significantly larger than the minimum stretch for towed-streamer data. Thus, the water-bottom image from DAS has lower resolution than the image from the towed streamer as shown in Figure 17. The resolution of the DAS image is extremely low in the shallow water area at 2500–2600 m along the cable. To obtain a higher resolution image, we should have controlled the seismic source to be laterally closer to the DAS cable. That is, we must reduce the crossline offset between the source and the DAS cable during the survey, so that the NMO stretch is minimized. Then, a higher resolution seismic image

can be achieved. The requirement of a short crossline offset is crucial especially for any shallow-water environment.

The effect of NMO stretch is illustrated in Figure 19, which compares a near-trace gather of the DAS data before and after NMO correction for the direct wave. Each trace of the near-trace gather is formed by stacking those seismic traces with inline offsets less than 2 m from the corresponding shot gather. The gather represents the DAS data with a nearly zero inline offset. That is, the offset of each trace in the gather is approximately equal to the crossline offset. In Figure 19a, we observe coherent seismic events (the direct wave) before NMO correction that would contribute to the seafloor image. These events have temporal resolution comparable to the streamer data as shown in Figure 4. The key coherent seismic events are indicated by the black arrows in Figure 19. When the NMO correction for the direct wave is applied, the events are shifted in time and their characteristics are deformed by NMO stretch. NMO stretch deforms the wavelet to have a lower frequency than the original form. As shown in Figure 19b, the stretch is enormous especially in the shallow water depth and large crossline offset such as in event A. In contrast, we see less NMO stretch where the crossline offset is short and the water is deep such as in event B. This observation is aligned with the plot of minimum stretch in Figure 18b.

Figure 20a compares the S/Ns in dB of the images from DAS and towed streamer around the water bottom. As plotted in Figure 17, the signal window is defined between the orange and green horizons, whereas the noise window is defined between the blue and orange horizons. We observe that the images from the towed-streamer data generally have a higher S/N than the DAS images, especially when the seafloor is shallow. However, Figure 20b compares the normalized power spectrum of the images in the signal window from streamer and DAS after the same postmigration signal enhancement processing. We observe that the DAS image has a lower dominant frequency than the streamer image. Moreover, the DAS image has more low-frequency content than the streamer image.

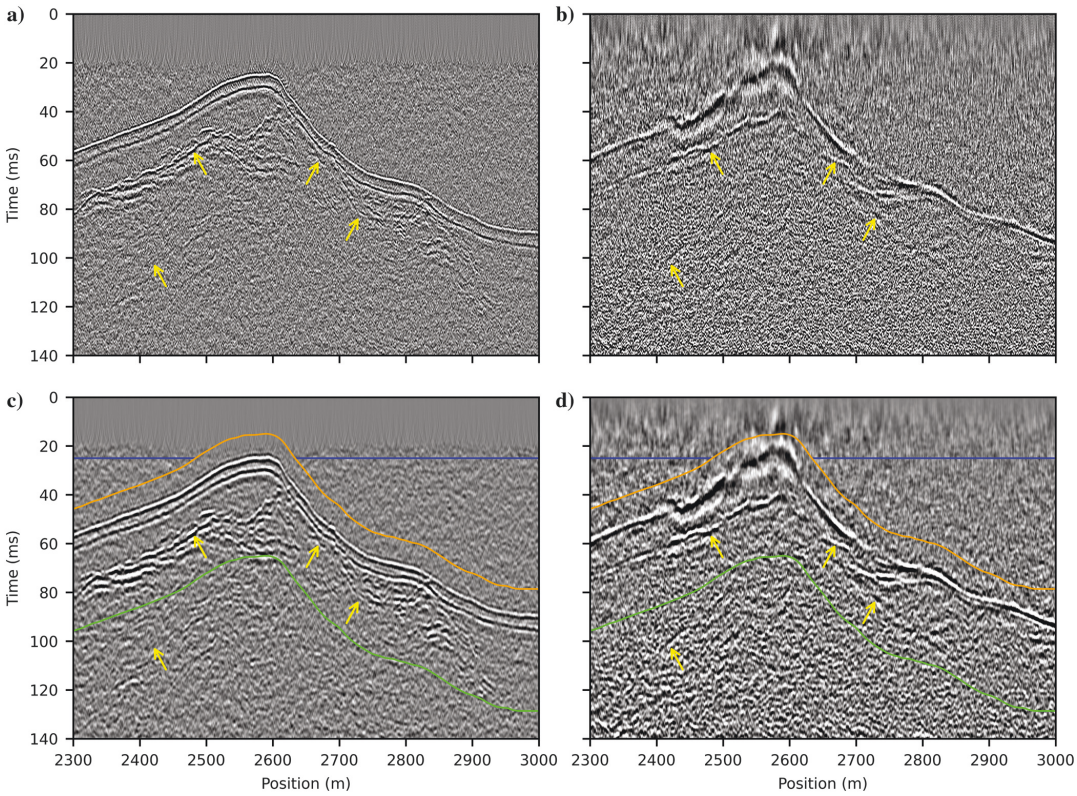

Figure 17. Poststack time-migrated seismic images from different data sets: (a) the reference image from a towed single-channel streamer with a 24-element hydrophone array of 7 m active length, (b) the image from seabed DAS with a 4 m gauge length, (c) the image of (a) with additional signal enhancement applied, and (d) the image of (b) with the same enhancement applied. The seismic events associated with the water bottom and subsurface reflections are presented in both images. Subsurface reflections in the DAS image are highlighted by yellow arrows in comparison with the reference image. The horizontal axis is the distance along the cable. The horizons plotted in (c and d) define the signal and noise windows for computing the S/N and spectrum in Figure 20. The signal window is defined between the orange and green horizons, whereas the noise window is defined between the blue and orange horizons.

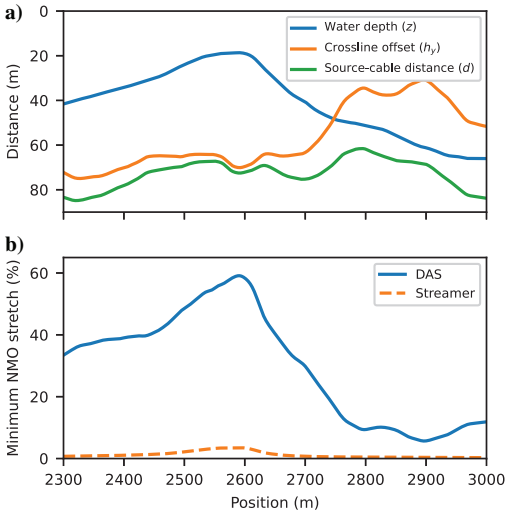

Figure 18. Plots of the following variables at different positions along the DAS cable: (a) the water depth (blue), the crossline horizontal offset from the source to the DAS cable (orange), and the distance between the source and the DAS cable (green); and, (b) the minimum NMO stretch associated with the water-bottom events in DAS data (the solid blue line) and towed-streamer data (the dashed orange line).

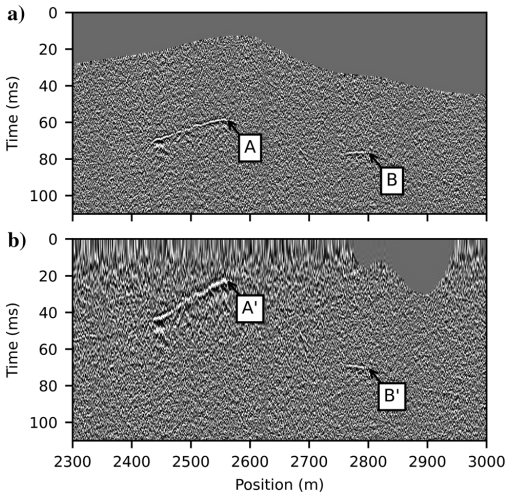

Figure 19. Illustration of the NMO stretch effect on a near-trace gather of DAS data in which the sources and receivers are redatumed to the sea surface: (a) a near-trace gather from the DAS data with common inline offset and (b) the same gather after NMO correction for the direct wave is applied. The black arrows indicate the two events before and after NMO correction as described in the text.

Limitations of the study

We emphasize that our comparison is not one to one in the sense that the streamer data result from the summation of the 24 hydrophone elements (approximately 7 m) into a single channel. Stacking of 24 hydrophone elements corresponds to an improved S/N of the square root of the number of stacking elements (nearly five times in this case). This is the major explanation for why the raw streamer data have less noise compared to the raw DAS data. The DAS data are recorded from each sensing element with a gauge length of 4 m. Furthermore, under an angle mute function, we sum the recorded data from at least 40 channels of 2 m spacing (approximately 80 m) with obvious signals as observed in Figure 5 to form a single trace of the DAS image in Figure 17b and 17d. The multichannel summation of the DAS data significantly enhances the S/N. However, the optimal number of channels to be summed is still limited by the desired temporal resolution associated with the offset-dependent NMO stretch. Therefore, we recommend testing the mute function for stacking to find a compromise between the signal enhancement and the temporal resolution.

Our seismic analysis covers the range from 160 to 480 Hz, corresponding to the wavelengths in the range of 9.4–3.1 m with the velocity of 1490 m/s. However, the bandwidth of the seismic source used in this experiment ranges from 350 to 1000 Hz with the dominant frequency at approximately 600 Hz. For wave velocities on the order of 1490 m/s, this corresponds to wavelengths in the range of 4.3–1.5 m, with the dominant energy at a wavelength of 2.5 m. Thus, with a DAS interrogator operating with a 4 m gauge length, the seismic waves propagating in parallel to the cable with frequency greater than the 375 Hz notch cannot be properly resolved

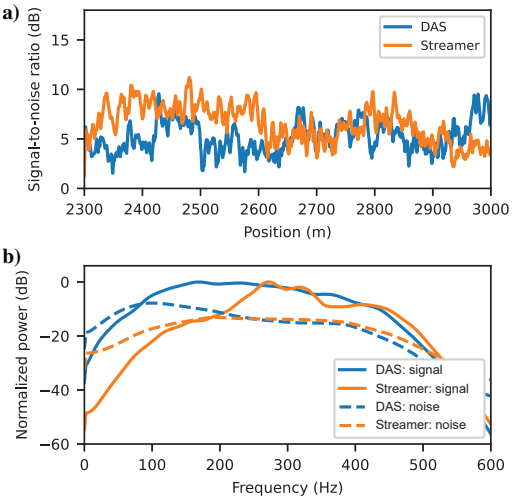

Figure 20. Line plots corresponding to the seismic images from DAS (blue) and towed streamer (orange) with additional signal enhancement applied as shown in Figure 17c and 17d: (a) S/N at different seismic traces and (b) normalized amplitude spectra within the signal and noise windows. The signal window is defined between the orange and green horizons, whereas the noise window is defined between the blue and orange horizons in Figure 17.

by DAS (see Figures 9 and 10 for the DAS array response). Using a seismic source with stronger low-frequency emission or operating the DAS interrogator at shorter gauge lengths should, therefore, improve the DAS image resolution. Furthermore, with a more powerful source at low frequencies, it might be possible to use more DAS channels at larger inline offsets (a longer cable length) to construct a larger aperture that might improve the spatial resolution and provide deeper imaging capabilities with DAS. Note that the seismic source used in our experiment is relatively weak compared to conventional seismic sources such as air guns.

Our major objective of this article is to achieve a qualitative comparison of the two types of data to demonstrate the enormous potential for DAS data, despite its higher background noise level. The tremendous advantage for the DAS data is the number of channels in the long fiber-optic cable. We aim to indicate that it is possible for DAS to record data over a long distance (several kilometers) to form subsurface images with comparable quality to those formed with the conventional streamer. The advantage of having excessive receivers over a long distance can be exploited for several other applications, such as tracking the positions of marine vessels, marine mammals, earthquakes, and so on. However, this article is limited to a simple comparison of conventional seismic imaging to DAS imaging for seismic exploration based on different acquisition geometries.

The results shown in this article clearly prove that we can use DAS cables together with controlled seismic sources to construct a subsurface image comparable to a conventional seismic survey using towed streamers. To obtain a DAS image with high quality and high S/N, we require sufficient source energy within the frequency range limited by the gauge length, which implies the spatial resolution of DAS. Moreover, we have to minimize the crossline offset between the source and the DAS cable during the survey to prevent excessive stretch and improve the image resolution. Thus, we can conclude that it is possible to use DAS from existing dark fiber-optic cables together with appropriate seismic sources for subsurface imaging. If a conventional seismic survey is conducted above recording DAS cables, the near-surface seismic image from DAS can be obtained and can be used for geohazard analysis prior to any construction on the seafloor. Hence, we envisage many possibilities of DAS to support various subsurface exploration activities.

CONCLUSION

We can produce subsurface images from seismic data acquired by DAS in a submarine telecommunication cable. The quality of the images can be improved by using a seismic source with sufficiently large energy within the low-frequency range matching the spatial resolution of DAS. A low-frequency seismic source would also improve the penetration to deeper geologic structures, and, hence, deeper seismic images. The temporal resolution can be improved by minimizing the crossline offset between seismic sources and the DAS cable. For water depths larger than the offset range used for DAS imaging, we find that DAS and hydrophone data have about the same quality. The DAS recording can be carried out simultaneously with any conventional seismic survey to support geohazard analysis below the seafloor and various subsurface exploration activities. The operational advantages of DAS over node systems and the validity of DAS for near-surface seismic imaging will sustain the growth of DAS in the seabed seismic market.

ACKNOWLEDGMENTS

The authors acknowledge the Norwegian Research Council, and the sponsors of the Geophysics and Applied Mathematics in Exploration and Safe production Project (grant no. 294404), the Digimon ACT Project (grant no. 299622), and the Centre for Geophysical Forecasting (grant no. 309960) at NTNU for financial support. The authors also thank the crew onboard the R/V *Gunnerus* for assistance during the field work, Alcatel Submarine Networks for lending an OptoDAS interrogator, Shearwater GeoServices Software for the Reveal software used in our analysis, Trond Larsen and KystTele for access to the optical fiber, and Eirik Larssen for assistance in facilitating the DAS experiment.

DATA AND MATERIALS AVAILABILITY

Data associated with this research are confidential and cannot be released.

APPENDIX A

DISTANCE BETWEEN SOURCE AND CABLE

From Figure 6, we define that t_0 is the UTC time when the source is fired, t is the UTC time when the direct wave arrives at a receiver, and τ is its traveltime from the source to the receiver. Thus,

$$\tau = t - t_0. \tag{A-1}$$

Assuming the constant velocity v, we can compute the travel distance of the direct wave from source to the receiver with the inline offset h_x as follows:

$$v\tau = \sqrt{d^2 + h_x^2}, \tag{A-2}$$

where d is the distance between the source and the DAS cable. Hence, the traveltime of the direct wave can be written as a function of the inline offset h_x as follows:

$$\tau_{\{h_x\}} = \frac{1}{v}\sqrt{d^2 + h_x^2}. \tag{A-3}$$

The subscript on variable τ denotes its functional dependence on the inline offset h_x. To the receiver at zero inline offset ($h_x = 0$), the traveltime has a minimum at

$$\tau_{\{h_x=0\}} = \frac{d}{v}. \tag{A-4}$$

Hence, the difference between the traveltime at zero inline offset and the traveltime at an arbitrary offset is defined as follows:

$$\Delta\tau = \tau_{\{h_x\}} - \tau_{\{h_x=0\}} = \frac{1}{v}\sqrt{d^2 + h_x^2} - \frac{d}{v}. \tag{A-5}$$

Rearranging equation A-5, we obtain equation 24 via the following steps:

$$\Delta\tau + \frac{d}{v} = \frac{1}{v}\sqrt{d^2 + h_x^2}, \tag{A-6}$$

$$\left(\Delta\tau + \frac{d}{v}\right)^2 = \frac{1}{v^2}(d^2 + h_x^2), \tag{A-7}$$

$$(\Delta\tau)^2 + 2(\Delta\tau)\left(\frac{d}{v}\right) + \frac{d^2}{v^2} = \frac{d^2}{v^2} + \frac{h_x^2}{v^2}, \tag{A-8}$$

$$d = \frac{v}{2\Delta\tau}\left(\frac{h_x^2}{v^2} - (\Delta\tau)^2\right). \tag{A-9}$$

APPENDIX B

DAS DATA PROCESSING SEQUENCE

The processing sequence for DAS data is listed here:

1) Perform radial trace mixing by summing the seismic traces from neighboring shots (3:1 shots).
2) Apply a band-pass frequency filter for 160 Hz/20 dB – 960 Hz/20 dB.
3) Apply static correction to redatum the source and receivers to the sea surface.
4) Regularize data using offset bin spacing of 1 m.
5) Apply NMO correction to correct the traveltime from arbitrary offsets to zero offset for the following two events separately using different correction methods:
   - the direct arrival from the source to the DAS receivers on the seafloor
   - the primary reflections from the geologic structures underlying the seafloor.
6) Attenuate multiple reflections in the Radon domain.
7) Mute the undesired NMO stretch at far offsets (0°–30° with 76 m preserved minimum offset).
8) Stack the NMO data from all offset bins.
9) Combine the NMO stacks from the direct arrival and reflections to construct a zero-offset seismic reflection data set in which the source and receivers are virtually at the sea surface.
10) Apply spectral whitening.
11) Apply zero-offset time migration using the NMO velocity for primary reflections.
12) Perform radial trace mixing by summing the seismic traces from the surrounding 21 traces.
13) Apply a high-cut filter at 480 Hz/20 dB.

APPENDIX C

MOVEOUT STRETCH FOR THE DIRECT WAVE

Considering the DAS data after redatuming the source and receivers to the sea surface, the direct wave moveout equation associated with the onset of the wavelet with the arrival time T_{direct} at offset h is given by equation 31. This expression can be rearranged as follows:

$$\left(T_{\text{direct}} - \frac{T_z}{2}\right)^2 = \frac{T_z^2}{4} + \frac{h^2}{v^2}, \tag{C-1}$$

$$T_{\text{direct}}^2 - T_{\text{direct}}T_z + \frac{T_z^2}{4} = \frac{T_z^2}{4} + \frac{h^2}{v^2}, \tag{C-2}$$

$$T_{\text{direct}}^2 - T_{\text{direct}}T_z = \frac{h^2}{v^2}. \tag{C-3}$$

After applying NMO correction for the direct wave, the wavelet of dominant period τ is stretched, and then its dominant period becomes $\tau_{\text{NMO}} = \tau + \Delta\tau_{\text{NMO,direct}}$ as previously defined in equation 33. Thus, the moveout equation associated with the termination of this wavelet can be derived by replacing T_{direct} with $T_{\text{direct}} + \tau$, and replacing T_z with $T_z + \tau_{\text{NMO}}$ in equation C-3. That is,

$$(T_{\text{direct}} + \tau)^2 - (T_{\text{direct}} + \tau)(T_z + \tau + \Delta\tau_{\text{NMO,direct}}) = \frac{h^2}{v^2}, \tag{C-4}$$

$$\begin{aligned}&(T_{\text{direct}}^2 + 2T_{\text{direct}}\tau + \tau^2)\\ &- T_{\text{direct}}T_z - T_{\text{direct}}\tau - T_{\text{direct}}\Delta\tau_{\text{NMO,direct}}\\ &- \tau T_z - \tau^2 - \tau\Delta\tau_{\text{NMO,direct}} = \frac{h^2}{v^2},\end{aligned} \tag{C-5}$$

$$\begin{aligned}&\left[(T_{\text{direct}}^2 - T_{\text{direct}}T_z) - \frac{h^2}{v^2}\right] + (T_{\text{direct}} - T_z)\tau\\ &= (T_{\text{direct}} + \tau)\Delta\tau_{\text{NMO,direct}}.\end{aligned} \tag{C-6}$$

The first term on the left side of equation C-6 becomes zero by the relation in equation C-3. Accordingly, using the definition of $\Delta T_{\text{NMO,direct}}$ from equation 30, we can derive the moveout stretch for the direct wave from equation C-6 as follows:

$$(\Delta T_{\text{NMO,direct}})\tau = (T_z + \Delta T_{\text{NMO,direct}} + \tau)\Delta\tau_{\text{NMO,direct}}, \tag{C-7}$$

$$\frac{\Delta\tau_{\mathrm{NMO,direct}}}{\tau} = \frac{\Delta T_{\mathrm{NMO,direct}}}{T_z + \Delta T_{\mathrm{NMO,direct}} + \tau}. \quad \text{(C-8)}$$

Assuming that $\tau \ll T_z$, the moveout stretch for the direct wave can be approximated by the following expression:

$$\frac{\Delta\tau_{\mathrm{NMO,direct}}}{\tau} \approx \frac{\Delta T_{\mathrm{NMO,direct}}}{T_z + \Delta T_{\mathrm{NMO,direct}}}. \quad \text{(C-9)}$$

REFERENCES

Ajo-Franklin, J., S. Dou, T. Daley, B. Freifeld, M. Robertson, C. Ulrich, T. Wood, I. Eckblaw, N. Lindsey, E. Martin, and A. Wagner, 2017, Time-lapse surface wave monitoring of permafrost thaw using distributed acoustic sensing and a permanent automated seismic source: 87th Annual International Meeting, SEG, Expanded Abstracts, 5223–5227, doi: 10.1190/segam2017-17774027.1.

Ajo-Franklin, J., N. Lindsey, T. Daley, B. Freifeld, M. Robertson, C. Ulrich, S. Dou, E. Martin, and A. Wagner, 2015, A field test of distributed acoustic sensing for ambient noise recording: 85th Annual International Meeting, SEG, Expanded Abstracts, 2620–2624, doi: 10.1190/segam2015-5926936.1.

Ajo-Franklin, J. B., S. Dou, N. J. Lindsey, I. Monga, C. Tracy, M. Robertson, V. Rodriguez Tribaldos, C. Ulrich, B. Freifeld, T. Daley, and X. Li, 2019, Distributed acoustic sensing using dark fiber for near-surface characterization and broadband seismic event detection: Scientific Reports, **9**, 1328, doi: 10.1038/s41598-018-36675-8.

Bakku, S. K., 2015, Fracture characterization from seismic measurements in a borehole: Ph.D. thesis, Massachusetts Institute of Technology.

Bakulin, A., I. Silvestrov, and R. Pevzner, 2019, Surface seismic with DAS changes land acquisition: Presented at the Middle East Oil and Gas Show and Conference, SPE.

Bakulin, A., I. Silvestrov, and R. Pevzner, 2020, Surface seismics with DAS: An emerging alternative to modern point-sensor acquisition: The Leading Edge, **39**, 808–818, doi: 10.1190/tle39110808.1.

Bertholds, A., and R. Dandliker, 1988, Determination of the individual strain-optic coefficients in single-mode optical fibres: Journal of Lightwave Technology, **6**, 17–20, doi: 10.1109/50.3956.

Biondi, B., E. Martin, S. Cole, M. Karrenbach, and N. Lindsey, 2017, Earthquakes analysis using data recorded by the Stanford DAS array: 87th Annual International Meeting, SEG, Expanded Abstracts, 2752–2756, doi: 10.1190/segam2017-17745041.1.

Daley, T. M., B. M. Freifeld, J. Ajo-Franklin, S. Dou, R. Pevzner, V. Shulakova, S. Kashikar, D. E. Miller, J. Goetz, J. Henninges, and S. Lueth, 2013, Field testing of fiber-optic distributed acoustic sensing (DAS) for subsurface seismic monitoring: The Leading Edge, **32**, 699–706, doi: 10.1190/tle32060699.1.

Dean, T., T. Brice, A. Hartog, E. Kragh, D. Molteni, and K. O'Connell, 2016, Distributed vibration sensing for seismic acquisition: The Leading Edge, **35**, 600–604, doi: 10.1190/tle35070600.1.

Dean, T., T. Cuny, and A. H. Hartog, 2017, The effect of gauge length on axially incident P-waves measured using fibre optic distributed vibration sensing: Geophysical Prospecting, **65**, 184–193, doi: 10.1111/1365-2478.12419.

Dou, S., N. Lindsey, A. M. Wagner, T. M. Daley, B. Freifeld, M. Robertson, J. Peterson, C. Ulrich, E. R. Martin, and J. B. Ajo-Franklin, 2017, Distributed acoustic sensing for seismic monitoring of the near surface: A traffic-noise interferometry case study: Scientific Reports, **7**, 11620, doi: 10.1038/s41598-017-11986-4.

Drijkoningen, G. G., 2003, Lecture notes: Seismic data acquisition – TA3600: Delft University of Technology.

Fang, G., Y. E. Li, Y. Zhao, and E. R. Martin, 2020, Urban near-surface seismic monitoring using distributed acoustic sensing: Geophysical Research Letters, **47**, e2019GL086115, doi: 10.1029/2019GL086115.

Fernández-Ruiz, M. R., M. A. Soto, E. F. Williams, S. Martin-Lopez, Z. Zhan, M. Gonzalez-Herraez, and H. F. Martins, 2020, Distributed acoustic sensing for seismic activity monitoring: APL Photonics, **5**, 030901, doi: 10.1063/1.5139602.

Hartog, A. H., 2017, An introduction to distributed optical fibre sensors, 1st ed.: CRC Press.

Kowarik, S., M.-T. Hussels, S. Chruscicki, S. Münzenberger, A. Lämmerhirt, P. Pohl, and M. Schubert, 2020, Fiber optic train monitoring with distributed acoustic sensing: Conventional and neural network data analysis: Sensors, **20**, 450, doi: 10.3390/s20020450.

Kuvshinov, B., 2016, Interaction of helically wound fibre-optic cables with plane seismic waves: Geophysical Prospecting, **64**, 671–688, doi: 10.1111/1365-2478.12303.

Landrø, M., and L. Amundsen, 2018, Introduction to exploration geophysics with recent advances: Bivrost.

Langhammer, J., M. Eriksrud, and H. Nakstad, 2010, Performance characteristics of 4C fiber optic ocean bottom cables for permanent reservoir monitoring: 80th Annual International Meeting, SEG, Expanded Abstracts, 66–70, doi: 10.1190/1.3513871.

L'Heureux, J.-S., L. Hansen, and O. Longva, 2009, Development of the submarine channel in front of the Nidelva River, Trondheimsfjorden, Norway: Marine Geology, **260**, 30–44, doi: 10.1016/j.margeo.2009.01.005.

Lindsey, N. J., T. C. Dawe, and J. B. Ajo-Franklin, 2019, Illuminating seafloor faults and ocean dynamics with dark fiber distributed acoustic sensing: Science, **366**, 1103–1107, doi: 10.1126/science.aay5881.

Lindsey, N. J., S. Yuan, A. Lellouch, L. Gualtieri, T. Lecocq, and B. Biondi, 2020, City-scale dark fiber DAS measurements of infrastructure use during the COVID-19 pandemic: Geophysical Research Letters, **47**, e2020GL089931, doi: 10.1029/2020GL089931.

Lumens, P. G. E., 2014, Fibre-optic sensing for application in oil and gas wells: Ph.D. thesis, Technische Universiteit Eindhoven.

Martin, E. R., C. M. Castillo, S. Cole, P. S. Sawasdee, S. Yuan, R. Clapp, M. Karrenbach, and B. L. Biondi, 2017, Seismic monitoring leveraging existing telecom infrastructure at the SDASA: Active, passive, and ambient-noise analysis: The Leading Edge, **36**, 1025–1031, doi: 10.1190/tle36121025.1.

Martin, E. R., F. Huot, Y. Ma, R. Cieplicki, S. Cole, M. Karrenbach, and B. L. Biondi, 2018, A seismic shift in scalable acquisition demands new processing: Fiber-optic seismic signal retrieval in urban areas with unsupervised learning for coherent noise removal: IEEE Signal Processing Magazine, **35**, 31–40, doi: 10.1109/MSP.2017.2783381.

Mateeva, A., J. Lopez, H. Potters, J. Mestayer, B. Cox, D. Kiyashchenko, P. Wills, S. Grandi, K. Hornman, B. Kuvshinov, W. Berlang, Z. Yang, and R. Detomo, 2014, Distributed acoustic sensing for reservoir monitoring with vertical seismic profiling: Geophysical Prospecting, **62**, 679–692, doi: 10.1111/1365-2478.12116.

Monrigal, O., I. de Jong, and H. Duarte, 2017, An ultra-high-resolution 3D marine seismic system for detailed site investigation: Near Surface Geophysics, **15**, 335–345, doi: 10.3997/1873-0604.2017025.

Papp, B., D. Donno, J. E. Martin, and A. H. Hartog, 2017, A study of the geophysical response of distributed fibre optic acoustic sensors through laboratory-scale experiments: Geophysical response of fibre optic sensors: Geophysical Prospecting, **65**, 1186–1204, doi: 10.1111/1365-2478.12471.

Sladen, A., D. Rivet, J. P. Ampuero, L. De Barros, Y. Hello, G. Calbris, and P. Lamare, 2019, Distributed sensing of earthquakes and ocean-solid Earth interactions on seafloor telecom cables: Nature Communications, **10**, 5777, doi: 10.1038/s41467-019-13793-z.

Thomas, Y., B. Marsset, G. Westbrook, C. Grail, L. Géli, P. Henry, G. Çifçi, A. Rochat, and H. Saritas, 2012, Contribution of high-resolution 3D seismic near-seafloor imaging to reservoir-scale studies: Application to the active North Anatolian Fault, Sea of Marmara: Near Surface Geophysics, **10**, 291–301, doi: 10.3997/1873-0604.2012019.

Urosevic, M., A. Bona, S. Ziramov, R. Pevzner, K. Tertyshnikov, R. Martin, J. Dwyer, D. Felding, C. Guarin, and A. Foley, 2019, Seismic exploration of mineral resources in Western Australia with distribute acoustic sensing: Presented at the 25th European Meeting of Environmental and Engineering Geophysics, EAGE, 1–5, doi: 10.3997/2214-4609.201902377.

Vinje, V., J. E. Lie, V. Danielsen, P. E. Dhelle, R. Silliqi, C.-I. Nilsen, E. Hicks, and A. Camerer, 2017, Shooting over the seismic spread: First Break, **35**, 97–104, doi: 10.3997/1365-2397.35.6.89461.

Waagaard, O. H., E. Rønnekleiv, A. Haukanes, F. Stabo-Eeg, D. Thingbø, S. Forbord, S. E. Aasen, and J. K. Brenne, 2021, Real-time low noise distributed acoustic sensing in 171 km low loss fiber: OSA Continuum, **4**, 688–701, doi: 10.1364/OSAC.408761.

Walter, F., D. Gräff, F. Lindner, P. Paitz, M. Köpfli, M. Chmiel, and A. Fichtner, 2020, Distributed acoustic sensing of microseismic sources and wave propagation in glaciated terrain: Nature Communications, **11**, 2436, doi: 10.1038/s41467-020-15824-6.

Wang, Y., H. Yuan, X. Liu, Q. Bai, H. Zhang, Y. Gao, and B. Jin, 2019, A comprehensive study of optical fiber acoustic sensing: IEEE Access, **7**, 85821–85837, doi: 10.1109/ACCESS.2019.2924736.

Williams, E. F., M. R. Fernández-Ruiz, R. Magalhaes, R. Vanthillo, Z. Zhan, M. González-Herráez, and H. F. Martins, 2019, Distributed sensing of microseisms and teleseisms with submarine dark fibers: Nature Communications, **10**, 5778, doi: 10.1038/s41467-019-13262-7.

Yilmaz, O., 2001, Seismic data analysis: SEG.

Yu, C., Z. Zhan, N. J. Lindsey, J. B. Ajo-Franklin, and M. Robertson, 2019, The potential of DAS in teleseismic studies: Insights from the Goldstone

experiment: Geophysical Research Letters, **46**, 1320–1328, doi: 10.1029/2018GL081195.

Zhu, T., J. Shen, and E. R. Martin, 2021, Sensing earth and environment dynamics by telecommunication fiber-optic sensors: An urban experiment in Pennsylvania, USA: Solid Earth, **12**, 219–235, doi: 10.5194/se-12-219-2021.

Kittinat Taweesintananon received a B.S. (2009) in physics from Chulalongkorn University, and an M.S. (2011) in geophysics from Stanford University. Since 2009, he has been a geophysicist at PTTEP, where he worked as a seismic processing QC representative and a seismic processing geophysicist. In 2020, he also joined the Norwegian University of Science and Technology (NTNU) as a Ph.D. candidate. His research interests include seismic data acquisition, seismic imaging, and time-lapse seismic analysis. He is a member of SEG and EAGE.

Martin Landrø received an M.S. (1983) and a Ph.D. (1986) in physics from the NTNU. From 1986 to 1989, he worked at SERES A/S. From 1989 to 1996, he was employed at IKU Petroleum Research as a research geophysicist and manager. From 1996 to 1998, he worked as a specialist at Statoil's research center in Trondheim. Since 1998, he has been a professor at NTNU. He received the Norman Falcon award from EAGE in 2000 and the award for best paper in GEOPHYSICS in 2001. He received the Norwegian Geophysical Award in 2004 and Statoil's researcher prize in 2007. He received the SINTEF Award for outstanding pedagogical activity in 2009. In 2010, he received the Louis Cagniard Award from EAGE. He received the Eni Award (New Frontiers in Hydrocarbons) in 2011, followed by the Conrad Schlumberger Award from EAGE in 2012. In 2014, he received the IOR Award from the Norwegian Petroleum Directorate. His research interests include seismic inversion, marine seismic acquisition, and 4D and 4C seismic, including geophysical monitoring of CO_2 storage. He is a member of EAGE, SEG, the Norwegian Academy of Technological Sciences, and the Royal Norwegian Society of Sciences and Letters.

Jan Kristoffer Brenne received an M.S. (2002) in physics from NTNU. From 2002 to 2003, he worked at Optomed A/S, and since 2003, he has been employed at Optoplan AS, which was acquired by and incorporated in Alcatel Submarine Networks (ASN) in 2014. At ASN, he has worked with the development of production techniques for fiber Bragg gratings and product development of fiber-optic sensing systems, such as the Optowave system for permanent reservoir monitoring and the DAS interrogator OptoDAS. His research interests include fiber Bragg gratings, interferometric fiber-optic sensing, and DAS. He is a member of OSA and IEEE.

Aksel Haukanes received an M.S. (2018) in cybernetics from the NTNU. From 2017 to 2018, he worked as an R&D engineer for Sevendof AS. From 2018 to 2021, he worked as a field/test engineer at ASN in the R&D department, conducting field trails and developing their OptoDAS interrogator. He is currently working as a system developer for Leirvik AS.

Paper II

Citation information:

L. Bouffaut, K. Taweesintananon, H. J. Kriesell, R. Rørstadbotnen, J. R. Potter, M. Landrø, S. E. Johansen, J. K. Brenne, A. Haukanes, O. Schjelderup and F. Storvik, 'Eavesdropping at the speed of light: Distributed acoustic sensing of baleen whales in the Arctic,' en, *Frontiers in Marine Science*, vol. 9, p. 901 348, 2022. DOI: 10.3389/fmars.2022.901348. [Online]. Available: https://www.frontiersin.org/articles/10.3389/fmars.2022.901348/full (visited on 01/07/2022)

Summary:

Bouffaut et al. present the first case of wildlife monitoring using distributed acoustic sensing (DAS). By repurposing the globally-available infrastructure of sub-sea telecommunication fibre-optic cables, they show that DAS can (1) record vocalising baleen whales along a 120 km fibre-optic cable with a sensing point every 4 m, from a protected fjord area out to the open ocean; (2) estimate the 3D position of a vocalising whale for animal density estimation; and (3) exploit whale non-stereotyped vocalisations to provide fully-passive conventional seismic records for subsurface exploration.

Contributions:

L.B. wrote the manuscript, read and approved by all co-authors. L.B. and H.J.K. conducted the acoustic data analysis; L.B. designed and produced most of the results shown in the manuscript, interpreted together with H.J.K., M.L. and J.R.P.; K.T. and M.L. produced and wrote about the subsurface exploration results and interpretation. L.B., K.T. and R.A.R. developed data handling and processing routines. M.L., J.K.B., A.H., S.E.J., O.S., and F.S. conceived the experiment. A.H. and F.S. collected the DAS data. All authors contributed to the article and approved the submitted version.

frontiers | Frontiers in Marine Science

ORIGINAL RESEARCH
published: 05 July 2022
doi: 10.3389/fmars.2022.901348

Eavesdropping at the Speed of Light: Distributed Acoustic Sensing of Baleen Whales in the Arctic

Léa Bouffaut[1,2,3]*, *Kittinat Taweesintananon*[1,2,4], *Hannah J. Kriesell*[1,2], *Robin A. Rørstadbotnen*[1,2], *John R. Potter*[1,2], *Martin Landrø*[1,2], *Ståle E. Johansen*[2,5], *Jan K. Brenne*[2,6], *Aksel Haukanes*[6], *Olaf Schjelderup*[7] *and Frode Storvik*[7]

[1] Acoustics Group, Department of Electronic Systems, Norwegian University of Science and Technology (NTNU), Trondheim, Norway, [2] Centre for Geophysical Forecasting, Norwegian University of Science and Technology (NTNU) Gløshaugen, Trondheim, Norway, [3] K. Lisa Yang Center for Conservation Bioacoustics, Cornell Lab of Ornithology, Cornell University, Ithaca, NY, United States, [4] PTT Exploration and Production Public Company Limited, Bangkok, Thailand, [5] Department of Geoscience and Petroleum, Norwegian University of Science and Technology (NTNU), Trondheim, Norway, [6] Alcatel Submarine Networks Norway AS, Tiller, Norway, [7] Uninett AS (merged into Sikt, Jan. 2022), Trondheim, Norway

OPEN ACCESS

Edited by:
Won Sang Lee,
Korea Polar Research Institute,
South Korea

Reviewed by:
Hiroyuki Matsumoto,
Japan Agency for Marine-Earth Science and Technology (JAMSTEC), Japan
Brian S. Miller,
Australian Antarctic Division, Australia

***Correspondence:**
Léa Bouffaut
lea.bouffaut@cornell.edu

Specialty section:
This article was submitted to Ocean Observation, a section of the journal Frontiers in Marine Science

Received: 21 March 2022
Accepted: 20 May 2022
Published: 05 July 2022

Citation:
Bouffaut L, Taweesintananon K, Kriesell HJ, Rørstadbotnen RA, Potter JR, Landrø M, Johansen SE, Brenne JK, Haukanes A, Schjelderup O and Storvik F (2022) Eavesdropping at the Speed of Light: Distributed Acoustic Sensing of Baleen Whales in the Arctic. Front. Mar. Sci. 9:901348. doi: 10.3389/fmars.2022.901348

In a post-industrial whaling world, flagship and charismatic baleen whale species are indicators of the health of our oceans. However, traditional monitoring methods provide spatially and temporally undersampled data to evaluate and mitigate the impacts of increasing climatic and anthropogenic pressures for conservation. Here we present the first case of wildlife monitoring using distributed acoustic sensing (DAS). By repurposing the globally-available infrastructure of sub-sea telecommunication fiber optic (FO) cables, DAS can (1) record vocalizing baleen whales along a 120 km FO cable with a sensing point every 4 m, from a protected fjord area out to the open ocean; (2) estimate the 3D position of a vocalizing whale for animal density estimation; and (3) exploit whale non-stereotyped vocalizations to provide fully-passive conventional seismic records for subsurface exploration. This first example's success in the Arctic suggests DAS's potential for real-time and low-cost monitoring of whales worldwide with unprecedented coverage and spatial resolution.

Keywords: distributed acoustic sensing, bioacoustics, passive acoustic monitoring, baleen whales, cetacean conservation, blue whale, fin whale

1 INTRODUCTION

While slowly recovering from industrial whaling, many baleen whale species [*Mysticeti*; Bannister (2018)] are still threatened or critically endangered IUCN, 2021 (Version 2021-2). Simultaneously, these animals and their vast ocean habitat are subject to an increasing number of stressors driven directly or indirectly by anthropogenic activities, e.g., entanglement in fishing gear, ship strikes and

noise pollution associated with the global increase in ship traffic. Additionally, alteration of water and nutrient cycles by plastic and chemical pollution affects the entire food web (Thomas et al., 2016). Climate change has further forced cetaceans to adapt their migration routes (or their timing). Globally, many species shift poleward to their preferred sea-surface temperature (van Weelden et al., 2021).

In the Arctic, the climate is changing faster than anywhere else in the world. It has been linked to major shifts in species distributions related to sea-ice loss and the Atlantification of the region (Hamilton et al., 2021). In the high latitudes of the Svalbard archipelago, boreal species, e.g., blue whales (*balaenoptera musculus*), fin whales (*balaenoptera physalus*), humpback (*megaptera novaeangliae*) and sei whales (*balaenoptera borealis*), have been considered seasonal residents, traditionally present from late spring/early summer to the fall and spending their winters at lower latitudes (Moore et al., 2019). Recently, however, fin whales have been observed year-round (Klinck et al., 2012; Lydersen et al., 2020). Furthermore, with sea-ice loss came an increase in human activities. While ship traffic is already abundant between the Barents and North sea and Svalbard (Reeves et al., 2014; Eguíluz et al., 2016), it will likely intensify in species-rich areas (Hamilton et al., 2021) with the impending cross-Arctic shipping routes (Ng et al., 2018). Airgun signals can already be recorded all year round in the western Fram Strait (Ahonen et al., 2017). Therefore, it is urgent to establish a baseline of the environment's exposure and marine mammal vulnerability to these anthropogenic stressors to mitigate their impacts, which requires monitoring.

From fixed autonomous archival recorders to moving near-real-time multi-sensory platforms (Mellinger et al., 2007; Baumgartner et al., 2018), passive acoustic monitoring has proven to be a reliable and suitable mean for baleen whale studies (Howe et al., 2019). However, it is still relatively expensive to deploy conservation-focused hydrophones and despite the research community's global efforts and the exponentially increasing amount of data collected worldwide (Kowarski and Moors-Murphy, 2021), recorders are sparse and unevenly spread: the oceans are under-sampled (Eguíluz et al., 2016; Ahonen et al., 2017; Ahonen et al., 2021; Hamilton et al., 2021).

Meanwhile, Distributed Acoustic Sensing (DAS) has started to conquer many fields both at sea (Lindsey et al., 2019; Sladen et al., 2019; Williams et al., 2019) and on land (Daley et al., 2013; Parker et al., 2014), with exponential progress in terms of data quality, spatial coverage and bandwidth (Parker et al., 2014; Waagaard et al., 2021). Using an interrogator, DAS technology re-purposes existing dark fiber optic (FO) cables to record nano strain (Culshaw and Kersey, 2008) and has the potential for real-time monitoring over tens of kilometers (up to 171 km (Waagaard et al., 2021)) with a spatial resolution of a few meters (Goertz and Wuestefeld, 2018; Waagaard et al., 2021). Initially applied to geophysical data collection (Schenato, 2017; Hartog et al., 2018), DAS has recently aroused interest with waterborne sound sources, e.g, it has been used for near-surface ship detection and bearing estimation in the Mediterranean sea (Rivet et al., 2021). Quality assessment of the data was performed using controlled airguns sources compared (a) to ocean bottom seismometers recordings in Japan (Matsumoto et al., 2021) and (b) to seismic streamers in Norway (Taweesintananon et al., 2021). Both studies showed similar capabilities between DAS and known instrumentation in terms of frequency response and signal-to-noise ratio (SNR). This article demonstrates the untapped potential of DAS for baleen whale monitoring (**Figure 1**).

Data was acquired during the summer of 2020 around Isfjorden, Svalbard, Norway, at the doorstep of the Arctic (**Figure 2**). At that time of the year, sightings and a previous acoustic study around the archipelago demonstrate the consistent presence of blue, fin and humpback whales, and possible presence of sei whales (Nieukirk et al., 2020; Ahonen et al., 2021; Hamilton et al., 2021). Raw DAS data used for this work is available in open access (Bouffaut and Taweesintananon, 2022). Note that, to ease the reader in, the Method section (§ 4) is the last section of this article.

2 RESULTS AND DISCUSSIONS

2.1 Experimental Setup

It is common practice to lay spare fibers in telecommunication cable bundles to minimize the cost of installation. On shore, one end of such a dark fiber can be tapped without disturbing data streams and, converted into DAS using an interrogator (**Figure 1A**). The interrogator injects linear frequency-modulated optical pulses which are backscattered by anomalies in the fiber (Waagaard et al., 2021). These defects are displaced at the nanometer scale under the influence of acoustic pressure waves [but also seismic, oceanographic (Landrø et al., 2021)], introducing delays in the backscattered pulse (**Figure 1B**) (Nishiguchi, 2016). The interrogator calculates the time-differentiated phase change of the backscattered response from consecutive sweeps at regularly spaced intervals along the fiber, further named channels (**Figure 1C**). The phase change is averaged over a section of the fiber, the gauge length, and converted into longitudinal strain waveforms, analogous to acoustic pressure, for each corresponding fiber section (Hartog, 2017; Taweesintananon et al., 2021). The resulting strain data, sampled in both time and space is streamed in near-real-time from the experiment site to a remote data-processing center (**Figure 1D**).

In this experiment, we re-purposed a dark fiber (SMF-28 single mode silica) in an existing Uninett submarine telecommunication cable connecting Longyearbyen to Ny-Ålesund in Svalbard, Norway (**Figure 2A**). The fiber, heading out to the open ocean from Longyearbyen, through Isfjorden was trenched 1 to 2 m into soft sediments all along the used section and, followed the seafloor bathymetric variations (**Figure 2B**).

The Longyearbyen end of the fiber was connected to an Alcatel Submarine Networks OptoDAS interrogator, converting the first 120 km of fiber into a DAS array. We used light pulses of 1500 nm free-space wavelength with a duration of 100 μs to sample along the 120 km with a 4.08 m spatial sampling, resulting in 30000 DAS channels. In the remainder of the article, we refer to channel

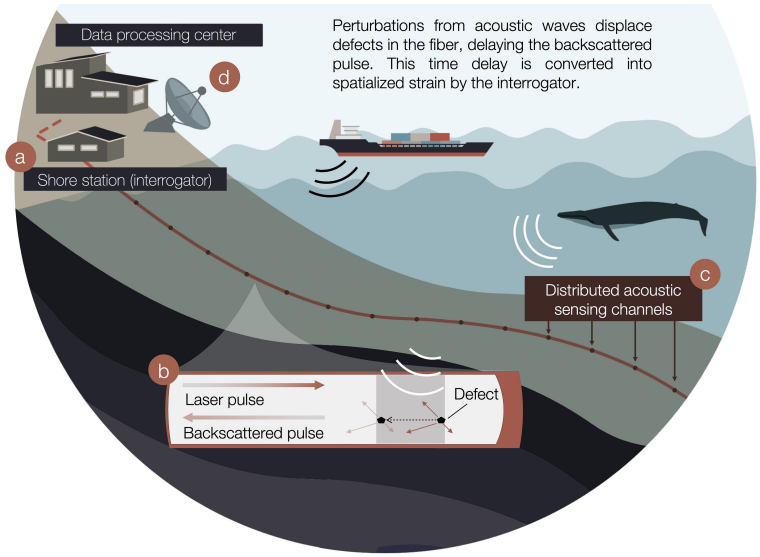

FIGURE 1 | Distributed acoustic sensing (DAS) for baleen whale monitoring. **(A)** On shore, an interrogator is connected to one end of an existing fiber optic cable to repurpose it into DAS. **(B)** It interrogates the fiber by sending laser pulses that are backscattered by anomalies while simultaneously, these defects are shifted under the effect of incoming acoustic waves. **(C)** The interrogator calculates time delays of the backscattered response at regularly spaced intervals along the fiber, named channels. Time delays are averaged over the gauge length and converted into longitudinal strain waveforms analogous to acoustic pressure. **(D)** DAS two-dimensional data is streamed in near-real-time to a remote data processing center.

positions along the FO cable from the Longyearbyen shore as simply *distance*, as illustrated on **Figure 2**. Normal signal strength decay along the fiber is 0.2 dB/km, such that the returned signal strength from 100 km is ≃−40 dB with respect to 1 km. A gauge length of 8.16 m was chosen as a compromise between maximizing the signal-to-noise ratio for the 4.08 m channel spacing (Dean et al., 2017), giving sufficiently large bandwidth for different applications (Landrø et al., 2021) and, optimizing the near-real-time data transmission rate. Data was streamed from Svalbard to NTNU (Trondheim, Norway) in near-real-time *via* Uninett's research network, using the 1 Gbit/s network interface of the interrogator. There, the data was recorded at a sampling frequency of f_s = 645.16 Hz, providing just over 300 Hz of bandwidth. The DAS data was continuously sampled over 44 days, between June 23 and August 5, 2020 and the experiment generated around 7 TB/day.

DAS instrumentation is not limited to low frequencies but its implementation is constrained by the relationship between the interrogating optical pulse intervals (the inverse of the sampling frequency) and 2-way light travel times along the physical length of the FO cable L such as $L = \frac{c_{light}}{2nf_s}$ with c_{light} = 299798458 m/s the speed of light in the fiber and n = 1.4667 the group refractive index of the fiber. For example, a 10 km-long DAS could record up to f_s = 10 kHz, without aliasing.

DAS array response to strain for a specific fiber optic/interrogator combination is a function of the gauge length, wave frequency, wave velocity and grazing angle between the source and the receivers. Due to the nature of the coupling between acoustic stress and FO cable strain, a notch in the impulse response of the fiber can be observed for perpendicular arrivals (Taweesintananon et al., 2021). The conversion from strain to acoustic pressure is a linear relation that depends on the Young's modulus of the seafloor, which varies along the FO cable. During this first experiment, calibration, e.g., using a known and georeferenced active source and co-located hydrophones as demonstrated locally in (Matsumoto et al., 2021; Taweesintananon et al., 2021) was not performed. Therefore, the results are presented in nano strain (adimensional) or in dB re. 10^{-9}. More broadly, the calibration of DAS systems has not yet been systematic and the community is working towards standardization procedures (Lindsey and Martin, 2021).

2.2 Acoustic Data Analysis

A sparse visual and aural inspection of the entire dataset (every 10 km; method described in § 4.1) revealed the presence of different known baleen whale low-frequency signatures along the fiber (**Figures 2C, D** and **Supplementary Audio S1**–**S3**). Of the 832 annotated calls, we identified 38% as North Atlantic blue whale stereotyped signals (AB call, peak frequency at 16.9 Hz; arched sounds, 9-Hz call) conforming to previous call descriptions (Mellinger and Clark, 2003). They were found

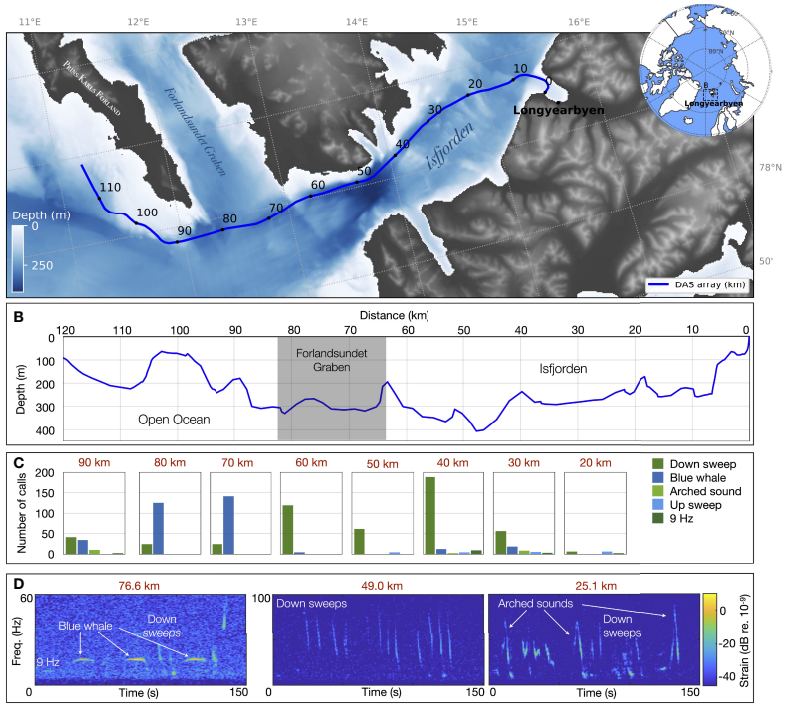

FIGURE 2 | Baleen whale vocalizations detected over the 120 km of the Svalbard underwater distributed acoustic sensing (DAS) array. **(A)** The DAS crosses Isfjorden out to the open sea, bypassing the South of Prins Karls Forland in Svalbard, Norway. The interrogator end of the fiber is located on shore in Longyearbyen, recording data with a spatial sampling of 4.08 m at a sampling frequency of f_s = 645.16 Hz between June 23 and August 5, 2020. **(B)** The DAS fiber optic cable is trenched 1-2 m deep in the seafloor and follows bathymetric variations with an average depth of ≃216 m. Number of calls **(C)** and examples **(D)** representative of the diversity of baleen whale vocalizations detected along the DAS during the entire recording period. Associated sounds are available in supplementary material **Audio 1**–**3**.

during the entire recording period with a higher number of calls detected after July 23, 2020. In four instances, sightings from whale-watching tours confirmed the presence of a blue whale in the area. Various species overlap within the observed bandwidth and produce down-sweeps (Ou et al., 2015), that were the most commonly labeled calls (60% of the annotations; peak frequency 45 ± 15 Hz, average duration 5.4 ± 2.4 s). They can be attributed to blue whales [D-calls; high variability but ≃2 s long (Oleson et al., 2007)], fin whales (40 Hz call; a 0.3 s down-sweep from 75 Hz to 40 Hz (Watkins et al., 1987)), humpback whales (non-song frequencies occur under 200 Hz and last between 0.1-4 s. (Recalde-Salas et al., 2020)), but also sei whales [e.g., a < 2 s down-sweep from 80 to 30 Hz (Tremblay et al., 2019; Nieukirk et al., 2020)]. Note that during this inspection of the (raw) unprocessed data, a unique vocalization was rarely found on two 10 km-spaced channels.

North Atlantic blue whale low frequency stereotyped calls were mostly recorded outside Isfjorden, between 70-90 km (Forlandsundet Graben), while non-stereotyped down-sweeps were detected in higher numbers in the more sheltered waters of the fjord. For blue whales, stereotyped calls have been associated with male vocal behavior (song), whereas non-stereotyped down-sweeps (D-calls) can be produced by all males, females and calves and have been associated with group social or foraging contexts (Oleson et al., 2007). No clear fin whale 20 Hz song was detected during the recording period. However, some of the down-sweeps could be fin whale 40 Hz calls, which have been linked to feeding behaviors (Širović et al., 2013; Romagosa et al., 2021). The spatial distribution of these two call types indicates potential variation in habitat use in the monitored area. The call abundance has good overlap with sighting-based models that demonstrate the increasing importance of Isfjord as habitat for large baleen whales in Western Svalbard (Storrie et al., 2018).

The spatially distributed observations provided by DAS add a new dimension to the previous (and ongoing) passive acoustic monitoring of baleen whales in Western Svalbard (Ahonen et al., 2021), highlighting potential variations at an unprecedented scale. However, in regard to the amount of data recorded, i.e.,

almost 7 TB a day during our experiment, there is a need for big-data processing methods to scan through, detect and classify vocalizations and improve species identification, specifically in heterogeneous call types such as down-sweeps (Ou et al., 2015).

2.3 Changing Perspectives: From Single Point to Distributed Sensing

One of the advantages of distributed acoustic sensing compared to typical single-point sensing is that it provides a continuity of measurement in both time and space, which requires "new" representations of the data. A common representation in the geophysical community is spatio-temporal plots also known as *t-x* plots, showing temporal variations of the strain along the FO cable (Parker et al., 2014; Lindsey and Martin, 2021). **Figure 3** is a spatio-temporal representation of two successive stereotyped blue whale calls (at 70 and 110 s), intertwined with down-sweeps (likely D-calls; at ≃90 , 95 and 127 s) between 68 and 84 km of the Svalbard DAS array, recorded on July 10, 2020 at 035530UTC. One channel of this strain data matrix (at 76.6 km) was used to draw the spectrogram in **Figure 2D**, starting 50 s earlier than **Figure 3**. A narrow [15-18] Hz butterworth band-pass filter is applied to the data to enhance the *t-x* plot's contrast. Detailed information on the pre-processing of **Figures 3** and **4** is given in § 4.2.

The low-frequency whale vocalizations (< 100 Hz) are transient acoustic signals emitted in the first tens of meters of the water column and observed on a very long array, the Svalbard DAS FO cable, trenched in the bottom of relatively shallow water (< 410 m). Therefore, signals are received only on limited portions of the array [as opposed to DAS recordings of distant earthquakes, received on the total length of an array (Lindsey et al., 2019; Sladen et al., 2019; Landrø et al., 2021)], with time delays corresponding to the difference of travel times between the source and the numerous 4.08 m-spaced channels. These time delays are inherent to the source-channel configuration and the sound speed in the water column. Spatio-temporal representations highlight the time delays on the received signals as hyperbolic wavefront arrivals, whose apex indicates the point on the FO cable closest to the source. In **Figure 3** the whale is closest to the channel at 76.3 km, and the single apex location suggests that the series of signals are emitted by a single individual (or a tight group). Benefiting from the pre-processing (§ 4.2), stereotyped signals at 70 and 110 s are recorded on ≃15 km of fiber, contrasting with the detection range of D-calls. This variation could be explained by the narrow band filtering that does not encompass the full D-calls' bandwidth and potential differences in source levels. Note that the slope of the down-sweep hyperbolas tends towards sound speed away from the apex. The received strain amplitude decay is not constant along the fiber which can be interpreted as (1) DAS directivity & local variations in the coupling between the fiber and seafloor (Matsumoto et al., 2021; Taweesintananon et al., 2021), (2) Coherent interferences in the wavefield due to a near-surface source (Lloyd's mirror effect) (Carey, 2009; Bouffaut et al., 2021), (3) Upward refracting trends in arctic waters sound propagation, with potential shadow zones and complex fjord and coastal 3D propagation (Jensen et al., 2011). Instrumental vertical and horizontal noise lines appear on the *t-x* plot. They could be removed with an additional pre-processing step, such as filtering in the frequency-wave number domain (known as *f-k* filtering) to keep only signals propagating at the speed of sound (Lindsey et al., 2019).

Figure 4 presents 130 s of recording on June 27, 2020 at 052440UTC, between 35 and 90 km of the Svalbard DAS FO

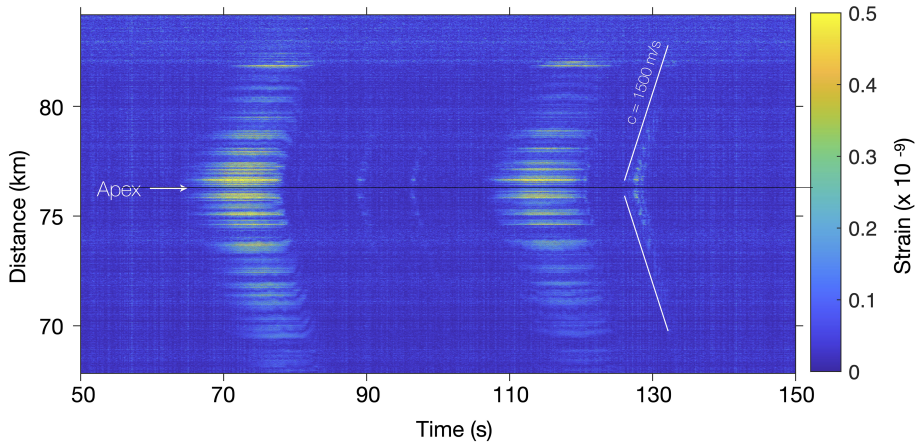

FIGURE 3 | Spatio-temporal representation of blue whale vocalizations recorded on the Svalbard DAS array. The *t-x* plot displays the temporal variations of the strain between 68 and 84 km of FO cable when receiving two successive stereotyped blue whale calls (at 70 and 110 s), intertwined with down-sweeps (D-calls; at ≃90 , 95 and 127 s) recorded on July 10, 2020 at 035530UTC. The channel at 76.6 km was used to produce for the spectrogram in **Figure 2D**.

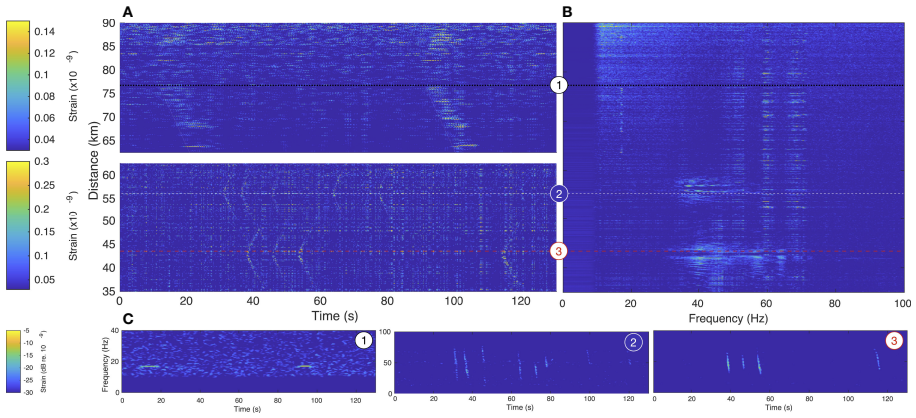

FIGURE 4 | Vocalizing baleen whales recorded simultaneously at three different locations along the Svalbard DAS array. **(A)** Spatio-temporal (*t-x*), **(B)** Spatio-spectral (*f-x*) and **(C)** Spectro-temporal (spectrogram) representations of a 130 s-long portion of recording from June 26, 2020 at 052440UTC, between 35-90 km of fiber optic cable. Each whale position (around 76.5 km, 57.5 km and 44.2 km) is given a number 1-3, to facilitate panel associations.

cable. It reveals the presence of at least 3 individuals at different locations along the cable, indicated by the dashed lines and numbers. **Figure 4A** is a spatio-temporal representation of the strain measured along the FO cable, in absolute value and separated around the mouth of the fjord at 62.25 km. To enhance the contrast, the signal out of the fjord (62.5-90 km) is band-pass filtered in the frequency domain between [16.7–17.2] Hz in (**Figure 4A**), highlighting the contribution of North Atlantic Blue whale stereotyped signals while it is band-pass filtered between [30-43] Hz to enhance down-sweeps inside the fjord (35–62.5 km). Lines with a 1500 m/s slope are added to (**Figure 4A**) to highlight the received signals.

A 16.9 Hz North-Atlantic blue whale signal is received on all represented channels outside the fjord over 27 km **Figure 4A**. The apex indicates that the vocalizing individual is closest to channels at ≃77 km. In the fjord, the down-sweeps are recorded over ≃5 km around the apexes, indicating two distinct vocalizing positions around 57 and 44 km. **Figure 4C** are spectrograms of the strain content recorded at 76.54, 57.46 and 44.22 km (Distances represented by the dashed lines from matching numbers), averaged over 2 juxtaposed channels (4.08 m apart) for noise removal and displayed in dB re. 10^{-9}. The channels used to compute the spectrograms are chosen near the apex to maximize the received amplitude.

Different features are considered to identify the calling species such as the rhythmic or inter-call intervals, the intensity or received levels, the contours in the time-frequency domain. However, the decisive characteristics to classify baleen whales is the spectral content of the signal (McDonald et al., 2006; Širović et al., 2017). We therefore propose a spatio-spectral representation of the DAS recordings or *f-x* plot, as employed in (Rivet et al., 2021), to show the spectral signature and its evolution against the distance. The method is detailed in § 4.3. An animation, showing the successive 2-s *f-x* plots is available in supplementary material **Video S1** while the integrated representation, over the 130 s of recording is displayed in **Figure 4B** with a time window duration of 2-s and 4096 samples fast Fourier transform, resulting in a *f-x* matrix with a frequency resolution of 0.16 Hz. For the three distances along the FO cable where signals were emitted, the measured bandwidth gives an indication on the species: for example, the clearly tonal signals around 70 km can be easily identified as Blue whale stereotyped call. At the two other locations, they cover a wider band, between 35-60 Hz around 57 km (whale 2) and wider 30-70 Hz around 42 km (whale 3). The received signals also show pattern of multi-path coherent interferences (e.g., notches on signals coming from whale 2), modulated by the FO cable reception sensitivity null.

Figure 4 reveals the full potential of DAS: it can simultaneously record vocalizing individuals over tens of kilometers from a protected fjord area out to the open Ocean, despite varying noise conditions. In addition to the change of environment, the increase of background noise along the length of the FO cable is due to the attenuation of the optical interrogation pulses. It can also be the effect of changes in the coupling between the FO cable and the seafloor (Matsumoto et al., 2021). The calibration of the system would enable the conversion of the measured strain into acoustic pressure, providing measurement of ambient sounds at the regional scale. The spatial distribution inherent to DAS also opens localization and near-field beamforming possibilities (§ 2.4).

2.4 Localization, Tracking and Beamforming

The localization problem is seen as an optimization process that aims to find the best match between measured and theoretical

time difference of arrivals (TDOA), estimated for different source positions (varying closest FO channel and range). Successive positions are linearized for individual tracking and the time delay information is used for near-field beamforming. The method is described in § 4.4. It was previously ground-truthed using acoustic signals received from a cargo ship and corresponding Automatic identification system (AIS) positioning, crossing the Svalbard DAS array at 86.6 km (Landrø et al., 2021).

The localization, tracking and beamforming method is illustrated in **Figure 5**, using a long (more than 10 min) recording with noticeable movement of a blue whale. *t-x* plots of portions of the recording containing calls and corresponding beamformed signals are represented. The white line indicates the variation of the estimated position of the whale along the FO cable (x_w) in time, moving from 86.4 to 87.5 km with an apparent speed of 5.4 km/h. The estimation of the range was not as precise as x_w, with a maximum of 700 m and the closest calls emitted (between 420-520 s) within a ≃100 m range. Considering the few numbers of points, no specific trend emerged, so the beamforming is set for a 200 m range. The resulting spectrogram shows a combination of singular stereotyped unit and D-calls, emitted in series, likely from the same animal.

The estimated apparent swim speed of 5.4 km/h is a minimum as the actual value increases with the angle between the FO cable and the whale's trajectory (which might not be a straight line). Nevertheless, it is within the bounds of transiting swim speeds reported for blue whales on feeding grounds, between 2-8 km/h (Bailey et al., 2009; Hucke-Gaete et al., 2018), and consistent with the behaviors associated with stereotyped singular unit and D-call vocal production (Oleson et al., 2007). A variation can be observed in the bandwidth of the beamformed down-sweeps between the successive panels **Figures 5E–H**. Besides the natural variability of D-calls, these could be introduced by the range x_w = 200 m used for the beamforming as well as the inter-channel amplitude variability (as observed in the received amplitudes **Figure 3**).

TDOA measured from D-calls are narrower than TDOA from long blue whales stereotyped calls and generally provided higher cross-correlation coefficients, ensuring better estimates of x_w. In addition, refining the range estimation would increase the resolution of the localization process and improve the beamforming. The FO cable is close to a straight line on the portion used for the localization, introducing a left/right ambiguity. This issue could be solved in Svalbard by instrumenting another already-installed FO cable running parallel to the used FO cable, only a couple of kilometers away. More generally, localization improvements require a georeferenced source to calibrate and test algorithms. Such information could be obtained using an active source, e.g., during DAS calibration experiments. Without this information, our take was to use the acoustic signal from a ship and its AIS positioning (Landrø et al., 2021). However, ship signals are continuous while whale calls are transient, requiring a different initial processing step. Another option to keep the experiment entirely passive could be to use acoustic bio-logging with Global Positioning System (GPS), combining rich information from

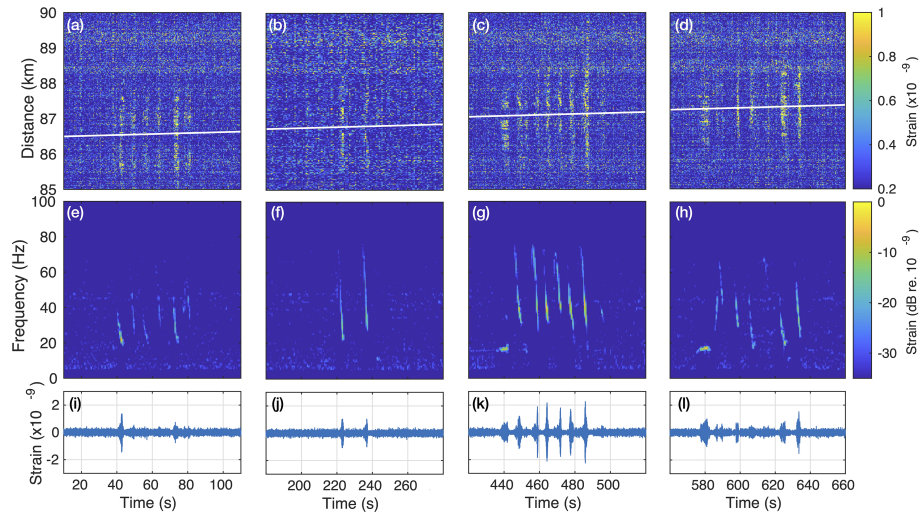

FIGURE 5 | Tracking and beamforming of series of blue whale calls recorded with a moveout on the Svalbard DAS array. **(A–D)** Spatio-temporal (*t-x*) representations of the recorded observation where the white line indicate the tracking of the apex, beamformed signals' spectrogram **(E–H)** and waveforms **(I–L)**, displayed as successive 100 s-long windows. The audio associated to **(C, G, K)** is available in supplementary material **Audio S4**.

calling individuals and their behavior to DAS observations (Oleson et al., 2007; Lewis et al., 2018).

The example in **Figure 5** demonstrates that whales passing over or near a FO cable can be detected and tracked. The information can subsequently be employed to, e.g., estimate the number of individuals in the vicinity of the array for animal density estimations and, overall, contribute to safer human/whale interactions. **Figure 5** also shows that the high SNR gain available from extended aperture array processing can be used to construct high-quality audio waveforms (**Audio S4**), with interest, e.g., for subsurface exploration (§ 2.5).

2.5 Subsurface Exploration

Recent work demonstrated that recordings of fin whale vocalizations by seabed vibration sensors contain seismic responses to subsurface geologic structures (Kuna and Nábělek, 2021). The fin whale song produced by males is composed of series of repeated short and low frequency pulses that share similarities with airgun blasts (Watkins et al., 1987; Croll et al., 2001) and when produced at different locations (e.g., while traveling) in the vicinity of a single sensor, they can be used for a common receiver song gather (Kuna and Nábělek, 2021). Concurrently, DAS has demonstrated its ability to produce seismic images of the subsurface geologic structures using conventional sources (Taweesintananon et al., 2021). This section investigates the combined use of a non-stereotyped single whale down-sweep and DAS to provide interpretable seismic profiles at two locations along the FO cable. The method is detailed in § 4.5.

Figure 6 displays correlated seismic profiles (**Figure 6A,B**) and associated received interference pattern introduced by the sea surface [**Figure 6C, D**; Lloyd's mirror effect (Carey, 2009)] obtained from two down-sweeps: one inside Isfjorden (**Figure 6A–C**) around 25 km of FO cable (**Figure 2D**, last call) and the other around 87 km of FO cable (D-call at 458 s on **Figure 5**) in Forlandsundet Graben (**Figure 6B, D**). The water depth at both location is ≃260 m explaining similar first arrival times (direct waves). The analysis and modeling of the interference patterns (**Figure 6C–D**) show a good match for a ≃20 m source depth, in the bounds of reported values for blue whales (Oleson et al., 2007; Lewis et al., 2018). Specifically source depth and range are set at z_w = 15 m and r_w = 40 m for the call emitted inside the fjord (**Figure 6A**) and z_w = 20 m and r_w = 110 m in Forlandsundet Graben (**Figure 6B**).

The correlated call profiles show direct waves, subsurface reflections, and strong water-layer multiple reflections, annotated on both panels. Comparing the sub-surface reflected waves at the two locations shows longer travel times in Isfjorden (**Figure 6A**) than in Forlandsundet Garben (**Figure 6B**), indicating a thicker shallow sedimentary rock layer in the fjord (see insets). The short-time subsurface reflections on the thinner layer of Forlandsundet Garben occur in the interference analysis window (110 ms), introducing additional lower frequency interference notches in (**Figure 6D**). Two and three (respectively **Figures 6A, B**) waterborne multiples are visible in the call profiles, indicating higher stiffness of the seafloor in Forlandsundet Garben due to different surface geology, matching traditionally-obtained subsurface structural models (Blinova et al., 2009, Figure 5F) (Asghar, 2011; Blinova et al., 2012) and reference seismic images (Schaaf, 2018, Figure 47) for the area. The subsurface primary reflection events observed in these two call profiles are reflected shear waves, which are probably corrupted by refracted shear waves from the same interfaces.

Figure 6 demonstrates that each whale frequency-modulated call recorded by DAS can be used to provide conventional seismic records for subsurface exploration. If produced and recorded at multiple locations along the array, we would obtain multiple seismic shot profiles sufficient for subsurface imaging. This example goes further than the proposal made by Kuna and Nábelek (2021) to use stereotyped fin whale male song in its use of non-stereotyped vocalizations such as D-calls, produced by all individuals in various baleen whales species (Oleson et al., 2007; Ou et al., 2015). We show that in areas where vocalizing baleen whales and DAS overlap, seismic exploration could be replaced - at least partially - by an entirely passive method keeping the environment and ecosystems undisturbed and unharmed. Therefore, DAS could reduce human activities and anthropogenic stressors such as noise in the oceans.

3 CONCLUSIONS AND PERSPECTIVES

Portions of the 1.2 million km of FO cables installed at the bottom of the world's oceans can be converted into DAS using off-the-shelf interrogators. We demonstrate through this work that, with tailored filtering, analyzing, and visualizing methods, DAS can provide cost-effective data for passive acoustic conservation with an unequaled and unprecedented spatial coverage and resolution. As a result, we are on the brink of a revolution.

However, there are a few challenges to overcome to enable worldwide eavesdropping at the speed of light. Regarding the instrumentation, telecommunication FO cables belong to various entities and require specific agreements to be accessed and tapped[1].

Because the primary purpose of these fibers is real-time data transmission, they are often equipped with signal-boosting repeaters blocking the interrogator's laser pulses and reducing the usable length to the first 50-70 km (Hartog et al., 2018) (which has the advantage of enabling higher sampling frequencies). Dedicated DAS cables are also being installed and used to improve SNR. An existing DAS system review is available in Hartog et al. (2018). Access to DAS interrogators through vendors (rent or purchase) is currently limited and negotiated by a few dedicated research groups. Making DAS instrumentation available through shared community instrument pools[2] is at the center of ongoing conversation within geophysical communities (Lindsey and Martin, 2021). Innovative applications, such as the passive subsurface exploration from whale calls depicted in § 2.5, only add to multi-disciplinary collaboration opportunities

[1] https://www.submarinecablemap.com.
[2] https://www.iris.edu/hq/initiatives/das_rcn.

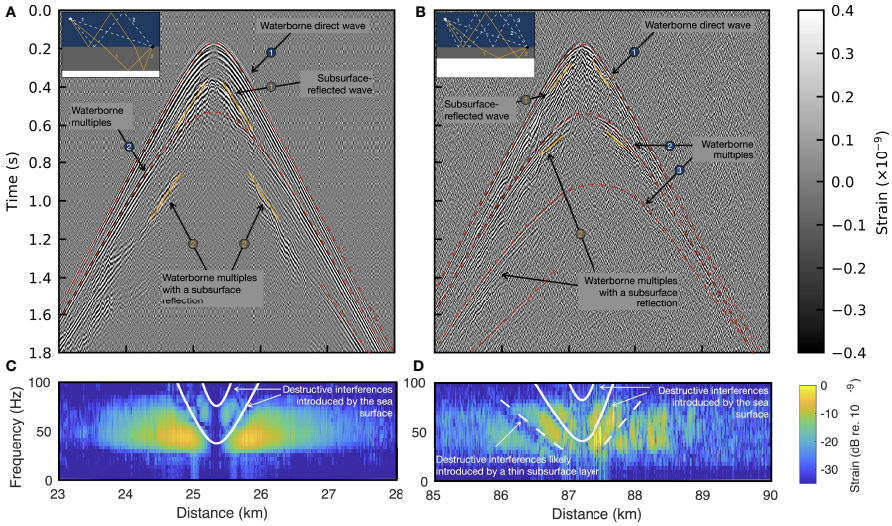

FIGURE 6 | Correlated seismic profiles from non-stereotyped whale calls. Analysis of a D-call **(A, C)** inside [last from **Figure 2D** (25.1km] and **(B, D)** outside (at 458 s on **Figure 5**) Isfjorden. **(A, B)** correlated seismic profiles at different locations. Key seismic events are highlighted and described by schematic Earth's models in the insets. Observed and modeled interference patterns generated by **(C)** the sea surface **(D)** the sea surface and a thin sub-surface layer.

fostered by DAS, contributing to a holistic approach to studying our Oceans.

Additionally, to reach its fullest potential, DAS demands big data handling methods and real-time processing along with efficient ways to scan through fast computed time-space-frequency representation of the data (the 120 km of FO cable sampled for this work generated 7 TB of data a day), process and detect potential signals of interest. Furthermore, a better understanding of the system's response to various sound sources and the availability of sensitivity response and calibration is critical in reliably estimating detection ranges. The estimation of this parameter is crucial to animal density estimations and the missing link to create occupation and presence maps to communicate to local stakeholders for conservation actions (Marques et al., 2013). This additional step can fast-track DAS from an engineering-oriented system to a robust, scalable, real-time and data-driven wildlife management information supplier, contributing to filling up the worldwide monitoring gaps for conservation.

4 METHODS

4.1 Acoustic Analysis

Benefiting from the near-real-time transmission of the data from Svalbard to Trondheim, Norway, the strain data was stored in 10 s long × 30000 channels matrices in Hierarchical Data Format (HDF5) format. For the acoustic analysis and labeling, DAS-recorded data was exported as a multichannel audio file (.wav) per day after each day, keeping a channel every 10 km of the fiber, starting from 20 km off-shore. The entirety of the 42 days of acquisition was visually (from spectrograms) and aurally examined by two independent and experimented analysts (H.J.K. & L.B.), using Raven Pro v1.6.1 (K. Lisa Yang Center for Conservation Bioacoustic, 2019). Any potential whale call was then annotated with a time-frequency-bounded box and given a label. This analysis was conducted in the same timeframe as the experiment.

4.2 Spatio-Temporal Representation Conditioning

The raw data matrices (amplitude versus time and distance) are pre-processed to improve the Signal to Noise Ratio (SNR) and contrast in the spatio-temporal representation. For **Figure 3**, a narrow [15-18] Hz butterworth band-pass filter is applied to the data and channels are stacked in pairs to reduce the background noise without altering the low frequency content. Absolute values are used in the *t-x* representation.

More processing is used for **Figure 4**, first the signal is band-pass filtered: in the frequency domain between [16.7–17.2] Hz out of the fjord (62.5-90 km) to enhance the strereotyped blue whale calls and butterworth band-pass-filtered between [30-43] Hz to enhance down-sweeps inside the fjord (35–62.5 km). Then, a 3 × 3 symmetrical 2D median filter (resolution of 12 m/4.65 ms) is applied. Absolute values are used in the *t-x* representation. The median value is successively subtracted from each time and space sample of the absolute amplitude (median subtracted from each row and column).

4.3 Spatio-Spectral Representation

For the spatio-spectral representation **Figure 4B**, a [5-110] Hz butterworth band-pass filter is applied. Then, the recordings are analyzed with a time window duration relevant to the minimum duration of whale calls. The frequency content is then evaluated on each channel by a fast Fourier transform, constructing the *t-x* matrix. The median value is subtracted from each row and column for noise reduction. It is possible to generate an image for each time window. For a representation integrated over a longer time period, we used for each point of the *t-x* grid the difference between its maximum and average value in time.

4.4 Localization, Tracking and Beamforming

DAS receivers at the positions $R\{x,r=0,z\}$ and whale position is at $S\ \{x = x_w,\ r = r_w,\ z = z_w\}$ where x is the position along the FO cable, r the cross-line range from the FO cable, z the depth and the subscript w stands for the whale. A grid of potential whale positions along the FO cable x_n and ranges r_m is established for the optimization problem, assuming a fixed calling depth z_w = 30 m (Lewis et al., 2018; Bouffaut et al., 2021). The source position is estimated by finding the theoretical TDOA that matches best the observed TDOA between all receivers an arbitrary chosen reference receiver position $R_0\{x_0,r=0,z_0\}$ such as

$$\mathrm{TDOA}_{m,n} = \frac{h_{n,m} - h_{0,m}}{c} \tag{1}$$

with c = 1500 m/s the constant sound speed, $h_{n,m} = \sqrt{|x - x_n|^2 + r_m^2 + |z - z_w|^2}$ where $|x - x_n|^2$ represents the distance between each receiver position and the tested position along the FO cable and $h_{0,m}$ is $h_{n,m}$ but for the reference R_0. The search grid used has a resolution of 50 m in x, within predefined 5 km bound around observed signal apexes ([85-90]km) and a 20 m resolution in ranges, from [0-4] km. Note, that the water depth is deeper than 300 m before 87 m and about 180 m at 90 km.

The *t-x* observation is sectioned in 5-s windows and band-pass filtered between [5-80] Hz. The 5-s-duration of the window allows for integrating the calculation over a period within the same order as the observed signals and covering potential time delays over the entire observed FO length. In the *t-x* representation of the TDOA, the apex gives information on x_w while the opening of the hyperbola gives information on r_w. The TDOA are estimated for each receiver position as the lags corresponding to the maximum of the cross-correlation between R_0 and the other receivers. Unrealistic values, e.g., $|\ \mathrm{TDOA}\ | \geq$ observed FO length over c are discarded along with $|\ \mathrm{TDOA}\ | \leq 5$ ms.

The optimization process is performed in 3 steps. First, the initialization cross-correlates measured and theoretical TDOA, where the maximum outcome initializes $S\ \{x = x_w,\ r = r_w,\ z = z_w\}$. The process is run a second time after filtering out measurement points that diverge from the initialization fit of more than the standard deviation of the difference between the theoretical and measured data points. This second run gives the best x_w. A third step is added to improve the r_w estimation by minimizing the root mean square error between the theoretical and measured points in a 1 km window around x_w.

To extend the single point localization to tracking, the localization procedure is applied iteratively to each 5-s window and only $S\ \{x = x_w,\ r = r_w,\ z = z_w\}$ points with a correlation coefficient higher than 0.85 are kept. The threshold is chosen to differentiate between signal and noise windows. A similar localization and tracking method was applied to signals received from a ship on the Svalbard DAS array and its positioning system (Automatic identification system; AIS) was used to ground-truth this localization method (Landrø et al., 2021).

Once $S\ \{x = x_w,\ r = r_w,\ z = z_w\}$ known, time delays can be compensated to beamform the received signal. In practice, only the 10 receivers with the most energy are summed-up, to limit the influence of coherent destructive interferences.

4.5 Seismic Profiles and Interferences Analysis

This method investigates the possibility of subsurface exploration from frequency-modulated whale vocalizations measured by the seabed DAS array in Svalbard. To that extent, we used 4 - 8 s long down-sweeps recorded by the array, sharing similarities with the seismic signals from vibroseis (Crawford et al., 1960), a commonly used source in land seismic exploration. Classically, shot profiles are obtained by cross-correlating the known source signal to the received signals. The following describes a method to estimate a whale call source signal from data recorded by DAS, which is then cross-correlated with the same received call over multiple channels to produce an interpretable seismic profile.

First, TDOA between channels are compensated as in § 4.4. These time-compensated signals contain coherent interferences introduced by multi-path propagation and reflection with a change of phase at an interface (e.g., at the surface), known as the Lloyd's mirror effect (Carey, 2009) or ghost effect. Specifically, destructive interferences create notches in spectral representations of the signal, varying with the source depth, the wavenumber, and the grazing angle between the source and receivers (Carey, 2009). Additionally, the time-compensated signals are auto-correlated to estimate the time of arrival of the sea-surface-reflected wave. This information is further used to remove the contribution of the interferences by applying predictive (gapped) deconvolution to the time-compensated signals (Robinson and Treitel, 2008). The result of this process is stacked to produce the source signature. Finally, the DAS strain data associated with a whale call is cross-correlated with the corresponding source signature to obtain a seismic profile.

Following the method in Pereira et al. (2020); Bouffaut et al. (2021), a side analysis provides an estimate of the source depth from frequency notches associated with the interferences patterns, using a 100 s window on the time-compensated signals to include the waterborne direct arrival and the sea-surface reflection (**Figure 6**).

DATA AVAILABILITY STATEMENT

The DAS-recorded spatio-temporal strain data supporting this analysis is available at https://doi.org/10.5281/zenodo.5823343 (Bouffaut and Taweesintananon, 2022).

ETHICS STATEMENT

Ethical review and approval was not required for the animal study because it was conducted by remote sensing using passive acoustics without any kind of contact, interactions or disturbances of the animals.

AUTHOR CONTRIBUTIONS

LB wrote the manuscript, read and approved by all co-authors. LB and HK conducted the acoustic data analysis; LB designed and produced most of the results shown in the manuscript, interpreted together with HK, ML and JP. KT and ML produced and wrote about the subsurface exploration results and interpretation. LB, KT and RR developed data handling and processing routines. ML, JB, AH, SJ, OS, and FS conceived the experiment, AH and FS collected the DAS data. All authors contributed to the article and approved the submitted version.

FUNDING

LB and HK are funded by the Research Center for Arctic Petroleum Exploration (ARCEx) partners, and the Research Council of Norway (Grant No. 228107). KT and RR are funded by the Geophysics and Applied Mathematics in Exploration and Safe production Project (GAMES) at NTNU (Research Council of Norway; Grant No. 294404). ML, JP, and SJ receive research funding from the Centre for Geophysical Forecasting (CGF) at NTNU, sponsored by Grant No. 309960 (Research Council of Norway). The acquisition of the data was financed by ARCEx and GAMES.

ACKNOWLEDGMENTS

Whale sighting provided by Svalbard Adventures and Henningsen Transport & Guiding.

SUPPLEMENTARY MATERIAL

The Supplementary Material for this article can be found online at: https://www.frontiersin.org/articles/10.3389/fmars.2022.901348/full#supplementary-material

Supplementary Audio 1 | Audio associated to the series of stereotyped North Atlantic blue whale calls and down-sweeps represented on **Figure 2D** at 76.6 km, sped up 3.5 times.

Supplementary Audio 2 | Audio associated to the series of non-stereotyped arched sounds and down-sweeps represented on **Figure 2D** 25.1 km, sped up 3.5 times.

Supplementary Audio 3 | Audio associated to the series of down-sweeps represented on **Figure 2D** at 49.0 km, sped up 3.5 times.

Supplementary Audio 4 | High-quality beamformed audio of the blue whale stereotyped and D-calls represented on **Figures 5C, G, K**, sped up 3.5 times.

Supplementary Video 1 | Animation showing the successive 2-s *f-x* plots used to construct the integrated representation of **Figure 4B**.

REFERENCES

Ahonen, H., Stafford, K. M., de Steur, L., Lydersen, C., Wiig, Ø., and Kovacs, K. M. (2017). The Underwater Soundscape in Western Fram Strait: Breeding Ground of Spitsbergen's Endangered Bowhead Whales. *Mar. Pollut. Bull.* 123, 97–112. doi: 10.1016/j.marpolbul.2017.09.019

Ahonen, H., Stafford, K. M., Lydersen, C., Berchok, C. L., Moore, S. E., and Kovacs, K. M. (2021). Interannual Variability in Acoustic Detection of Blue and Fin Whale Calls in the Northeast Atlantic High Arctic Between 2008 and 2018. *Endang. Specie. Res.* 45, 209–224. doi: 10.3354/esr01132

Asghar, A. (2011). *Processing and Interpretation of Multichannel Seismic Data From Isfjorden, Svalbard. Master's Thesis* (Bergen: The University of Bergen).

Bailey, H., Mate, B. R., Palacios, D. M., Irvine, L., Bograd, S. J., and Costa, D. P. (2009). Behavioural Estimation of Blue Whale Movements in the Northeast Pacific From State-Space Model Analysis of Satellite Tracks. *Endang. Specie. Res.* 10, 93–106. doi: 10.3354/esr00239

Bannister, J. L. (2018). "Baleen Whales (Mysticeti)," in *Encyclopedia of Marine Mammals* (Cambridge, Massachusetts: Elsevier), 62–69. doi: 10.1016/B978-0-12-804327-1.00058-3

Baumgartner, M. F., Stafford, K. M., and Latha, G. (2018). "Near Real-Time Underwater Passive Acoustic Monitoring of Natural and Anthropogenic Sounds," in *In Observing the Oceans in Real Time*. Eds. R. Venkatesan, A. Tandon, E. D'Asaro and M. A. Atmanand (Cham: Springer International Publishing), 203–226. doi: 10.1007/978-3-319-66493-4_10

Blinova, M., Faleide, J. I., Gabrielsen, R. H., and Mjelde, R. (2012). Seafloor Expression and Shallow Structure of a Fold-and-Thrust System, Isfjorden, West Spitsbergen. *Polar. Res.* 31, 11209. doi: 10.3402/polar.v31i0.11209

Blinova, M., Thorsen, R., Mjelde, R., and Faleide, J. I. (2009). Structure and Evolution of the Bellsund Graben Between Forlandsundet and Bellsund (Spitsbergen) Based on Marine Seismic Data. *Norweg. J. Geol.* 89, 215–228.

Bouffaut, L., Landrø, M., and Potter, J. R. (2021). Source Level and Vocalizing Depth Estimation of Two Blue Whale Subspecies in the Western Indian Ocean From Single Sensor Observations. *J. Acoust. Soc. America* 149, 4422–4436. doi: 10.1121/10.0005281

Bouffaut, L., and Taweesintananon, K. (2022). Das4whale: Svalbard Distributed Acoustic Sensing Dataset for Baleen Whale Monitoring. *Dataset*. doi: 10.5281/zenodo.5823343

Carey, W. M. (2009). Lloyd's Mirror-Image Interference Effects. *Acoust. Today* 5, 14–20. doi: 10.1121/1.3182842

Crawford, J. M., Doty, W. E. N., and Lee, M. R. (1960). Continuous Signal Seismograph. *Geophysics* 25, 95–105. doi: 10.1190/1.1438707

Croll, D. A., Acevedo-Gutiérrez, A., Tershy, B. R., and Urbán-Ramírez, J. (2001). The Diving Behavior of Blue and Fin Whales: Is Dive Duration Shorter Than Expected Based on Oxygen Stores? *Comp. Biochem. Physiol. Part A.: Mol. Integr. Physiol.* 129, 797–809. doi: 10.1016/S1095-6433(01)00348-8

Culshaw, B., and Kersey, A. (2008). Fiber-Optic Sensing: A Historical Perspective. *J. Lightw. Technol.* 26, 1064–1078. doi: 10.1109/JLT.0082.921915

Daley, T. M., Freifeld, B. M., Ajo-Franklin, J., Dou, S., Pevzner, R., Shulakova, V., et al. (2013). Field Testing of Fiber-Optic Distributed Acoustic Sensing (DAS)

for Subsurface Seismic Monitoring. *Lead. Edge.* 32, 699–706. doi: 10.1190/tle32060699.1

Dean, T., Cuny, T., and Hartog, A. H. (2017). The Effect of Gauge Length on Axially Incident P-Waves Measured Using Fibre Optic Distributed Vibration Sensing. *Geophys. Prospect.* 65, 184–193. doi: 10.1111/1365-2478.12419

Eguiluz, V. M., Fernández-Gracia, J., Irigoien, X., and Duarte, C. M. (2016). A Quantitative Assessment of Arctic Shipping in 2010–2014. *Sci. Rep.* 6, 1–6. doi: 10.1038/srep30682

Goertz, A., and Wuestefeld, A. (2018). Real-Time Passive Monitoring With a Fibre-Optic Ocean Bottom Array. *First. Break.* 36, 55–61. doi: 10.3997/1365-2397.n0083

Hamilton, C. D., Lydersen, C., Aars, J., Biuw, M., Boltunov, A. N., Born, E. W., et al. (2021). Marine Mammal Hotspots in the Greenland and Barents Seas. *Mar. Ecol. Prog. Ser.* 659, 3–28. doi: 10.3354/meps13584

Hartog, A. H. (2017). *An Introduction to Distributed Optical Fibre Sensors* (Boca Raton: CRC press).

Hartog, A. H., Belal, M., and Clare, M. A. (2018). Advances in Distributed Fiber-Optic Sensing for Monitoring Marine Infrastructure, Measuring the Deep Ocean, and Quantifying the Risks Posed by Seafloor Hazards. *Mar. Technol. Soc. J.* 52, 58–73. doi: 10.4031/MTSJ.52.5.7

Howe, B. M., Miksis-Olds, J., Rehm, E., Sagen, H., Worcester, P. F., and Haralabus, G. (2019). Observing the Oceans Acoustically. *Front. Mar. Sci.* 6. doi: 10.3389/fmars.2019.00426

Hucke-Gaete, R., Bedriñana-Romano, L., Viddi, F. A., Ruiz, J. E., Torres-Florez, J. P., and Zerbini, A. N. (2018). From Chilean Patagonia to Galapagos, Ecuador: Novel Insights on Blue Whale Migratory Pathways Along the Eastern South Pacific. *PeerJ* 6, e4695. doi: 10.7717/peerj.4695

IUCN (2021). *(Version 2021-2). The IUCN Red List of Threatened Species*. www.iucnredlist.org

Jensen, F. B., Kuperman, W. A., Porter, M. B., and Schmidt, H. (2011). *Computational Ocean Acoustics* (New York, NY: Springer Science & Business Media). doi: 10.1007/978-1-4417-8678-8

Klinck, H., Nieukirk, S. L., Mellinger, D. K., Klinck, K., Matsumoto, H., and Dziak, R. P. (2012). Seasonal Presence of Cetaceans and Ambient Noise Levels in Polar Waters of the North Atlantic. *J. Acoust. Soc. America* 132, EL176–EL181. doi: 10.1121/1.4740226

K. Lisa Yang Center for Conservation Bioacoustics (2019). *Raven Pro: Interactive Sound Analysis Software (Version 1.6.1) Dataset*. (Ithaca, New York: Cornell University)

Kowarski, K. A., and Moors-Murphy, H. (2021). A Review of Big Data Analysis Methods for Baleen Whale Passive Acoustic Monitoring. *Mar. Mamm. Sci.* 37, 652–673. doi: 10.1111/mms.12758

Kuna, V. M., and Nábělek, J. L. (2021). Seismic Crustal Imaging Using Fin Whale Songs. *Science* 371, 731–735. doi: 10.1126/science.abf3962

Landrø, M., Bouffaut, L., Kriesell, H. J., Potter, J. R., Rørstadbotnen, R. A., Taweesintananon, K., et al. (2021). Title: Sensing Whales, Storms, Ships and Earthquakes Using an Arctic Fibre- Optic Cable. *Earth Space. Sci. Open Arch.* 39, 1–39. doi: 10.1002/essoar.10507855.1

Lewis, L. A., Calambokidis, J., Stimpert, A. K., Fahlbusch, J., Friedlaender, A. S., McKenna, M. F., et al. (2018). Context-Dependent Variability in Blue Whale Acoustic Behaviour. *R. Soc. Open Sci.* 5, 180241. doi: 10.1098/rsos.180241

Lindsey, N. J., Dawe, T. C., and Ajo-Franklin, J. B. (2019). Illuminating Seafloor Faults and Ocean Dynamics With Dark Fiber Distributed Acoustic Sensing. *Science* 366, 1103–1107. doi: 10.1126/science.aay5881

Lindsey, N. J., and Martin, E. R. (2021). Fiber-Optic Seismology. *Annu. Rev. Earth Planet. Sci.* 49, 309–336. doi: 10.1146/annurev-earth-072420-065213

Lydersen, C., Vacquié-Garcia, J., Heide-Jørgensen, M. P., Øien, N., Guinet, C., and Kovacs, K. M. (2020). Autumn Movements of Fin Whales (Balaenoptera Physalus) From Svalbard, Norway, Revealed by Satellite Tracking. *Sci. Rep.* 10, 1–13. doi: 10.1038/s41598-020-73996-z

Marques, T. A., Thomas, L., Martin, S. W., Mellinger, D. K., Ward, J. A., Moretti, D. J., et al. (2013). Estimating Animal Population Density Using Passive Acoustics. *Biol. Rev.* 88, 287–309. doi: 10.1111/brv.12001

Matsumoto, H., Araki, E., Kimura, T., Fujie, G., Shiraishi, K., Tonegawa, T., et al. (2021). Detection of Hydroacoustic Signals on a Fiber-Optic Submarine Cable. *Sci. Rep.* 11, 2797. doi: 10.1038/s41598-021-82093-8

McDonald, M. A., Mesnick, S. L., and Hildebrand, J. A. (2006). Biogeographic Characterization of Blue Whale Song Worldwide: Using Song to Identify Populations. *J. Cetac. Res. Manage.* 8, 55–65.

Mellinger, D. K., and Clark, C. W. (2003). Blue Whale (Balaenoptera Musculus) Sounds From the North Atlantic. *J. Acoust. Soc Am.* 114, 1108–1119. doi: 10.1121/1.1593066

Mellinger, D. K., Stafford, K. M., Moore, S. E., Dziak, R. P., and Matsumoto, H. (2007). An Overview of Fixed Passive Acoustic Observation Methods for Cetaceans. *Oceanography* 20, 36–45. doi: 10.5670/oceanog.2007.03

Moore, S. E., Haug, T., Víkingsson, G. A., and Stenson, G. B. (2019). Baleen Whale Ecology in Arctic and Subarctic Seas in an Era of Rapid Habitat Alteration. *Prog. Oceanogr.* 176, 102118. doi: 10.1016/j.pocean.2019.05.010

Ng, A. K., Andrews, J., Babb, D., Lin, Y., and Becker, A. (2018). Implications of Climate Change for Shipping: Opening the Arctic Seas. *Wiley. Interdiscip. Review.: Climate Change* 9, e507. doi: 10.1002/wcc.507

Nieukirk, S. L., Mellinger, D. K., Dziak, R. P., Matsumoto, H., and Klinck, H. (2020). Multi-Year Occurrence of Sei Whale Calls in North Atlantic Polar Waters. *J. Acoust. Soc. America* 147, 1842–1850. doi: 10.1121/10.0000931

Nishiguchi, K. (2016). "Phase Unwrapping for Fiber-Optic Distributed Acoustic Sensing," in *Proceedings of the ISCIE International Symposium on Stochastic Systems Theory and Its Applications* (Fukuoka, Japan: The ISCIE Symposium on Stochastic Systems Theory and Its Applications), Vol. 2016. 81–87.

Oleson, E. M., Calambokidis, J., Burgess, W. C., McDonald, M. A., LeDuc, C. A., and Hildebrand, J. A. (2007). Behavioral Context of Call Production by Eastern North Pacific Blue Whales. *Mar. Ecol. Prog. Ser.* 330, 269–284. doi: 10.3354/meps330269

Ou, H., Au, W. W., Van Parijs, S., Oleson, E. M., and Rankin, S. (2015). Discrimination of Frequency-Modulated Baleen Whale Downsweep Calls With Overlapping Frequencies. *J. Acoust. Soc. America* 137, 3024–3032. doi: 10.1121/1.4919304

Parker, T., Shatalin, S., and Farhadiroushan, M. (2014). Distributed Acoustic Sensing–A New Tool for Seismic Applications. *First. Break.* 32, 61–69. doi: 10.3997/1365-2397.2013034

Pereira, A., Harris, D., Tyack, P., and Matias, L. (2020). On the Use of the Lloyd's Mirror Effect to Infer the Depth of Vocalizing Fin Whales. *J. Acoust. Soc Am.* 148, 3086–3101. doi: 10.1121/10.0002426

Recalde-Salas, A., Erbe, C., Salgado Kent, C., and Parsons, M. (2020). Non-Song Vocalizations of Humpback Whales in Western Australia. *Front. Mar. Sci.* 7, 141. doi: 10.3389/fmars.2020.00141

Reeves, R. R., Ewins, P. J., Agbayani, S., Heide-Jørgensen, M. P., Kovacs, K. M., Lydersen, C., et al. (2014). Distribution of Endemic Cetaceans in Relation to Hydrocarbon Development and Commercial Shipping in a Warming Arctic. *Mar. Policy* 44, 375–389. doi: 10.1016/j.marpol.2013.10.005

Rivet, D., de Cacqueray, B., Sladen, A., Roques, A., and Calbris, G. (2021). Preliminary Assessment of Ship Detection and Trajectory Evaluation Using Distributed Acoustic Sensing on an Optical Fiber Telecom Cable. *J. Acoust. Soc. America* 149, 2615–2627. doi: 10.1121/10.0004129

Robinson, E. A., and Treitel, S. (2008). *Digital Imaging and Deconvolution: The ABCs of Seismic Exploration and Processing (Society of Exploration Geophysicists)*. (Tulsa, Oklahoma: Society of Exploration Geophysicists)

Romagosa, M., Pérez-Jorge, S., Cascão, I., Mouriño, H., Lehodey, P., Pereira, A., et al. (2021). Food Talk: 40-Hz Fin Whale Calls are Associated With Prey Biomass. *Proc. R. Soc. B.* 288, 20211156. doi: 10.1098/rspb.2021.1156

Schaaf, N. W. (2018). *Tectono-Sedimentary History of the Forlandsundet Graben. Master's Thesis* (Oslo: University of Oslo).

Schenato, L. (2017). A Review of Distributed Fibre Optic Sensors for Geo-Hydrological Applications. *Appl. Sci.* 7, 896. doi: 10.3390/app7090896

Širović, A., McDonald, M., Balcazar-Cabrera, N., Buchan, S., Cerchio, S., Clark, C., et al. (2017). "Blue Whale Songs Worldwide: An Update," in *22nd Biennial Conference of the Biology of Marine Mammals (Society for Marine Mammalogy)*. (Halifax, Canada: 22nd Biennial Conference on the Biology of Marine Mammals)

Širović, A., Williams, L. N., Kerosky, S. M., Wiggins, S. M., and Hildebrand, J. A. (2013). Temporal Separation of Two Fin Whale Call Types Across the Eastern North Pacific. *Mar. Biol.* 160, 47–57. doi: 10.1007/s00227-012-2061-z

Sladen, A., Rivet, D., Ampuero, J.-P., De Barros, L., Hello, Y., Calbris, G., et al. (2019). Distributed Sensing of Earthquakes and Ocean-Solid Earth Interactions on Seafloor Telecom Cables. *Nat. Commun.* 10, 1–8. doi: 10.1038/s41467-019-13793-z

Storrie, L., Lydersen, C., Andersen, M., Wynn, R. B., and Kovacs, K. M. (2018). Determining the Species Assemblage and Habitat Use

of Cetaceans in the Svalbard Archipelago, Based on Observations From 2002 to 2014. *Polar. Res.* 37, 1463065. doi: 10.1080/17518369.2018.1463065

Taweesintananon, K., Landrø, M., Brenne, J. K., and Haukanes, A. (2021). Distributed Acoustic Sensing for Near-Surface Imaging Using Submarine Telecommunication Cable: A Case Study in the Trondheimsfjord, Norway. *Geophysics* 86, B303–B320. doi: 10.1190/geo2020-0834.1

Thomas, P. O., Reeves, R. R., and Brownell, J. R.L. (2016). Status of the World's Baleen Whales. *Mar. Mamm. Sci.* 32, 682–734. doi: 10.1111/mms.12281

Tremblay, C. J., Van Parijs, S. M., and Cholewiak, D. (2019). 50 to 30-Hz Triplet and Singlet Down Sweep Vocalizations Produced by Sei Whales (Balaenoptera Borealis) in the Western North Atlantic Ocean. *J. Acoust. Soc. America* 145, 3351–3358. doi: 10.1121/1.5110713

van Weelden, C., Towers, J. R., and Bosker, T. (2021). Impacts of Climate Change on Cetaceans Distribution, Habitat and Migration. *Climate Change Ecol.* 1, 100009. doi: 10.1016/j.ecochg.2021.100009

Waagaard, O. H., Rønnekleiv, E., Haukanes, A., Stabo-Eeg, F., Thingbø, D., Forbord, S., et al. (2021). Real-Time Low Noise Distributed Acoustic Sensing in 171 Km Low Loss Fiber. *OSA. Continuum.* 4, 688–701. doi: 10.1364/OSAC.408761

Watkins, W. A., Tyack, P., Moore, K. E., and Bird, J. E. (1987). The 20-Hz Signals of Finback Whales (Balaenoptera Physalus). *J. Acoust. Soc Am.* 82, 1901–1912. doi: 10.1121/1.395685

Williams, E. F., Fernández-Ruiz, M. R., Magalhaes, R., Vanthillo, R., Zhan, Z., González-Herráez, M., et al. (2019). Distributed Sensing of Microseisms and Teleseisms With Submarine Dark Fibers. *Nat. Commun.* 10, 1–11. doi: 10.1038/s41467-019-13262-7

Conflict of Interest: Author KT is employed by PTT Exploration and Production Public Company Limited. Author JB is and AH was employed by Alcatel Submarine Networks Norway AS. Authors OS and FS are employed by Uninett AS (merged into Sikt in Jan. 2022).

The remaining authors declare that the research was conducted in the absence of any commercial or financial relationships that could be construed as a potential conflict of interest.

Publisher's Note: All claims expressed in this article are solely those of the authors and do not necessarily represent those of their affiliated organizations, or those of the publisher, the editors and the reviewers. Any product that may be evaluated in this article, or claim that may be made by its manufacturer, is not guaranteed or endorsed by the publisher.

Paper III

Citation information:

K. Taweesintananon, M. Landrø, J. R. Potter, S. E. Johansen, R. A. Rørstadbotnen, L. Bouffaut, H. J. Kriesell, J. K. Brenne, A. Haukanes, O. Schjelderup and F. Storvik, 'Distributed acoustic sensing of ocean-bottom seismo-acoustics and distant storms: A case study from Svalbard, Norway,' *GEOPHYSICS*, vol. 88, no. 3, B135–B150, May 2023, ISSN: 0016-8033. DOI: 10.1190/geo2022-0435.1. [Online]. Available: https://doi.org/10.1190/geo2022-0435.1 (visited on 29/04/2023)

Summary:

Taweesintananon et al. review the mechanisms of ocean-bottom vibrations recorded by distributed acoustic sensing (DAS) in a submarine telecommunication fibre-optic cable in Svalbard, Norway. They show that ocean-bottom DAS data can be used to map near-surface geologic structure and to trace ocean swells back to their storm origins as far as 13,000 km away from the cable.

Contributions:

M.L., S.E.J., J.K.B., A.H., O.S. and F.S. conceived and designed the experiment. A.H. and F.S. collected data. K.T. processed data and prepared the visualisations. K.T. and M.L. analysed data with support from J.R.P., S.E.J., R.A.R., L.B. and H.J.K. M.L. and J.R.P. validated research outputs, acquired funding, and managed the project. K.T. wrote the original draft of the manuscript. All the authors conducted review and editing of the manuscript.

GEOPHYSICS, VOL. 88, NO. 3 (MAY-JUNE 2023); P. B135–B150, 9 FIGS., 1 TABLE.
10.1190/GEO2022-0435.1

Case History

Distributed acoustic sensing of ocean-bottom seismo-acoustics and distant storms: A case study from Svalbard, Norway

Kittinat Taweesintananon[1], Martin Landrø[2], John Robert Potter[2], Ståle Emil Johansen[3], Robin André Rørstadbotnen[2], Léa Bouffaut[4], Hannah Joy Kriesell[5], Jan Kristoffer Brenne[6], Aksel Haukanes[7], Olaf Schjelderup[8], and Frode Storvik[8]

ABSTRACT

Distributed acoustic sensing (DAS) leverages an ocean-bottom telecommunication fiber-optic cable into a densely sampled array of strain sensors. We demonstrate DAS applications to passive acoustic monitoring through an experiment on a submarine fiber-optic cable in Longyearbyen, Svalbard, Norway. We find that DAS can measure many types of signals in the frequency range from 0.01 to 20 Hz generated by dynamics in the atmosphere, ocean, and solid earth. These include ocean-bottom loading pressure fluctuation of ocean surface waves generated by storms, winds, and airflow turbulence, shear-wave resonances in low-velocity near-surface sediments, acoustic resonances in the water column, and propagating seismic waves. We find that DAS can record high-quality low-frequency seismo-acoustic waves down to 0.01 Hz, which could be used for subsurface exploration. Using the shear-wave resonances recorded by DAS, we can determine the subsurface structure of near-surface sediments with low velocity. In addition, we can trace ocean swells back to their origins of distant storms as far as 13,000 km away from the cable. Because DAS is capable of seismo-acoustic monitoring with a high spatial resolution of approximately 1 m over a cable of approximately 100 km long and with a broadband sensitivity down to 0.01 Hz on the low end, it can deliver great scientific value to the ocean observation and geophysics community.

INTRODUCTION

The earth's atmosphere and oceans are continuously in coupled motion. These complex motions and interactions determine the weather and, over the longer term, the climate of the planet. Oceans play a significant role in the climate, because they can retain heat and distribute it around the globe (Schmitt, 2018). Large-scale ocean currents, which are driven by variations in water density

Manuscript received by the Editor 7 July 2022; revised manuscript received 18 January 2023; published ahead of production 15 February 2023; published online 28 April 2023.
[1]NTNU – Norwegian University of Science and Technology, Acoustics Group, Department of Electronic Systems, Trondheim, Norway; NTNU – Norwegian University of Science and Technology, Centre for Geophysical Forecasting, Trondheim, Norway; and PTT Exploration and Production Public Company Limited (PTTEP), Bangkok, Thailand. E-mail: kittinat.taweesintananon@ntnu.no (corresponding author).
[2]NTNU – Norwegian University of Science and Technology, Acoustics Group, Department of Electronic Systems, Trondheim, Norway and NTNU – Norwegian University of Science and Technology, Centre for Geophysical Forecasting, Trondheim, Norway. E-mail: martin.landro@ntnu.no; john.r.potter@ntnu.no; robin.a.rorstadbotnen@ntnu.no.
[3]NTNU – Norwegian University of Science and Technology, Centre for Geophysical Forecasting, Trondheim, Norway and NTNU – Norwegian University of Science and Technology, Department of Geoscience and Petroleum, Trondheim, Norway. E-mail: stale.johansen@ntnu.no.
[4]Formerly NTNU – Norwegian University of Science and Technology, Acoustics Group, Department of Electronic Systems, Trondheim, Norway; presently Cornell University, K. Lisa Yang Center for Conservation Bioacoustics, Cornell Lab of Ornithology, Ithaca, New York, USA. E-mail: lea.bouffaut@cornell.edu.
[5]NTNU – Norwegian University of Science and Technology, Acoustics Group, Department of Electronic Systems, Trondheim, Norway. E-mail: hannah.kriesell@miljodir.no.
[6]NTNU – Norwegian University of Science and Technology, Centre for Geophysical Forecasting, Trondheim, Norway and Alcatel Submarine Networks Norway AS, Tiller, Norway. E-mail: jan.kristoffer.brenne@asn.com.
[7]Formerly Alcatel Submarine Networks Norway AS, Tiller, Norway. E-mail: aksel.haukanes@gmail.com.
[8]Uninett AS (merged into Sikt in January 2022), Trondheim, Norway. E-mail: olaf.schjelderup@sikt.no; frode.storvik@sikt.no.

caused by temperature and salinity gradients, influence the climate by exchanging heat and water with the atmosphere. A change in ocean dynamics could induce major climate variations over large areas of the earth in the long term (Bigg and Hanna, 2016). Hence, ocean surface winds, currents, and surface gravity waves are key climate variables that induce exchanges of momentum, energy, heat, salinity, gases, and other tracers between the ocean and the atmosphere (Villas Bôas et al., 2019).

Ocean surface gravity waves (OSGWs) have random properties and evolve from complex mechanisms, where gravity is the principal restoring force. Their modern studies started in the 1940s (Mitsuyasu, 2002; Wunsch, 2021), with seminal contributions from Sverdrup (1947), Stommel (1948), and Munk (1950). Wind blowing on a water surface generates OSGWs, which are modulated via breaking and nonlinear interactions. The wave breaking affects exchanges between the sea and the atmosphere (Cavaleri et al., 2012). Therefore, OSGWs are an important factor in the air-sea momentum transfer. Moreover, OSGWs are a primary source of turbulence in the upper ocean, so that they directly affect navigation, offshore structure design, and coastal erosion (Abolfazli et al., 2020). However, they are not used explicitly in constraining most ocean-atmosphere models, because high-spatial-resolution (spatial sampling under 25 km) 2D measurements of waves are normally unavailable. Such measurements could significantly improve ocean models (Wu et al., 2019).

Many instruments have been developed to measure directional OSGWs (European Cooperation in Science and Technology Action 714, Working Group 3, 2005). The classical methods such as spatial arrays and pitch-and-roll buoys have been complemented by new technologies such as displacement and Global Positioning System buoys, acoustic Doppler current meters, microwave and marine radars, coastal high-frequency radars, and real and synthetic aperture radars. However, none of these instruments can provide all the data needed to make a complete and robust estimate of the directional properties of OSGWs. Data with high spatial resolution and extensive spatial coverage would be necessary to overcome this limit. In principle, the subsurface instruments that measure ocean-bottom pressure fluctuations due to OSGWs could be deployed in spatially extended arrays for an accurate estimation of the swell directional spectra, but this would be prohibitively expensive. Therefore, compact subsurface instruments, the dimensions of which are smaller than the typical wavelength, are more widely used by the oceanographic community. Ardhuin et al. (2019) review the modern measurement techniques of OSGWs and discuss key requirements for future sea-state observation.

Distributed acoustic sensing (DAS) is a technology that can exploit the optical fiber in standard telecommunication cables as an extended spatial array of acoustic sensors (Hartog, 2017). More than 1.3 million km of submarine telecommunication cables have been deployed around the earth. Many optical fibers in these cables, often "spares," are not currently used for telecommunication. It is possible to repurpose these unused "dark" fibers to serve as ocean-bottom distributed acoustic sensors to measure, among other signals, dynamic strains caused by ocean-bottom pressure fluctuations. DAS measures the strain fluctuations at each sensing element of an optical fiber. A DAS interrogator can measure the strain data along the fiber with a length of up to 171 km in a controlled experiment (Waagaard et al., 2021). Therefore, DAS can form spatially extended arrays with very large dimensions compared with the typical length of OSGWs. In addition, DAS measures data with a spatial sampling interval of as little as 1 m, which creates arrays of many tens of thousands of sensors at a relatively low cost.

DAS in submarine fiber-optic cables can measure pressure fluctuations at the ocean bottom, originating from a variety of sources (Landrø et al., 2022). DAS in ocean-bottom telecommunication fiber-optic cables can detect OSGWs, microseisms, and earthquakes (Lindsey et al., 2019; Sladen et al., 2019). Furthermore, Williams et al. (2019) demonstrate that DAS can record the seismic waves from a distant earthquake, OSGWs, and Scholte waves. However, their spectral analyses were performed on a data record of only one hour. DAS data with a longer recording length are necessary for studying the dynamics of ocean swells, which are OSGWs originating from distant storms. For example, Zhan et al. (2021) show several dispersed signals from ocean swells from distant storms in a spectrogram computed from more than 11 days of fiber-optic sensing data using the state-of-polarization technique.

In this paper, we show that DAS can be used as a valuable tool for studying ocean dynamics. First, we describe the DAS data used in our study and their acquisition parameters. Second, we review the mechanisms of the ocean-bottom vibrations that are recorded by DAS along an ocean-bottom telecommunication cable. We also review the characteristics of the DAS data corresponding to different mechanisms of ocean-bottom vibrations. Then, we discuss the results of our analysis related to OSGWs corresponding to distant storms. Finally, we address some potential applications of DAS in the oceanographic and geophysics communities.

METHODS

Data acquisition

We used a standard single-mode G.652D fiber within an existing submarine telecommunication cable, which was installed into soft sediments at 0–2 m below the seafloor, from Longyearbyen to Ny-Ålesund in Svalbard, Norway (Figure 1). The cable is approximately 250 km long and contains 24 fibers. Here, we used one available dark fiber for DAS recordings, reaching approximately one-half of the total cable length. The cable is owned and operated by Uninett AS (merged into Sikt in January 2022), which is the National Research and Education Network in Norway.

We connected an OptoDAS interrogator, developed by Alcatel Submarine Networks, to the cable end onshore Longyearbyen. The OptoDAS interrogator sends linear optical frequency-modulated swept pulses into the fiber and receives backscattered pulses from inhomogeneities in the fiber (Waagaard et al., 2021). It calculates the time-differentiated phase changes of consecutive backscattered pulses corresponding to every spatially sampled position along the fiber. These are used to estimate the longitudinal strains of the fiber at each sampling point.

In this experiment, we use light pulses with a free-space wavelength of 1550 nm and a sampling period of 1×10^{-8} s at the optical receiver. Defined by regions of interest, we extract 30,000 channels sampled every 4.08 m along the fiber from 0 to 120 km from the interrogator. Figure 1 shows a map of the active DAS array used in our experiment. The DAS data were continuously recorded using a 1.55 ms time-sampling interval throughout the survey. The gauge length is 8.16 m. The backscattered signal strength decays by approximately 0.2 dB/km along the cable, amounting to −40 dB over 100 km. We acquired the data over 44 days from 23 June 2020 to 5

August 2020 and transferred them in near-real-time to NTNU in Trondheim over Uninett's telecommunication network for further analysis.

Data processing

The phenomena investigated in this study occur below 20 Hz. Therefore, we resample the DAS strain data from 1.55 to 20 ms with an antialiasing filter at 80% of the output Nyquist frequency. The resampled data with the Nyquist frequency of 25 Hz are used in our analysis. Data resampling also reduces the computational cost of analyzing data over a long time window. We also attenuate the interrogator noise that occurs in the whole DAS array, where the noise model is obtained by stacking all the DAS data traces from the onshore channels in a calm environment. To understand the characteristics of the data corresponding to the different mechanisms of ocean-bottom vibrations, we compare the processed data with and without the excitation from seismic waves. With this comparison, we can distinguish seismo-acoustic signals from ocean-bottom pressure fluctuation exerted by loading under ocean surface waves.

To distinguish different wave types, we analyze DAS strain data in different domains including the time-distance (t-x) domain, the frequency-distance (f-x) domain, the time-frequency (t-f) domain (also called a spectrogram), the frequency-wavenumber (f-k) domain, and the frequency-velocity (f-v) domain.

Mechanisms of ocean-bottom vibrations

The strain of a fiber section is a function of its particle motion along the fiber (Lior et al., 2021). Based on Newton's second law of motion, the particle acceleration along the fiber can be induced by the force endowed with the pressure changes with the distance (i.e., a pressure gradient) along the fiber (Stull, 2017, chapter 10). Based on Hooke's law in elastic media, the strain of the fiber section is proportional to that component of the pressure gradient projected along the direction of the fiber (Robein, 2010, chapter 1). The transfer function between seafloor displacements and pressure fields associated with OSGWs, which is called seafloor compliance, is discussed by Crawford et al. (1991). Therefore, pressure changes in space and time are detectable by DAS at the seafloor, provided they cause strains above the detection limit (due to the noise) in the order of 1 nε (nano-strain unit).

Ocean-bottom vibrations are excited by two mechanisms. The first mechanism is the loading pressure change under an overlying wave, which is attributed to the atmosphere and ocean dynamics. The second mechanism is an interaction of the ocean bottom and the propagating seismo-acoustic waves, which are generated by an earthquake, explosion, or similar energetic source. In this context, seismo-acoustic waves include not only compressional (P) waves but also shear (S) waves and interface waves.

Loading pressure responses

The total or absolute pressure under an overlying wave such as OSGWs is the summation of dynamic and static pressures. The dynamic component is the pressure fluctuation caused by the wave motion. In contrast, the static component comprises the atmospheric pressure and the hydrostatic pressure corresponding to the weight of the overlying water body.

For a progressive wave with small amplitude, we consider an OSGW as a simple sinusoidal wave profile as a function of time t and the x and y coordinates on the horizontal plane:

$$\eta(x, y, t) = a\,\cos(k_x x + k_y y - \omega t), \tag{1}$$

where η is the elevation of the water surface relative to the still-water level (SWL); a is the wave amplitude equal to one-half of the wave height (the vertical distance to its crest from the preceding trough); $\omega = 2\pi f$ is the angular frequency; and k_x and k_y are the x- and y-components of the horizontal angular wavenumber $k = 2\pi/\lambda = \sqrt{k_x^2 + k_y^2}$, respectively. Here, f and λ are the frequency and wavelength of the OSGW, respectively. Hence, the total pressure at the vertical displacement z from the SWL is given by (Coastal Engineering Research Center, 1984)

$$P_{\text{total}}(x,y,t,z) = \rho g \frac{\cosh(k(z+H))}{\cosh(kH)}\eta(x,y,t) - \rho g z + P_a, \tag{2}$$

where z equals zero at the SWL and is negative downward (toward the seafloor), H is the water depth (the depth measured from the SWL

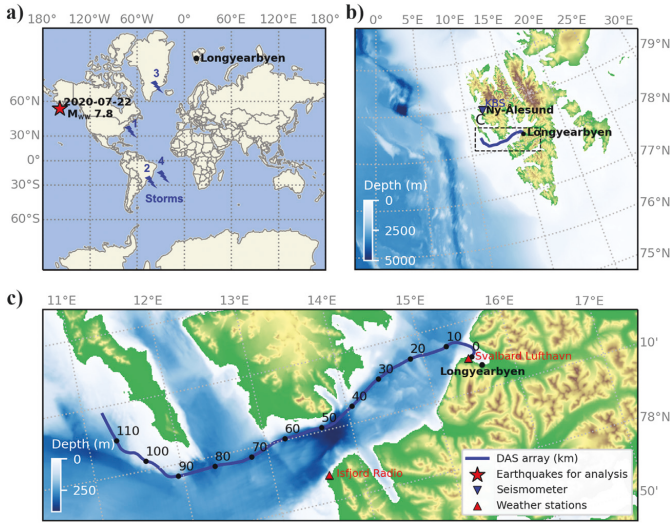

Figure 1. Maps of the ocean-bottom DAS array. (a) World map showing the array location in Longyearbyen, the epicenter of the 22 July 2020 M_{ww} 7.8 earthquake on the Alaska Peninsula, and the approximate storm locations marked in Figure 9c. (b) Regional map showing the array and the KBS seismic station. (c) Local map showing the array in the Isfjord, annotated with the distance in kilometers from the shore in Longyearbyen, and nearby weather stations.

to the seafloor), ρ is the mass density of water, $g \approx 9.81$ m/s^2 is the gravitational acceleration, and P_a is the atmospheric pressure. On the right side of equation 2, the first term represents a dynamic component, whereas the second and third terms are the hydrostatic and atmospheric pressures, respectively.

Because only the dynamic component is transferred to strains measured by ocean-bottom DAS, we derive the dynamic pressure at the seafloor ($z = -H$) from equation 2 as

$$P_{d,\text{osgw}}(x,y,t,z=-H) = P_{\text{total}} - \rho g H - P_a = \frac{\rho g \eta(x,y,t)}{\cosh(kH)}. \quad (3)$$

Because this dynamic loading pressure is a direct impact of the OSGW $\eta(x, y, t)$ as shown in equation 1, it has the same dispersion relation as the OSGW (Airy, 1841; Craik, 2004):

$$\omega^2 = gk \tanh(kH). \quad (4)$$

In addition, equation 3 implies that the dynamic loading pressure at the seafloor decays exponentially with water depth through the hyperbolic cosine function.

We may define the maximum frequency limit of OSGWs as the highest frequency at which the OSGW dynamic loading pressure is observable using the same approach as Williams et al. (2022), based on Crawford et al. (1991). Let $n = \lambda/H$ be the ratio between wavelength and water depth, so that the angular wavenumber can be written as $k = 2\pi/(nH)$, and, hence, the frequency of OSGWs is derived from equation 4 as

$$f_{\text{osgw}} = \sqrt{\frac{g}{2\pi n H} \tanh\left(\frac{2\pi}{n}\right)}. \quad (5)$$

By using $n = 0.827$ with an approximation that $\tanh(2\pi/n) \approx 1$, we derive the maximum frequency of OSGWs from equation 5 as

$$f_{\text{osgw,max}} \approx \sqrt{\frac{g}{2\pi H \times 0.827}}. \quad (6)$$

This maximum frequency corresponds to the dynamic loading pressure with a sufficiently low magnitude at $P_{d,\text{osgw}} \approx 0.001 \times \rho g \eta$. Here, we derive equation 6 by using $n = 0.827$ in equation 5, such that the corresponding dynamic loading pressure (using $1/\cosh(kH) = 1/\cosh(2\pi/n) \approx 0.001$ in equation 3) has a sufficiently low magnitude at 0.1% of the dynamic loading pressure at SWL, i.e., $P_{d,\text{osgw}} \approx 0.001 \times \rho g \eta$. This low-magnitude threshold is lower than the threshold of 0.37% using $n = 1$ by Williams et al. (2022). Note that the choice of selecting this low-magnitude threshold is arbitrary. It can be any sufficiently low number that highlights the high-frequency limit of observable OSGWs in DAS data.

The tide can also affect the OSGW dynamic loading pressure at the seafloor, as discussed in Williams et al. (2022). Here, we derive an explicit formula of its maximum frequency in the presence of the tide, which causes SWL to change with time. Let $\zeta(t)$ be the sea-level change defined as the vertical displacement with positive upward from the mean-sea level (MSL) to the time-variant SWL. Then, the water depth is written as $H(t) = H_{\text{avg}} + \zeta(t)$, where H_{avg} is the time-invariant depth measured from MSL to the seafloor. From equation 2, we derive the dynamic pressure at the seafloor associated with OSGWs and the tide as

$$P_{d,\text{osgw-tide}}(x,y,t,z=-H) = P_{\text{total}} - \rho g H_{\text{avg}} - P_a = \frac{\rho g \eta(x,y,t)}{\cosh(k(H_{\text{avg}} + \zeta(t)))} + \rho g \zeta(t). \quad (7)$$

From equation 4, based on equation 7, we can determine the maximum frequency of OSGWs corresponding to the sufficiently low dynamic pressure at $P_{d,\text{osgw-tide}} \approx 0.001 \times \rho g \eta$:

$$f_{\text{osgw-tide,max}} = \frac{1}{2\pi}\sqrt{g k_{\text{osgw-tide,max}} \tanh(k_{\text{osgw-tide,max}}(H_{\text{avg}} + \zeta(t)))}, \quad (8)$$

where

$$k_{\text{osgw-tide,max}} = \frac{1}{H_{\text{avg}} + \zeta(t)} \operatorname{arccosh}\left(\frac{\eta}{0.001 \times \eta - \zeta(t)}\right). \quad (9)$$

Equation 9 only exists if $0 \le 0.001 \times \eta - \zeta(t) \le \eta$. Later in this paper, we visualize the effect of the tide on the maximum frequency of the OSGW dynamic loading pressure at the seafloor by applying $\eta = 1000 \times \zeta_{\text{max}}$ to equations 8 and 9. Here, ζ_{max} is the maximum sea-level change from MSL over the entire recording period.

It is important to note that any ocean surface wave can cause dynamic loading pressure on the seafloor. The ocean surface waves can be classified by wave period or frequency, disturbing force, and restoring force (Coastal Engineering Research Center, 1984). For waves in the frequency range from 0.01 to 20 Hz, the ocean surface waves are typically generated by the friction exerted by winds on the ocean surface. Either gravity or surface tension can be the principal restoring force, i.e., the force that attempts to return the fluid to its equilibrium position. OSGWs have gravity as the restoring force. They are called "seas" when the waves are under the influence of local wind in a generating area, and they are called swells when the waves move out of the generating area and are no longer influenced by significant wind action. On the other hand, ocean surface waves are called capillary waves when the surface tension is the principal restoring force. The ocean surface waves that are affected by gravity and surface tension are called gravity-capillary waves (Părău et al., 2005). The impact of surface tension on the wave amplitude is lower than gravity, such that the dynamic loading pressure on the seafloor is dominated by OSGWs.

Nevertheless, strong winds and airflow turbulence may cause unstable ocean surface waves and disruptions to the sea surface. Surface disruptions such as wave breaking could cause additional forces and, hence, slamming pressure onto the ocean bottom. Breaking wave loads are an element of the dynamic loading pressure on the seafloor. Reviews of the breaking waves and their characteristics in deep and intermediate waters can be found in, e.g., Perlin et al. (2013), Robertson et al. (2013), and Barthelemy et al. (2018). In addition, the slamming pressure resulting from breaking wave loads in shallow water is studied by Yang and Cai (2022). However, the wave-breaking mechanism and the breaking wave loads onto the seafloor, especially in deep and intermediate waters, have not been fully understood and are still under research.

Seismo-acoustic responses

Seismo-acoustic waves propagating through the seawater and the solid earth cause strain fluctuation in an ocean-bottom fiber-optic cable upon their arrival. Seismo-acoustic waves are emitted by a great variety of sources from natural and anthropogenic origins, as discussed by Schwardt et al. (2022). At some specific frequencies equal to or close to the natural frequencies (also known as the eigenfrequencies) of the system, the seismo-acoustic waves can excite modes of vibration in the media where they are propagating, which are called standing waves or normal modes. Normal modes can occur naturally in any layer and be caused by either P or S waves, even in the absence of any external driving force. In each mode, the wave amplitude significantly increases if we apply a periodic force with a frequency close to the natural frequency. This phenomenon is called resonance.

In seawater, seismo-acoustic waves can propagate in a long range via bottom-interacting paths in the form of guided waves at different propagation modes (Landrø and Hatchell, 2012). The lowest frequency in which a certain mode can propagate is the cutoff frequency. That is, a cutoff frequency is the critical frequency below which the water channel ceases to act as a waveguide, causing energy radiated by the source to propagate directly into the bottom (Jensen et al., 2011). The cutoff frequencies for the guided waves in the water layer can be determined from

$$f_n = \frac{(2n-1)c_w}{4H\sqrt{1-(c_w/c_p)^2}}, \tag{10}$$

where n is a positive integer, indicating the order of the normal mode (Landrø and Hatchell, 2012). This expression is exact only for a homogeneous water column with water depth H and sound speed c_w overlying a homogeneous bottom with sound speed c_p. In the case of a rigid seafloor ($c_w/c_p \ll 1$), the cutoff frequencies in equation 10 can be written as

$$f_n \approx \frac{(2n-1)c_w}{4H}. \tag{11}$$

Assuming that the P-wave velocity below the seafloor is higher than the P-wave velocity in the water, we use equation 11 as a simple guide in this paper to characterize the normal modes of acoustics in the water layer.

At a soft sedimentary seafloor (a fluid-solid interface), of which the S-wave velocity in the bottom layer (c_s) is much lower than the P-wave velocities in the water (c_w) and the bottom layer (c_p), there exists the Scholte interface mode (the zeroth mode). This Scholte interface mode has no cutoff frequency, and its (horizontal) phase velocity is identical to the Rayleigh-wave velocity for extremely low frequencies and approaches the Scholte-wave velocity for extremely high frequencies (Rauch, 1980). Raising the frequency scale, the dispersion curves for the (horizontal) phase velocities of the higher-order modes correspond to the propagation modes of the body waves (either P or S waves) in the layers above and below the fluid-solid interface, i.e., the water and ocean-bottom layers (Westwood et al., 1996).

Wave propagation modes can occur for either P or S waves in any solid layer below the seafloor. The S-wave resonances can be observed at frequencies between 0.3 and 7.5 Hz, when surficial marine sediments over a rock substrate have low S-wave velocities (Godin et al., 2021). These resonances are generated by the normal reflection of S waves. The S-wave resonances as well as the normal modes and propagation modes of S waves in the seafloor sediments are discussed and studied in several publications (Webb, 1998; Stephen et al., 2003). Based on the theoretical explanation given by Godin and Chapman (1999), we may investigate this phenomenon using a power-law S-wave velocity profile of the soft seafloor sediments in the form $c_s(z_s) = c_{s,0} z_s^{\nu}$, where z_s is the depth below the seafloor (a fluid-solid interface). Here, $c_{s,0}$ and ν are the two nonnegative constants, whereas z_s equals zero at the seafloor and is positive downward (toward the center of the earth). Let $z_s = H_s$ be a rigid boundary, so that the soft-sediment thickness is equal to H_s. According to Godin and Chapman (1999, equation 17), the nth S-wave resonance frequency can be determined from

$$f_{s,n} = \frac{c_{s,0}(1-\nu) j_{m,n}}{2\pi H_s^{1-\nu}}, \tag{12}$$

where n is a positive integer indicating the order of the normal mode, $m = (2\nu-1)/(2(1-\nu))$ is a monotonically increasing function of ν, and $j_{m,n}$ is the nth positive zero of the Bessel function $J_m(x)$. For $n \gg 1 + m^2$, we can apply the asymptotic expansion for the Bessel function zeros to equation 12, and then we obtain (Godin and Chapman, 1999, equation 18)

$$f_{s,n} \approx \frac{\left(n + \frac{m}{2} - \frac{1}{4}\right) c_{s,0}(1-\nu)}{2H_s^{1-\nu}} + \mathcal{O}\left(\frac{1}{n}\right). \tag{13}$$

For the homogeneous sediment with a constant S-wave velocity ($\nu = 0$ giving $c_s = c_{s,0}$ and $m = -(1/2)$), equation 13 has the same form as the cutoff frequencies in the homogeneous water layer in equation 11, i.e., $f_{s,n} \approx (2n-1)c_{s,0}/(4H_s)$.

Later in this paper, we show that ocean-bottom DAS can measure the S-wave modes in seafloor sediments. Using the relation in equation 13, we can determine the seafloor soft-sediment thickness (H_s) from the first S-wave resonance frequency ($f_{s,1}$), which is estimated from the frequency analysis.

Origin of ocean swells

Ocean-bottom seismic sensors can detect the loading pressure associated with ocean swells generated from large storms occurring several thousand kilometers away. Bromirski and Duennebier (2002) discuss the amplitude characteristics and wave spectra of these swells. The dispersion relation for OSGWs in deep water predicts that low-frequency waves will arrive before higher-frequency waves. Also, it depicts the resulting linear upsweep characteristics of ocean swells in spectrograms (time-frequency representations) computed from ocean-bottom seismic data (Bromirski and Duennebier, 2002, Figure 11). Using the method described by Lin et al. (2018) based on Munk et al. (1963), we can also trace ocean swells, measured by DAS, back to their originating distant storms. We use the time-frequency gradients measured in spectrograms to calculate the great-circle distances and traveltimes of the storm-induced ocean swells traveling from the storm centers to the DAS receiver.

Lin et al. (2018), based on Munk et al. (1963), derive the expression for the propagation distance of an ocean swell as

$$x = \frac{g}{4\pi\left(\frac{df}{dt}\right)}, \tag{14}$$

where f is the frequency of the ocean swell. Here, df/dt is the time-frequency gradient or slope of the linear upsweep trend. Furthermore, the group velocity (c_g) of the swell in deep water can be computed from

$$c_g = \frac{1}{2}\sqrt{\frac{g}{k}} \approx \frac{g}{4\pi f}, \tag{15}$$

where f is the frequency of the wave. Then, we can estimate the traveltime (t) of the ocean swell from the storm center to the DAS receiver from

$$t = \frac{x}{c_g}. \tag{16}$$

In short, we first estimate the slope of a linear upsweep trend in the spectrogram and determine the propagation distance of the swell using equation 14. Next, we use the starting frequency of the trend in the spectrogram to compute the group velocity and the traveltime using equations 15 and 16, respectively. The estimated distance and traveltime help to characterize the storms that produced the observed ocean swells.

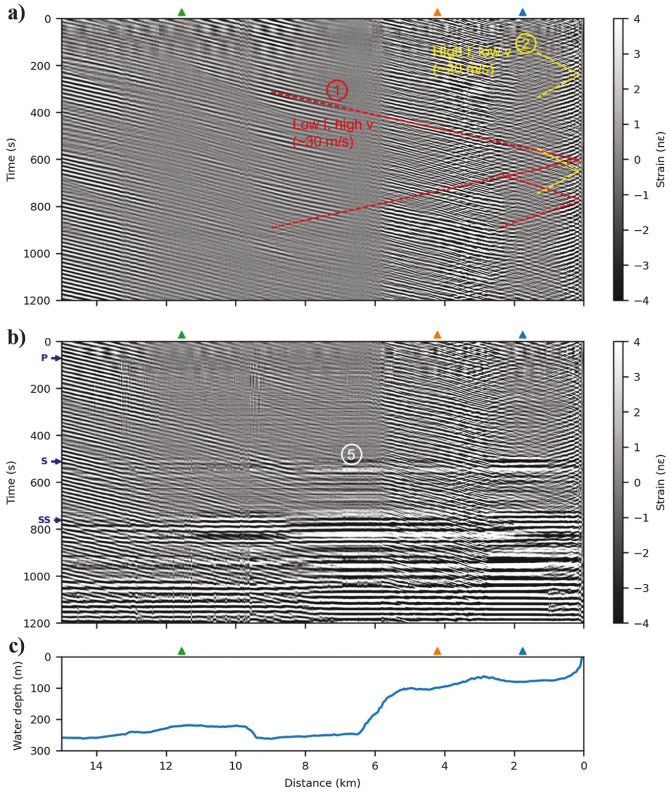

Figure 2. DAS strain data from 0 to 15 km along the cable. (a) The strain data in the 1200 s time window from 2020-07-22T06:00:02Z containing no strong seismic waves from significant earthquakes. (b) The strain data in the 1200 s time window from 2020-07-22T06:20:02Z containing strong seismic waves (P, S, and SS waves) from the 22 July 2020 M_{ww} 7.8 earthquake on the Alaska Peninsula. (c) The water-depth profile along the cable.

RESULTS AND DISCUSSION

Data characterization

Based on our analysis of the data in the frequency range between 0.01 and 20 Hz, we observe six signatures associated with different wave types in the ocean-bottom DAS strain data in Svalbard. Figures 2, 3, 4, 5, 6, 7, and 8 are used to identify the phenomena behind the six wave types marked as events 1–6 in Figure 3. These phenomena shall be discussed in detail in the next subsections, but we here provide a brief overview as follows. Events 1–3 are associated with the loading pressure responses of ocean swells (OSGWs originating from distant storms), OSGWs exerted by winds, and ocean surface disruptions caused by strong winds and airflow turbulence, respectively. In contrast, events 4–6 belong to the following seismo-acoustic responses, respectively: S-wave resonances in the seafloor sediments, seismic waves generated from various sources (earthquakes, microseisms, anthropogenic sources, etc.), and acoustic propagation modes in the water channel.

This section is structured into three subsections. First, we introduce the data and relevant illustrations used for characterizing different wave types in ocean-bottom DAS data. Second, we discuss the wave phenomena related to ocean-bottom loading pressure responses. Finally, we discuss the seismo-acoustic responses observed in the ocean-bottom DAS data.

Data description

On 22 July 2020 at 06:12:44 Universal Time Coordinated (UTC), represented as 2020-07-22T06:12:44Z according to the extended format defined in International Organization for Standardization (ISO) 8601-1:2019, an earthquake with a moment W-phase magnitude (M_{ww}) of 7.8 occurred at a depth of 28 km approximately 100 km south of the Alaska Peninsula (Figure 1a). The earthquake was detected by seismic stations worldwide and our DAS array near Longyearbyen, which is approximately 5100 km away from the epicenter on a great circle. At the DAS channel at 36 km inline distance from the shore, the approximate arrival times of the P, S, and SS waves are 510, 950, and 1200 s, respectively, from the earthquake's origin time.

We compare the DAS strain data before and after the seismic waves from the earthquake in Alaska arrive. As shown in Figure 2a, the data in the 1200 s time window from 2020-07-22T06:00:02Z contain no seismic waves from significant earthquakes. In contrast, Figure 2b shows

the data in the 1200 s time window from 2020-07-22T06:20:02Z that contain strong seismic waves from the earthquake in Alaska. The P, S, and SS waves arrive at the DAS array 72, 512, and 762 s from 2020-07-22T06:20:02Z, respectively. The seismic waves are marked as event 5 in Figure 2b (for consistency with the annotation in Figure 3). In this paper, our discussion is primarily based on a series of figures representing different domains of the data from the two 1200 s time windows shown in Figure 2.

From Figure 2a, we observe low-frequency right- and left-dipping wavetrains (marked as event 1) with an apparent velocity of approximately 30 m/s in all the channels from 0 to 15 km from the shore, where the water depth ranges from 0 to 280 m. In addition, we observe right- and left-dipping wavetrains (marked as event 2) with the higher frequency and the lower apparent velocity at 20 m/s only in shallow water with less than 100 m water depth.

Figure 3a and 3b shows the *f-x* spectral analysis from 0.01 to 20 Hz of the processed DAS strain data from the 1200 s time window before the arrivals of strong seismic waves from the Alaska earthquake, which corresponds to the strain data shown in Figure 2a. Note that the processed data have a time-sampling interval of 20 ms, i.e., the Nyquist frequency is 25 Hz. A power spectrum is computed by a discrete Fourier transform along the time axis of the processed data within the whole 1200 s time window, in which the normalization factor is one (unscaled) for the forward transform. The average power spectra over 251 channels (500 m radius) around three selected locations are shown in Figure 3a. The locations are selected to represent the data recorded at different water depths and distances from the shore. The power spectra of individual channels are combined to produce the distance-frequency plot shown in Figure 3b. Similarly, the *f-x* spectral analysis of the DAS strain data in Figure 2b, from the 1200 s time window containing strong seismic waves from the Alaska earthquake, is shown in Figure 3c and 3d.

In three different frequency bands, Figure 4 shows the band-limited DAS strain data in the time window between 100 and 130 s from 2020-07-22T06:00:02Z, i.e., the data without strong earthquake signals in Figure 2a. The band-limited data are used to understand the *t-x* characteristics of the wave types in different frequency bands. Based

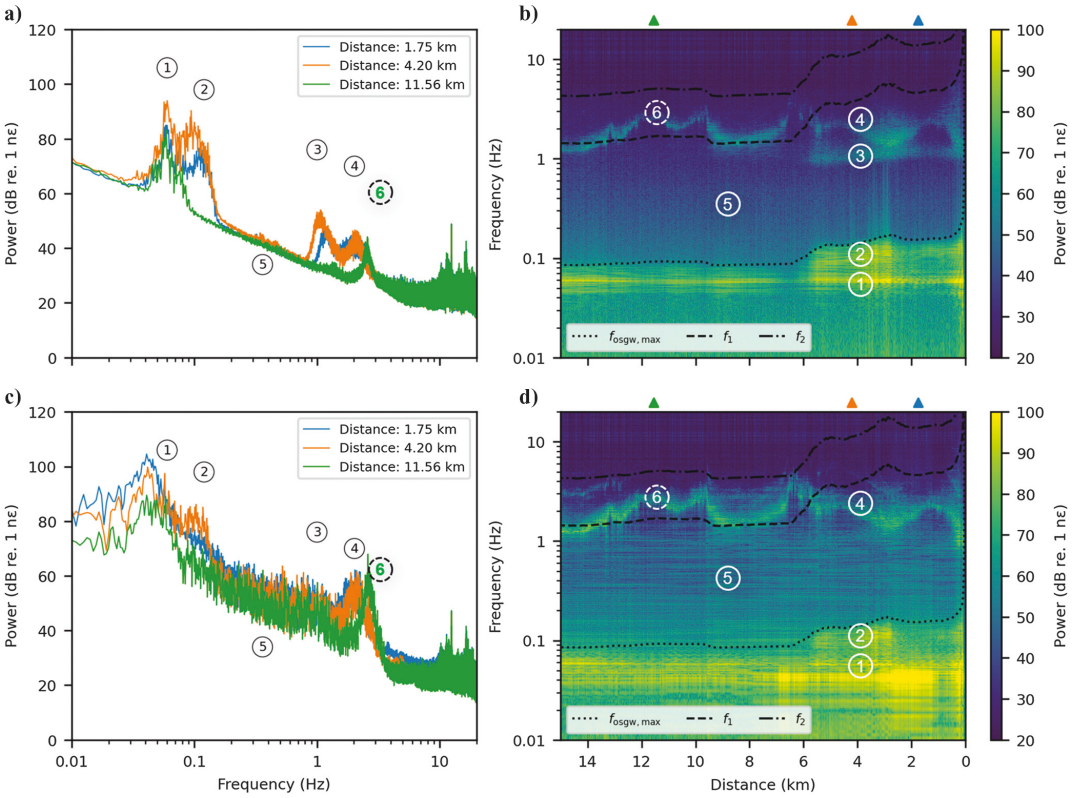

Figure 3. Spectral analysis of DAS strain data. (a) The average power spectra at selected locations along the cable and (b) the power spectral profile in the 1200 s time window from 2020-07-22T06:00:02Z containing no strong seismic waves from significant earthquakes. (c) The average power spectra at the same locations and (d) the power spectral profile in the 1200 s time window from 2020-07-22T06:20:02Z containing strong seismic waves (P, S, and SS waves) from the 22 July 2020 M_{ww} 7.8 earthquake on the Alaska Peninsula. The average power spectra in (a and c) are computed over 251 recording channels (500 m radius) around each location. The numeric annotations highlight the six key events discussed in the text. The colored triangles in (b and d) mark the locations associated with the power spectra in (a and c).

on the annotations shown in Figure 3a, events 1 and 2 are observed in 0.005–0.2 Hz (Figure 4c), events 3 and 5 are observed in 0.2–1.2 Hz (Figure 4b), and event 4 is observed in 1.2–20 Hz (Figure 4a).

Figure 5 shows the frequency analysis of the data without strong earthquake signals from 0 to 76 km distances along the cable at the same time window as shown in Figure 2a. To avoid poor quality due to image downsampling, we only plot the data along the 76 km distance of the fiber-optic cable in this paper. Figure 6 shows the *f-k* spectra of the DAS strain data at four individual spatial locations, with and without the strong seismic waves from the Alaska earthquake. Figure 7 shows the spectrograms of the DAS strain data calculated at three individual recording channels. Figure 8 shows the same frequency analysis as Figure 5 on the data with strong earthquake signals from Alaska at the same time window as shown in Figure 2b.

Loading pressure responses

The 0.06 Hz peak marked as event 1 in Figure 3b presents in all the recording channels from 0 to 15 km along the cable, where the water depth ranges from 0 to 280 m. In Figures 2a and 4c, the waves associated with event 1 are seen to propagate at the apparent velocity of 30 m/s mainly toward the shore, and their reflections at the shore cause weaker wavetrains to propagate back to the open ocean. As shown in Figure 3b, the frequency of event 1 is lower than the maximum frequency of OSGWs ($f_{\mathrm{osgw,max}}$) calculated from equation 6 using the water depths from local bathymetry along the fiber-optic cable. This frequency characteristic is also observed in Figure 5b, which shows the frequency analysis on the data without strong earthquake signals from 0 to 76 km distances along the cable at the same time window as shown in Figure 2a.

If event 1 is the dynamic loading pressure response of OSGWs, its amplitude must decay with water depth, as described in equation 3. To clarify this, we will compare the root-mean-square (rms) of the amplitude at a frequency of approximately 0.06 Hz from the *f-x* power spectra with an amplitude trend modeled by equation 3 as plotted in Figure 5c. In Figure 5c, we model the strain amplitude associated with OSGWs at a constant frequency of 0.06 Hz using an approach similar to Williams et al. (2019, Figure 6), as described next. First, we solve the dispersion relation in equation 4 for the angular wavenumber (k) using the Newton-Raphson method (You, 2008, equations 2 and 3). Then, we compute the dynamic pressure at the seafloor ($P_{d,\mathrm{osgw}}$) using equation 3. Finally, we convert the seafloor pressure into a fiber strain by multiplying $P_{d,\mathrm{osgw}}$ with a scaling factor, which is determined by data fitting for a linear relationship between pressure and strain. This model assumes that OSGW amplitude (one-half of the wave height) is invariant with water depth.

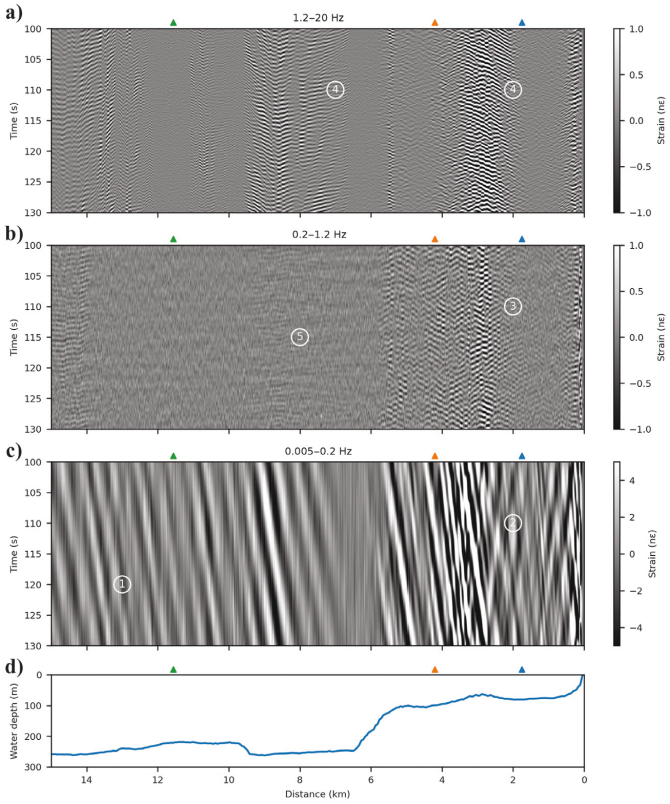

Figure 4. Band-limited DAS strain data. The strain data from Figure 2a are decomposed by band-pass filters into three frequency bands: (a) 1.2–20 Hz, (b) 0.2–1.2 Hz, and (c) 0.005–0.2 Hz. (d) The water-depth profile. The recording time starts from zero at 2020-07-22T06:00:02Z. The colored triangles mark the locations associated with the spectra shown in Figure 3.

Figure 5c compares the powers corresponding to the observed rms amplitude and the modeled amplitude at 0.06 Hz. We observe a good correspondence between the observed and modeled amplitude for the distance greater than 20 km from the shore. In contrast, the strain amplitude of event 1 in the inner part of the Isfjord (<20 km from the shore) is obviously weaker than the modeled amplitude. This amplitude mismatch implies that the OSGW amplitude in the inner part of the Isfjord is smaller than the wave in the deeper water in the outer part. According to Kakinuma and Kusuhara (2022), the amplitudes of the ocean-surface waves depend on not only the water depth but also the width of the water channel (lateral). Because the width of the Isfjord mostly increases from the outer to the inner parts (from west to east), the OSGW amplitude in the inner part near Longyearbyen tends to be lower than the OSGW amplitude in the outer part. Hence, the amplitude mismatch of event 1 and the OSGW model shown in Figure 5c could be an effect of the topography of the water channel.

Figure 6 shows the *f-k* spectra of the DAS strain data at four individual spatial locations, with and without strong seismic waves from the Alaska earthquake. In all the *f-k* spectra, we observe that the 0.06 Hz peak is aligned with

the OSGW dispersion curve (the dashed blue line), which is calculated from equation 4. From the spectrograms shown in Figure 7, we observe that the frequency of event 1 slowly increases with time. According to equation 14, the low time-frequency gradient or slope of event 1 implies that the sources of the OSGWs are thousands of kilometers away from Svalbard. Thus, event 1 corresponds to the loading pressure fluctuation associated with the overlying ocean swells originating from distant storms. In the next subsection, we study event 1 for storm monitoring in more detail.

The 0.12 Hz peak marked as event 2 in Figure 3b is pronounced only in shallow water (<100 m deep) within a 5 km distance from the shore. The water-depth profile is shown in Figure 2c. In Figures 2a and 4c, the waves associated with event 2 are observed clearly at the first 5 km distance from the shore. They propagate approximately at an apparent velocity of 20 m/s forward with reflections backward to the shore. As shown in Figure 3b, the frequency of event 2 is higher than event 1 but lower than the maximum frequency of OSGWs ($f_{\mathrm{osgw,max}}$) calculated from equation 6. The amplitude of event 2 is bound by this maximum frequency limit in all recording channels along the cable, as shown in Figure 5b. By conforming to this frequency limit, the amplitude of event 2 decays with water depth exponentially, as described in equation 3. In Figure 6, we observe in the *f-k* domain that event 2 is generally aligned with the OSGW dispersion curve (the dashed blue line) calculated from equation 4. The small deviation of event 2 from the OSGW dispersion curve occurs when the propagating direction of an OSGW is oblique to the cable axis. Therefore, we conclude that event 2 is the dynamic loading pressure response of OSGWs excited by winds.

Because events 1 and 2 are direct responses to OSGWs, their amplitude and frequency must be affected by the tide described in equations 7 and 8, respectively. Figure 7 shows the spectrograms for three individual channels along with the tide and weather data in the study area. The maximum frequency limit of OSGWs ($f_{\mathrm{osgw\text{-}tide,max}}$) from equation 8 is plotted in red. Here, we can observe that the high-frequency OSGWs, i.e., event 2, are strongly modulated by sea-level changes caused by the tide. The variation of the amplitude and frequency in shallow water (Figure 7a) is larger than in deep water (Figure 7c). In Figure 7a, we clearly see that the spectral amplitude and the maximum frequency of OSGWs become highest at high tide (high sea level), as plotted in Figure 7d. This tidal modulation of OSGWs agrees with their maximum frequency limit defined in equation 8, which indirectly validates the dynamic pressure response in equation 7. Note that our observation here is different from Williams et al. (2022, Figure 3), in which they infer that the spectral amplitude and maximum frequency become highest during low tide with frequency-dependent phase delays affected by nonlinear wave-current interaction. We believe that their observation could be explained by equation 8 in this paper.

The energy peak at 1.0–1.2 Hz is marked as event 3 in Figures 3 and 5. Similar to event 2, event 3 can be observed only in shallow water (<100 m deep) within a 5 km distance from the shore. This implies that the amplitude of event 3 decays with water depth in a fashion similar to event 2. However, we see that the frequency of event 3 is almost invariant with water depth. Because the frequency of event 3 is not a function of water depth, event 3 does not involve seismo-acoustic wave propagation in the water layer. In addition, because its amplitude decays with water depth to a greater extent than spherical divergence, event 3 does not involve seismo-acoustic wave propagation from earthquakes or other seismic sources. Hence, event 3 may result from dynamic loading pressure on the seafloor caused by some wave motions above.

As observed in Figures 3 and 5, event 3 has a higher frequency than the maximum frequency limit of OSGWs. Therefore, event 3 is definitely not caused by an OSGW. In Figure 4b, we observe that

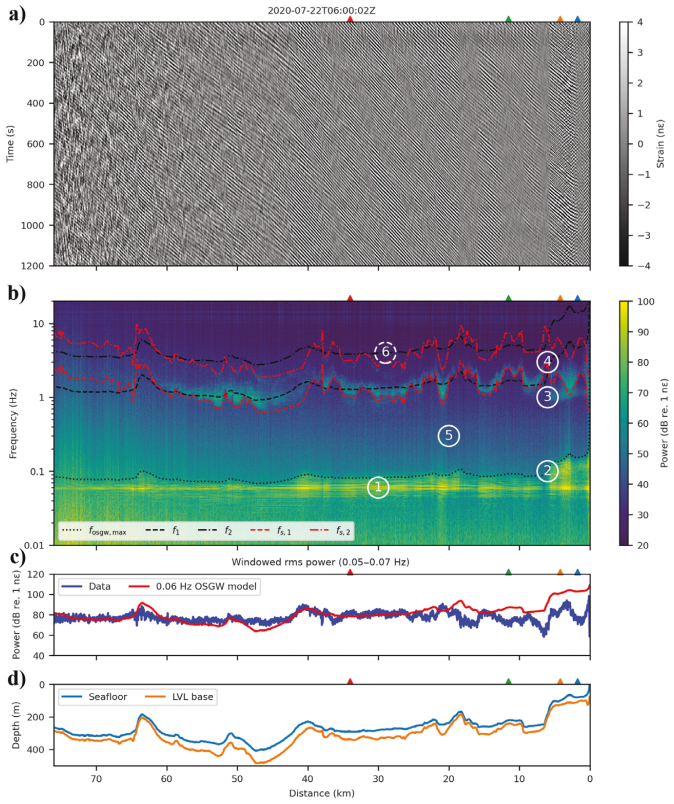

Figure 5. Frequency analysis of DAS strain data from 0 to 76 km along the cable. (a) The strain data in the 1200 s time window from 2020-07-22T06:00:02Z containing no strong seismic waves from significant earthquakes. (b) The *f-x* power spectra. (c) The rms of the power (the blue) extracted from the frequency range 0.05–0.07 Hz in the *f-x* power spectra in comparison with the modeled power (the red) for the OSGWs at 0.06 Hz. (d) The depth profile below the SWL of the seafloor and the estimated base of the LVL.

the waves associated with event 3 are scattered with unclear patterns across the time and space axes. However, we can estimate from the same figure that the apparent velocity of their diffraction tails could be as high as 200 m/s. This estimation agrees with the *f-k* spectrum shown in Figure 6c. The velocity is too high for event 3 to be interpreted as ocean surface waves or ocean currents.

One possible generating mechanism of event 3 could be an effect of the slamming pressure exerted onto the seafloor caused by turbulence in the upper ocean or ocean surface disruptions such as wave breaking. Weather and wind conditions can affect the frequency of such surface disruptions and their subsequent ocean-bottom pressure. In addition, the slamming pressure on the seafloor caused by these disruptions could be impulsive and sufficiently strong to generate seismo-acoustic waves such as P waves, S waves, and Scholte interface waves. The Scholte interface waves, which longitudinally propagate along the seafloor, can be measured by ocean-bottom DAS and have relatively high-amplitude responses (Spica et al., 2022). In addition, the apparent velocity of 200 m/s for event 3 is reasonable for the Scholte-wave velocity, which is typically on the order of 0.86 times the S-wave velocity (c_s) in the seafloor sediments if $c_s < c_w$ (Westwood et al., 1996).

Figure 7a and 7b shows the spectrograms from two channels in shallow water. We clearly see that the frequency of event 3 varies with time. Its amplitude is also strongest during strong wind conditions (high wind speed), as compared with the wind speed data, especially from the Isfjord Radio weather station in Figure 7d. Because the amplitude of event 3 is modulated with the wind speed and its apparent velocity matches with the Scholte-wave velocity at the seafloor, we believe that event 3 has a relation with the Scholte interface waves generated from the dynamic ocean-bottom loading pressure caused by wind-driven ocean surface disruptions. More detailed studies are required to verify our speculation on event 3.

Seismo-acoustic responses

Event 4 marked on the *f-x* spectra in Figures 3 and 5 is observed in all the recording channels along the cable. Its frequency is spatially variant. Event 4 is associated with harmonic wave patterns. As

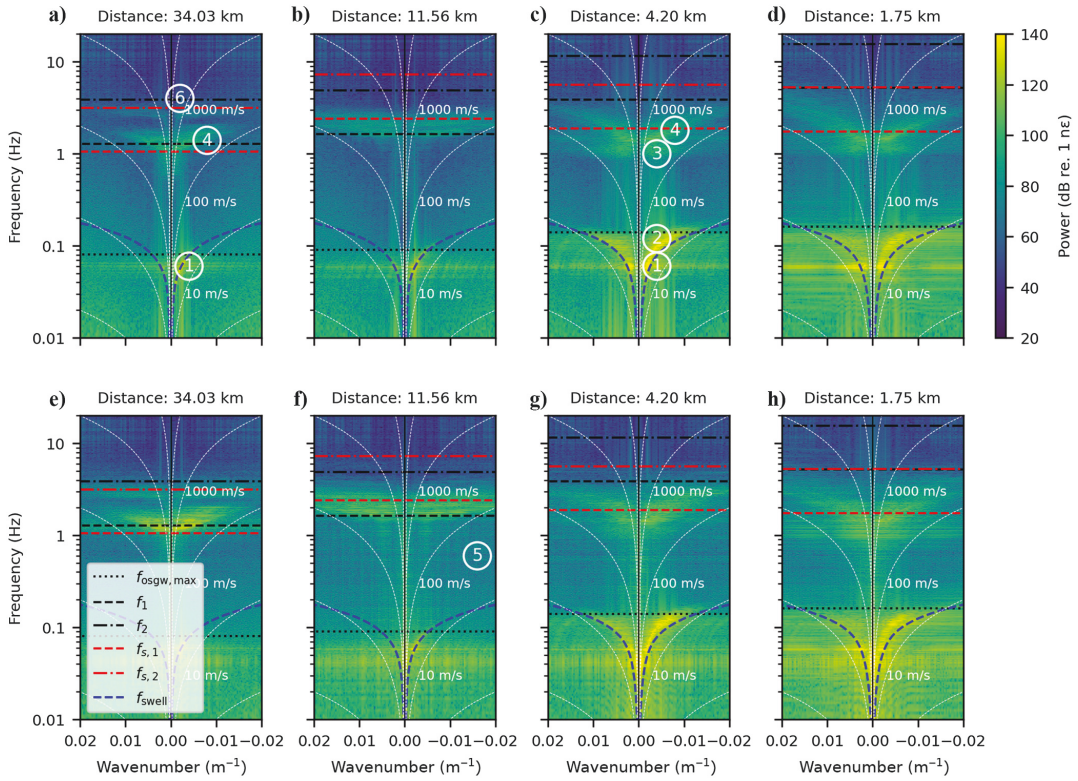

Figure 6. The *f-k* spectra of DAS strain data. (a–d) The *f-k* power spectra of the DAS recording from 2020-07-22T06:00:02Z (Figures 2a and 5a) at 34.03, 11.56, 4.20, and 1.75 km along the cable from shore, respectively, each of which is computed from the 1200 s time window over its surrounding 1001 recording channels (2 km radius). (e–h) The *f-k* power spectra of the DAS recording from 2020-07-22T06:20:02Z (Figures 2b and 8a) at the same positions and the same window sizes as for (a–d). The wavenumber $k/(2\pi)$ is referencing the cable distance from the shore in Longyearbyen: $k > 0$ for waves propagating to the west (the North Atlantic Ocean) and $k < 0$ for waves propagating to the east (the inner part of the Isfjord).

shown in Figure 5b, the first harmonic is observed in the data even in the absence of strong seismic waves from earthquakes. When strong seismic waves from the Alaska earthquake dominate the data (Figure 8a), the harmonics at the higher orders can be observed, as shown in Figure 8b. Because event 4 occurs naturally and can be enhanced by external seismic waves, we relate event 4 to normal modes driven by seismo-acoustic waves.

In Figures 5b and 8b, the first (f_1) and second (f_2) cutoff frequencies for the guided acoustic waves in the water layer are plotted as dashed black lines on the *f-x* spectra. Here, the cutoff frequencies are calculated from equation 11 using the water sound speed $c_w = 1490\,\mathrm{m/s}$ and the water-depth profile along the fiber-optic cable. In the *f-x* spectra, the energy peak associated with event 4 does not spatially conform to these water-related cutoff frequencies, especially in the shallow water within a 5 km distance from the shore. Hence, event 4 must be associated with the normal modes in a different layer than the water layer.

The time-invariant frequency of event 4 as shown in Figure 7 also confirms that event 4 is not related to normal modes in the water column, of which the thickness varies with time due to the tide. The *f-k* spectra in Figure 6 show that event 4 is dispersed and its apparent phase velocity is between 100 and 1000 m/s. From Figure 6, the apparent phase velocity approximately decreases from 1000 to 200 m/s by increasing the frequency above the cutoff frequency for S-wave modes. Because its velocity is significantly lower than the water sound speed (approximately 1490 m/s) and subsurface P-wave velocity, event 4 should involve S-wave propagation below the seafloor.

According to Albaric et al. (2021), we can expect the low-velocity layer (LVL) with an S-wave velocity of approximately 200 m/s in the upper 50 m of the near-surface sediments in Longyearbyen. A strong velocity contrast can be observed at approximately 100 m depth below the surface, in which the S-wave velocity abruptly changes from 450 to 1800 m/s within a few meters (Albaric et al., 2021, Figure 8). This velocity contrast may be interpreted as the interface between frozen and unfrozen strata in permafrost underlying most of the land surface in Svalbard. In Svalbard, there is a low probability of finding submarine permafrost, which is the relict terrestrial permafrost that was inundated when sea levels rose after the Last Glacial Maximum (Angelopoulos et al., 2020). Therefore, we would refer the strong velocity contrast below the seafloor in Svalbard to the interface between unconsolidated sediments (the LVL) and consolidated rock strata. According to Forwick and Vorren (2011), this LVL is interpreted as the shallow glacimarine sediments below the water column in the Isfjord. Because DAS is sensitive to the particle motions along the cable axis, it is likely that event 4 results from S-wave resonances corresponding to horizontally polarized shear (SH) wave propagation in the LVL.

We manually pick the first S-wave resonance frequency $f_{s,1}$ at the onset of the lower-frequency energy peak associated with event 4 in the *f-x* spectra, as shown in Figures 5b and 8b. Based on Albaric et al. (2021), we assume the LVL to be homogeneous with the constant S-wave velocity of 200 m/s. Given the first S-wave resonance frequency $f_{s,1}$ as picked and the homogeneous S-wave velocity model, we can determine the thickness H_s of the LVL from equation 13 with $n = 1$, $\nu = 0$, $c_{s,0} = 200\,\mathrm{m/s}$, and $m = -(1/2)$. As a result, we can plot the structural depths below the SWL of the seafloor (H) and the LVL base ($H + H_s$), as shown in Figures 5d and 8d. As also plotted in Figures 5b and 8b, we determine the second S-wave resonance frequency $f_{s,2}$ from equation 13 using the previously estimated LVL thickness H_s.

As discussed previously, we can use passive DAS recording to map the subsurface structure of the LVL below the seafloor. This also implies that we can delineate the base of shallow glacimarine sediments in the Arctic using the S-wave resonance observed in

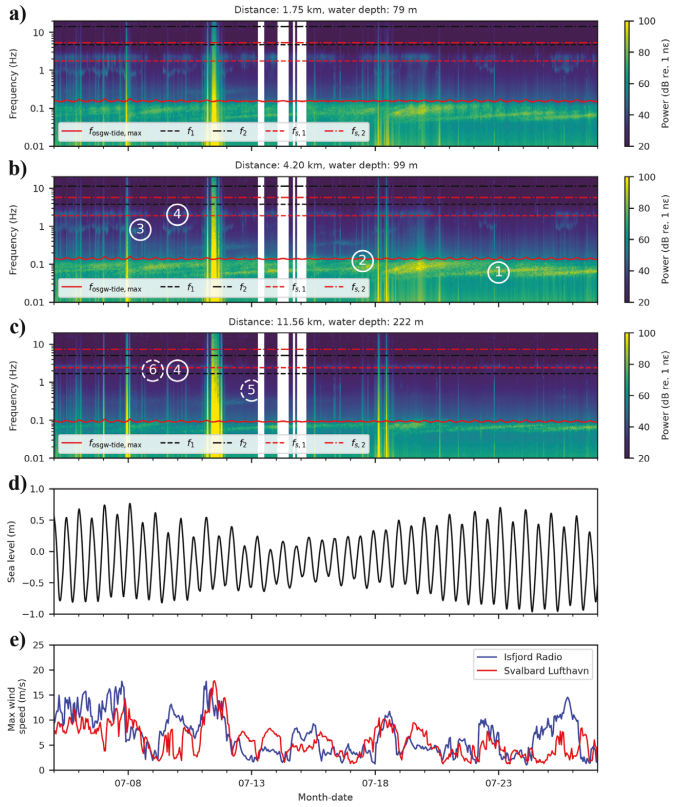

Figure 7. Spectrograms (*t-f* spectra) of the DAS strain data. Spectrograms at (a) 1.75 km, (b) 4.20 km, and (c) 11.56 km along the cable from shore. (d) Sea level in Longyearbyen (Svalbard) with respect to the average sea level during the experiment. (e) Maximum wind speeds measured at Isfjord Radio and Svalbard Lufthavn weather stations (see Figure 1c). All of the spectrograms are computed from the average power spectrum over 251 recording channels (500 m radius) around the selected locations within a 300 s time window on an hourly basis. White vertical stripes in the spectrograms indicate the dropout periods in the real-time data transfer.

DAS data. Similarly, we may use DAS to determine the structure of any other LVL such as near-surface unconsolidated sediments or weathered layers in tropical survey areas. Hence, the ocean-bottom DAS is a potential tool for exploring and characterizing the near-surface geologic structure.

In this paper, event 5 denotes ocean-bottom DAS responses to seismo-acoustic waves directly propagating from any source type such as earthquakes, cryoseisms, microseisms, seismic air guns, whales, and ship propellers. Hence, event 5 is representing seismic waves in any frequency range depending on their source types. In Figure 3a, there is a slight increase in energy of approximately 0.36 Hz marked as event 5 in the power spectra. An increase in energy of approximately 0.36 Hz has been reported as the secondary microseism associated with the 0.18 Hz opposing surface gravity wave groups in an ocean-bottom DAS experiment in Belgium by Williams et al. (2019, Figure 2). In our data, we observe no energy peak of approximately 0.18 Hz. Moreover, the 0.36 Hz energy (event 5) appears as flat low-frequency wavetrains in Figure 4b. This characteristic is obviously different from the highly dipping linear wavetrains associated with the OSGW responses (events 1 and 2) observed in Figure 4c. Therefore, it is unlikely that the 0.36 Hz energy directly involves OSGWs. In addition, its frequency is not close to the frequency limits of OSGWs, normal modes of acoustics in water, or S-wave resonances in the LVL below the seafloor. Thus, we believe that the 0.36 Hz energy shown in Figure 3a results from seismo-acoustic waves and could be marked as event 5, although we cannot identify their seismic origins.

Figure 3c and 3d shows the spectral analysis of the DAS strain data in Figure 2b that contain strong seismic waves (P, S, and SS waves) from the 22 July 2020 M_{ww} 7.8 earthquake on the Alaska Peninsula. Here, the responses caused by these seismic waves arriving at the seafloor significantly boost the strain power in all frequencies below 4 Hz. This strong seismic energy is classified as event 5, and it is superimposed on the initial ambient levels shown in Figure 3a and 3b. Figure 8a shows the seismic recording profile measured by DAS that contains strong seismic waves from the Alaska earthquake. The recorded data are similar to the horizontal component seismogram measured from the KBS seismic station in Global Seismograph Network (FDSN, 2014), which is located in Ny-Ålesund. The arrival times of the P, S, and SS waves marked in Figure 8a also agree with the KBS seismogram and the traveltimes modeled by ray tracing from the epicenter.

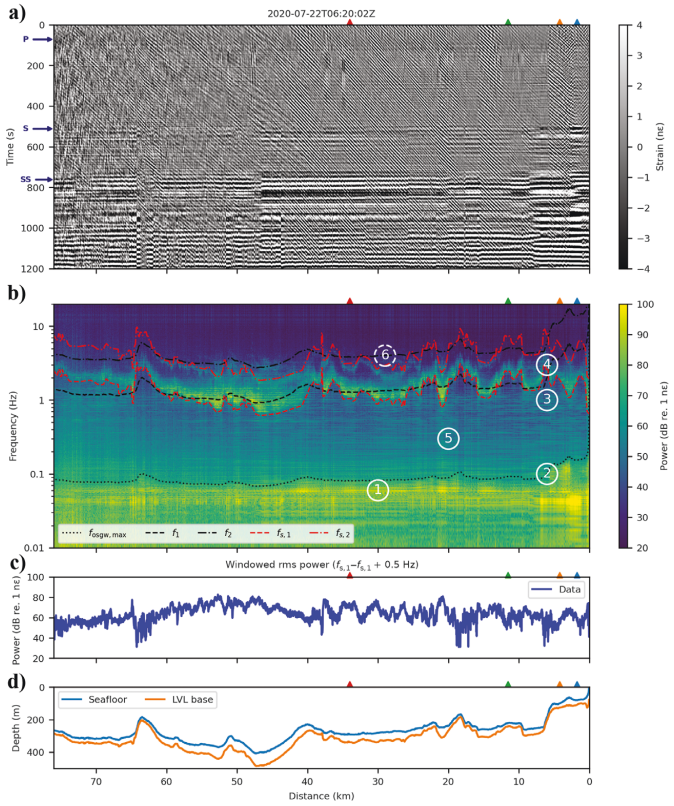

Figure 8. Frequency analysis of the DAS strain data from 0 to 76 km along the cable. (a) The strain data in the 1200 s time window from 2020-07-22T06:20:02Z containing strong seismic waves (P, S, and SS waves) from the 22 July 2020 M_{ww} 7.8 earthquake on the Alaska Peninsula. (b) The *f-x* power spectra. (c) The rms power extracted along the first S-wave resonance frequency ($f_{s,1}$) picks in the *f-x* power spectra. (d) The depth profile below the SWL of the seafloor and the estimated base of the LVL.

Figure 8a also agree with the KBS seismogram and the traveltimes modeled by ray tracing from the epicenter.

The particle motions perpendicular to the fiber-optic cable can be sensed by DAS with less sensitivity than the parallel motions (Taweesintananon et al., 2021). Hence, the normal modes of acoustic wave propagation in the water column marked as event 6 are hardly observed in all the *f-x* spectra in Figures 3, 5, and 8. Although it is much weaker than the S-wave resonance (event 4), we can see the energy peak for the first mode of the acoustics in the water column marked as event 6 in the *f-k* spectra in Figure 6a and 6e. Here, we observe that event 6 is dispersed, in which its apparent phase velocity is between 1000 and 10,000 m/s and decreases with an increasing frequency above the first cutoff frequency (f_1) for acoustic normal modes in the water column.

Ocean wave monitoring

Ocean-bottom DAS can be used for monitoring low-frequency ocean-bottom vibrations corresponding to OSGWs and, hence, ocean swells. In this section, we elaborate on our detailed analysis of the same DAS data for storm monitoring as presented by Landrø et al. (2022). Figure 9 shows spectrograms from three individual DAS recording channels at different water depths and distances from the shore. Figure 9a–9c shows the linear upsweep trends of different ocean swells ranging from 0.04 to 0.1 Hz. Their frequencies monotonically increase with time. These linear trends correspond to the ocean swells produced by distant storms. Over the entire period of recording, we can identify 12 linear trends in the spectro-

grams. Most of them last between 50 and 100 hours and can overlap in time and space.

Figure 9e shows the maximum speed of local winds measured at the Isfjord Radio and Svalbard Lufthavn weather stations near the DAS array. The Isfjord Radio station is located at the entrance of the Isfjord and close to the 55 km distance point along the DAS array, whereas the Svalbard Lufthavn station is located at the Svalbard Airport in Longyearbyen and close to the start of the DAS array (see Figure 1c). We find no correlation between the local wind speeds and the responses associated with the OSGWs. Therefore, we deduce that the OSGW responses visible in the spectrograms are mostly generated from winds or storms outside the Isfjord.

Four linear upsweep trends of the ocean swells corresponding to distant storms are highlighted in the spectrogram shown in Figure 9c. Using the procedure described in the "Methods" section, we can calculate the distance and time taken by an ocean swell to travel from each storm center to the DAS array. Although this procedure has widely been applied to many data sets measured by conventional sensors, we demonstrate it using the ocean-bottom DAS data with detailed calculations for the first time. Table 1 summarizes the calculation of the four storms marked in Figure 9c. By applying geographical and topological constraints (there must be an open seaway between our DAS array and the source of the OSGWs), we can retrieve their approximate locations for comparison with public records. The Arctic Ocean is isolated from other oceans by land. The Fram Strait, which lies between Svalbard and Greenland, is the only deep passage into the Arctic Ocean. In addition, the main orientation of our DAS array points toward the Atlantic Ocean. Therefore, the ocean swells detected by our DAS array are produced by storms in the Atlantic Ocean. It is unlikely that our DAS data are dominated by the swells caused by storms in the Pacific Ocean through the shallow Bering Strait.

From public records, we can trace all four linear trends shown in Figure 9c back to their corresponding storms in the Atlantic Ocean. Storm 1 corresponds to Tropical Storm Edouard near Bermuda at approximately 4100 km away from Longyearbyen, occurring from 4 July 2020 to 6 July 2020 (Pasch, 2021). Storm 2 possibly corresponds to the bomb cyclone in offshore south Brazil at approximately 13,000 km from Longyearbyen from 30 June 2020 to 2 July 2020, as reported by Gobato and Heidari (2020) and Khalid et al. (2020). According to weather news in Iceland (Ćirić, 2020), storm 3 should correspond to an extratropical depression between Iceland and Greenland at approximately 2400 km away from the DAS array from 15 July 2020 to 17 July 2020. Finally, storm 4 probably comes from a storm in a remote region in offshore south Brazil at approximately 11,000 km from the DAS array on 12 July 2020.

These four storms are examples of the total 12 storms observed in our data set. Many events similar to storm 4 and the stronger trend in the rightmost of the time-frequency spectra shown in Figure 9c come from remote regions in the South Atlantic Ocean between the eastern coast of South America and the western coast of Africa. As discussed by Landrø et al. (2022), the storms in these remote regions might not affect humans and, hence, not be documented. However, they are obviously detected by DAS. Thus, DAS could be a potential storm monitoring system with global coverage.

Future applications

Subsurface exploration

Ocean-bottom DAS can record seismo-acoustic vibrations in broadband frequency ranges. Taweesintananon et al. (2021) use DAS data resulting from marine impulsive seismic sources at a few hundred Hertz for subsurface seismic imaging. In addition,

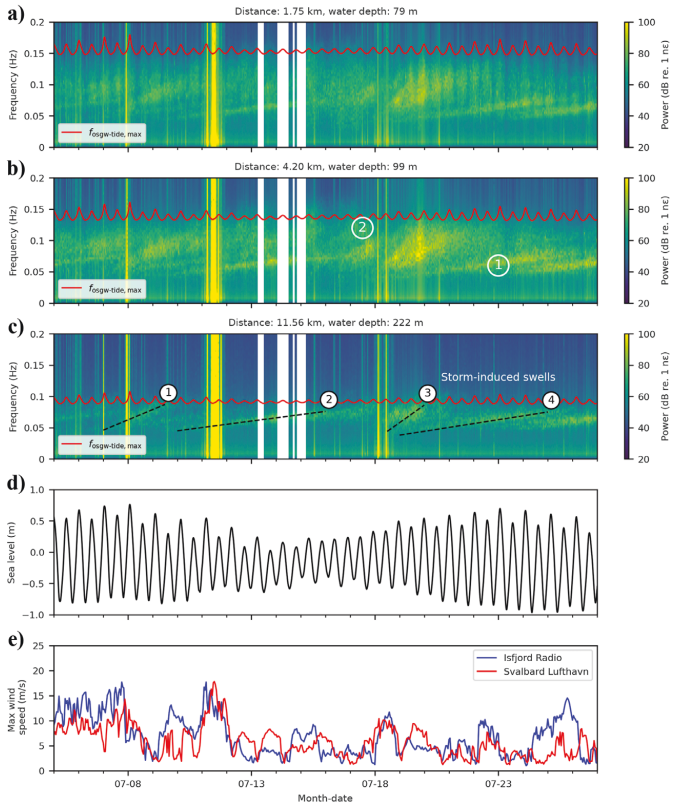

Figure 9. Spectrograms for storm monitoring. The same spectrograms as Figure 7, but with a linear scale for the vertical axes, (a) 1.75 km, (b) 4.20 km, and (c) 11.56 km along the cable from shore. (d) Sea level in Longyearbyen (Svalbard) with respect to the average sea level during the experiment. (e) Maximum wind speeds measured at Isfjord Radio and Svalbard Lufthavn weather stations (see Figure 1c). Four storm events marked in (c) are discussed in the text. All the spectrograms are computed from the average power spectrum over 251 recording channels (500 m radius) around the selected locations within a 300 s time window on an hourly basis.

Table 1. The estimated origins of the four storms producing the ocean swells marked in Figure 9c.

Parameters	Storm 1	Storm 2	Storm 3	Storm 4
Start time at DAS (t_0)	7 July 2020 T00:00:00Z	10 July 2020 T00:00:00Z	18 July 2020 T12:00:00Z	19 July 2020 T00:00:00Z
End time at DAS (t_1)	9 July 2020 T12:00:00Z	16 July 2020 T00:00:00Z	20 July 2020 T00:00:00Z	25 July 2020 T00:00:00Z
Frequency at start time (f_0) (Hz)	0.046	0.045	0.044	0.038
Frequency at end time (f_1) (Hz)	0.087	0.076	0.086	0.075
Travel distance (x in equation 14) (km)	4113	13,055	2409	10,938
Group velocity for the lowest-frequency swell (c_g in equation 15 with $f = f_0$) (m/s)	16.97	17.35	17.74	20.54
Traveltime for the lowest-frequency swell (t in equation 16) (hours)	67.32	209.03	37.71	147.89
Estimated time at source ($t_0 - t$)	4 July 2020 T04:40:00Z	1 July 2020 T06:58:00Z	16 July 2020 T22:17:00Z	12 July 2020 T20:06:00Z

Bouffaut et al. (2022) use DAS to record frequency-swept acoustic waves at a few dozen Hertz produced by whales and generate their corresponding seismic profiles for subsurface exploration. Our data characterization affirms that DAS can record high-quality, low-frequency seismo-acoustic data ranging from 0.01 to 10 Hz, as also shown in other publications (e.g., Sladen et al., 2019; Williams et al., 2019).

In subsurface seismic exploration, the seismo-acoustic waves at frequencies lower than 10 Hz are usually treated as noise to be removed in data processing. However, the waves in this low-frequency range interact with subsurface layers. We clearly see from Figure 3 that the earthquake-related waves give additional data between 0.01 and 10 Hz, in which the S-wave resonances become more pronounced. Previously, we show that the S-wave resonances can be used to determine the structure of the subsurface LVL.

Therefore, it could be possible to further apply DAS to seismic imaging using data with a frequency below 10 Hz. In addition to the higher-frequency data, we could expect more applications of DAS in making use of these low-frequency data for subsurface imaging and exploration. Examples of such applications can be found in Lior et al. (2022) and Spica et al. (2022).

Ocean observation

Functioning marine ecosystems are vital to healthy oceans on which a sustainable future on earth for all living beings ultimately depends (Danovaro et al., 2020). Marine acoustics play an important role in studying physical processes in the oceans and their interaction with the solid earth, atmosphere, and living organisms. Therefore, passive acoustic monitoring (PAM) is recognized as an important surveillance tool for the earth's ecosystems, through the studies of ocean ambient sound, marine mammal behavior, glacial/iceberg noise, anthropogenic ocean use, unsanctioned nuclear or other polluting activity, earthquake, and tsunami warning, in addition to search and rescue.

We have shown that DAS, as a PAM system, can detect waves from various sources through dynamic interactions among the atmosphere, ocean, and solid earth. It effectively measures ocean-bottom vibrations at a low frequency down to 0.01 Hz corresponding to OSGWs. Moreover, it can be used to monitor ocean currents (Williams et al., 2022). Accordingly, the sea state can indirectly be monitored by ocean-bottom DAS. Therefore, DAS has many valuable attributes to offer the oceanographic community, nicely complementing existing sensing systems such as satellites (which are broadly limited to very near-surface observations), buoys, moorings, and floats (which have limited spatial coverage and resolution). The advantages of DAS include broadband and high-resolution spatial and temporal measurement capacities, with data available in real time to support active marine management and decision-making. Its real-time capability, bringing data from the seafloor, is unmatched by any other system other than fixed installations cabled to shore or supporting long lines to surface buoys, both of which represent expensive and complex engineering challenges. The potential for earthquake and tsunami warning systems alone is therefore remarkable. This sensing network may also be created at a low cost, because we can use the existing submarine telecommunication cables. These cables span more than one million kilometers around all the oceans on the globe, potentially bringing a sensing capability to many less-sampled environments, and perhaps also able to support less developed countries in responsibly managing their maritime resources.

Thus, DAS brings an innovative and game-changing new sensing modality to oceanographic and geophysical observation systems in general. The ocean-bottom DAS can be used to monitor the sea state, which is one of the essential climate variables specified by the Global Climate Observing System (WMO, 2016). Therefore, we believe that DAS can become a valuable new component of the Global Ocean Observing System of the Intergovernmental Oceanographic Commission of UNESCO, as discussed in Howe et al. (2019).

CONCLUSION

DAS in an ocean-bottom telecommunication fiber-optic cable can measure various types of ocean-bottom vibrations that are caused by dynamics in the atmosphere, ocean, and solid earth. They comprise (1) the ocean-bottom loading pressure fluctuation corresponding to dynamics in the ocean and atmosphere and (2) the responses corresponding to seismo-acoustic wave propagation. We clearly describe and compare their characteristics in the ocean-bottom DAS data. Our interpretations are validated by redundant samples from the data that were acquired extensively in spatial and temporal dimensions, over 44 days along 120 km of a submarine

fiber-optic cable, extending along the Isfjord in Longyearbyen, Svalbard, across different water depths from 0 to 400 m.

In the ocean-bottom DAS data, we observe the signals associated with OSGWs originating from winds and distant storms, together with their reflections at Longyearbyen's shore in shallow water. This observation enables us to trace several responses of ocean swells back to their origins of distant storms in the South Atlantic Ocean up to 13,000 km away from the DAS array in Svalbard. Moreover, we demonstrate a DAS application for near-surface structural mapping using the recorded S-wave resonances. Hence, we may use DAS to delineate the base of the LVL, which is shallow glacimarine sediments in the Arctic. Thanks to its high spatial and temporal resolution, real-time data availability, broadband low-frequency sensitivity, and ability to sense what is happening close to the seafloor, capturing ocean surface waves and seismo-acoustic events, DAS offers great scientific value to observation systems for the earth and the oceans.

ACKNOWLEDGMENTS

The authors acknowledge the Research Council of Norway and the sponsors of the Geophysics and Applied Mathematics in Exploration and Safe production project (GAMES; grant no. 294404), the Digimon ACT project (grant no. 305075), and the Centre for Geophysical Forecasting (CGF; grant no. 309960) at NTNU for financial support. The authors thank Alcatel Submarine Networks Norway AS for supporting and operating the OptoDAS interrogator, and Uninett AS for providing access to their fiber-optic cable between Longyearbyen and Ny-Ålesund and operating the data transfer through their network between Svalbard and Trondheim. The authors thank T. C. Netland and D. Bergh for their technical support on the real-time data transfer. The authors acknowledge E. F. Williams and H. Dong for constructive feedback and discussion on the data characterization.

AUTHOR CONTRIBUTIONS

M. Landrø, S. E. Johansen, J. K. Brenne, A. Haukanes, O. Schjelderup, and F. Storvik conceived and designed the experiment. A. Haukanes and F. Storvik collected the data. K. Taweesintananon processed the data and prepared the visualizations. K. Taweesintananon and M. Landrø analyzed the data with support from J. R. Potter, S. E. Johansen, R. A. Rørstadbotnen, L. Bouffaut, and H. J. Kriesell. M. Landrø and J. R. Potter validated the research outputs, acquired the funding, and managed the project. K. Taweesintananon wrote the original draft of the manuscript. All the authors conducted the review and editing of the manuscript.

COMPETING INTERESTS

Author K. Taweesintananon is employed by PTT Exploration and Production Public Company Limited. Author J. K. Brenne is, and author A. Haukanes was, employed by Alcatel Submarine Networks Norway AS. Authors O. Schjelderup and F. Storvik are employed by Uninett AS (merged into Sikt in January 2022). The remaining authors declare that the research was conducted in the absence of any commercial or financial relationships that could be construed as a potential conflict of interest.

DATA AND MATERIALS AVAILABILITY

The DAS data for this research are available in Taweesintananon and Landrø (2022) via https://doi.org/10.18710/VPRD2H. The seismic data from the KBS seismic station in Svalbard used as our reference are available through the IRIS web services: https://service.iris.edu/. Details on the 22 July 2020 M_{ww} 7.8 earthquake on the Alaska Peninsula are available at the USGS website: https://earthquake.usgs.gov/earthquakes/eventpage/us7000asvb/executive. The weather data are available through the Norwegian Center for Climate Services at https://seklima.met.no/observations/. The tidal data at Longyearbyen (Svalbard) are available through the Norwegian Mapping Authority, Hydrographic Service at https://www.kartverket.no/en/at-sea/se-havniva.

REFERENCES

Abolfazli, E., J. Liang, Y. Fan, Q. J. Chen, N. D. Walker, and J. Liu, 2020, Surface gravity waves and their role in ocean-atmosphere coupling in the Gulf of Mexico: Journal of Geophysical Research: Oceans, **125**, e2018JC014820, doi: 10.1029/2018JC014820.

Airy, G. B., 1841, Tides and waves, *in* H. J. Rose, et al., eds., Encyclopaedia Metropolitana (1817–1845): Mixed Sciences, 3, 241–396.

Albaric, J., D. Kühn, M. Ohrnberger, N. Langet, D. Harris, U. Polom, I. Lecomte, and G. Hillers, 2021, Seismic monitoring of permafrost in Svalbard, Arctic Norway: Seismological Research Letters, **92**, 2891–2904, doi: 10.1785/0220200470.

Angelopoulos, M., P. P. Overduin, F. Miesner, M. N. Grigoriev, and A. A. Vasiliev, 2020, Recent advances in the study of Arctic submarine permafrost: Permafrost and Periglacial Processes, **31**, 442–453, doi: 10.1002/ppp.2061.

Ardhuin, F., J. E. Stopa, B. Chapron, F. Collard, R. Husson, R. E. Jensen, J. Johannessen, A. Mouche, M. Passaro, G. D. Quartly, V. Swail, and I. Young, 2019, Observing sea states: Frontiers in Marine Science, **6**, 124, doi: 10.3389/fmars.2019.00124.

Barthelemy, X., M. L. Banner, W. L. Peirson, F. Fedele, M. Allis, and F. Dias, 2018, On a unified breaking onset threshold for gravity waves in deep and intermediate depth water: Journal of Fluid Mechanics, **841**, 463–488, doi: 10.1017/jfm.2018.93.

Bigg, G. R., and E. Hanna, 2016, Impacts and effects of ocean warming on the weather, *in* D. Laffoley and J. M. Baxter, eds., Explaining ocean warming: Causes, scale, effects and consequences: IUCN, 359–372, doi: 10.2305/IUCN.CH.2016.08.en.

Bouffaut, L., K. Taweesintananon, H. J. Kriesell, R. Rørstadbotnen, J. R. Potter, M. Landrø, S. E. Johansen, J. K. Brenne, A. Haukanes, O. Schjelderup, and F. Storvik, 2022, Eavesdropping at the speed of light: Distributed acoustic sensing of baleen whales in the Arctic: Frontiers in Marine Science, **9**, 901348, doi: 10.3389/fmars.2022.901348.

Bromirski, P. D., and F. K. Duennebier, 2002, The near-coastal microseism spectrum: Spatial and temporal wave climate relationships: Journal of Geophysical Research: Solid Earth, **107**, 2166, doi: 10.1029/2001JB000265.

Cavaleri, L., B. Fox-Kemper, and M. Hemer, 2012, Wind waves in the coupled climate system: Bulletin of the American Meteorological Society, **93**, 1651–1661, doi: 10.1175/BAMS-D-11-00170.1.

Ćirić, J., 2020, Weather warning for Central Highland, Northwest Iceland: Iceland Review, https://www.icelandreview.com/travel/weather-warning-for-central-highland-northwest-iceland/.

Coastal Engineering Research Center, 1984, Shore protection manual, 4th ed.: U.S. Army Engineer Waterways Experiment Station, 1.

Craik, A. D., 2004, The origins of water wave theory: Annual Review of Fluid Mechanics, **36**, 1–28, doi: 10.1146/annurev.fluid.36.050802.122118.

Crawford, W. C., S. C. Webb, and J. A. Hildebrand, 1991, Seafloor compliance observed by long-period pressure and displacement measurements: Journal of Geophysical Research: Solid Earth, **96**, 16151–16160, doi: 10.1029/91JB01577.

Danovaro, R., E. Fanelli, J. Aguzzi, D. Billett, L. Carugati, C. Corinaldesi, A. Dell'Anno, K. Gjerde, A. J. Jamieson, S. Kark, C. McClain, L. Levin, N. Levin, E. Ramirez-Llodra, H. Ruhl, C. R. Smith, P. V. R. Snelgrove, L. Thomsen, C. L. Van Dover, and M. Yasuhara, 2020, Ecological variables for developing a global deep-ocean monitoring and conservation strategy: Nature Ecology & Evolution, **4**, 181–192, doi: 10.1038/s41559-019-1091-z.

European Cooperation in Science and Technology Action 714, Working Group 3, 2005, Measuring and analysing the directional spectra of ocean waves: EU Publications Office.

FDSN, 2014, IU: Global seismograph network, doi: 10.7914/SN/IU.

Forwick, M., and T. O. Vorren, 2011, Stratigraphy and deglaciation of the Isfjorden area, Spitsbergen: Norwegian Journal of Geology, **90**, 163–179.
Gobato, R., and A. Heidari, 2020, Cyclone bomb hits Southern Brazil in 2020: Journal of Atmospheric Science Research, **3**, 8–12, doi: 10.30564/jasr.v3i3.2163.
Godin, O. A., and D. M. F. Chapman, 1999, Shear-speed gradients and ocean seismo-acoustic noise resonances: The Journal of the Acoustical Society of America, **106**, 2367–2382, doi: 10.1121/1.428074.
Godin, O. A., T. J. Deal, and H. Dong, 2021, Physics-based characterization of soft marine sediments using vector sensors: The Journal of the Acoustical Society of America, **149**, 49–61, doi: 10.1121/10.0002975.
Hartog, A. H., 2017, An introduction to distributed optical fibre sensors, 1st ed.: CRC Press.
Howe, B. M., J. Miksis-Olds, E. Rehm, H. Sagen, P. F. Worcester, and G. Haralabus, 2019, Observing the oceans acoustically: Frontiers in Marine Science, **6**, 426, doi: 10.3389/fmars.2019.00426.
Jensen, F. B., W. A. Kuperman, M. B. Porter, and H. Schmidt, 2011, Computational ocean acoustics, 2nd ed.: Springer, Modern Acoustics and Signal Processing.
Kakinuma, T., and Y. Kusuhara, 2022, A 3D numerical study on tsunamis ascending a river: Coastal Engineering Journal, **64**, 272–284, doi: 10.1080/21664250.2021.2015199.
Khalid, A., A. D. S. de Lima, F. Cassalho, T. Miesse, and C. Ferreira, 2020, Hydrodynamic and wave responses during storm surges on the Southern Brazilian coast: A real-time forecast system: Water, **12**, 3397, doi: 10.3390/w12123397.
Landrø, M., L. Bouffaut, H. J. Kriesell, J. R. Potter, R. A. Rørstadbotnen, K. Taweesintananon, S. E. Johansen, J. K. Brenne, A. Haukanes, O. Schjelderup, and F. Storvik, 2022, Sensing whales, storms, ships and earthquakes using an Arctic fibre optic cable: Scientific Reports, **12**, 19226, doi: 10.1038/s41598-022-23606-x.
Landrø, M., and P. Hatchell, 2012, Normal modes in seismic data — Revisited: Geophysics, **77**, no. 4, W27–W40, doi: 10.1190/geo2011-0094.1.
Lin, J., S. Fang, X. Li, R. Wu, and H. Zheng, 2018, Seismological observations of ocean swells induced by typhoon Megi using dispersive microseisms recorded in coastal areas: Remote Sensing, **10**, 1437, doi: 10.3390/rs10091437.
Lindsey, N. J., T. C. Dawe, and J. B. Ajo-Franklin, 2019, Illuminating seafloor faults and ocean dynamics with dark fiber distributed acoustic sensing: Science, **366**, 1103–1107, doi: 10.1126/science.aay5881.
Lior, I., E. D. Mercerat, D. Rivet, A. Sladen, and J. Ampuero, 2022, Imaging an underwater basin and its resonance modes using optical fiber distributed acoustic sensing: Seismological Research Letters, **93**, 1573–1584, doi: 10.1785/0220210349.
Lior, I., A. Sladen, D. Mercerat, J.-P. Ampuero, D. Rivet, and S. Sambolian, 2021, Strain to ground motion conversion of distributed acoustic sensing data for earthquake magnitude and stress drop determination: Solid Earth, **12**, 1421–1442, doi: 10.5194/se-12-1421-2021.
Mitsuyasu, H., 2002, A historical note on the study of ocean surface waves: Journal of Oceanography, **58**, 109–120, doi: 10.1023/A:1015880802272.
Munk, W. H., 1950, On the wind-driven ocean circulation: Journal of Atmospheric Sciences, **7**, 80–93, doi: 10.1175/1520-0469(1950)007<0080:OTWDOC>2.0.CO;2.
Munk, W. H., G. R. Miller, F. E. Snodgrass, N. F. Barber, and G. E. R. Deacon, 1963, Directional recording of swell from distant storms: Philosophical Transactions of the Royal Society of London. Series A, Mathematical and Physical Sciences, **255**, 505–584, doi: 10.1098/rsta.1963.0011.
Părău, E. I., J.-M. Vanden-Broeck, and M. J. Cooker, 2005, Three-dimensional gravity-capillary solitary waves in water of finite depth and related problems: Physics of Fluids, **17**, 122101, doi: 10.1063/1.2140020.
Pasch, R. J., 2021, National hurricane center tropical cyclone report: Tropical storm Edouard (AL052020): Technical Report, National Oceanic and Atmospheric Administration.
Perlin, M., W. Choi, and Z. Tian, 2013, Breaking waves in deep and intermediate waters: Annual Review of Fluid Mechanics, **45**, 115–145, doi: 10.1146/annurev-fluid-011212-140721.
Rauch, D., 1980, Seismic interface waves in coastal waters: A review: Technical Report SACLANTCEN Report SR-42, North Atlantic Treaty Organization, Italy.
Robein, E., 2010, Velocities, time-imaging and depth-imaging: Principles and methods, 3rd ed.: EAGE.
Robertson, B., K. Hall, R. Zytner, and I. Nistor, 2013, Breaking waves: Review of characteristic relationships: Coastal Engineering Journal, **55**, 1350002, doi: 10.1142/S0578563413500022.
Schmitt, R. W., 2018, The ocean's role in climate: Oceanography, **31**, 32–40, doi: 10.5670/oceanog.2018.225.
Schwardt, M., C. Pilger, P. Gaebler, P. Hupe, and L. Ceranna, 2022, Natural and anthropogenic sources of seismic, hydroacoustic, and infrasonic waves: Waveforms and spectral characteristics (and their applicability for sensor calibration): Surveys in Geophysics, **43**, 1265–1361, doi: 10.1007/s10712-022-09713-4.
Sladen, A., D. Rivet, J. P. Ampuero, L. De Barros, Y. Hello, G. Calbris, and P. Lamare, 2019, Distributed sensing of earthquakes and ocean-solid earth interactions on seafloor telecom cables: Nature Communications, **10**, 5777, doi: 10.1038/s41467-019-13793-z.
Spica, Z. J., J. C. Castellanos, L. Viens, K. Nishida, T. Akuhara, M. Shinohara, and T. Yamada, 2022, Subsurface imaging with ocean-bottom distributed acoustic sensing and water phases reverberations: Geophysical Research Letters, **49**, e2021GL095287, doi: 10.1029/2021GL095287.
Stephen, R. A., F. N. Spiess, J. A. Collins, J. A. Hildebrand, J. A. Orcutt, K. R. Peal, F. L. Vernon, and F. B. Wooding, 2003, Ocean seismic network pilot experiment: Geochemistry, Geophysics, Geosystems, **4**, 1092, doi: 10.1029/2002GC000485.
Stommel, H., 1948, The westward intensification of wind-driven ocean currents: Eos, Transactions American Geophysical Union, **29**, 202–206, doi: 10.1029/TR029i002p00202.
Stull, R., 2017, Practical meteorology: An algebra-based survey of atmospheric science, version 1.02b ed.: University of British Columbia.
Sverdrup, H. U., 1947, Wind-driven currents in a Baroclinic Ocean; with application to the equatorial currents of the Eastern Pacific: Proceedings of the National Academy of Sciences, **33**, 318–326, doi: 10.1073/pnas.33.11.318.
Taweesintananon, K., and M. Landrø, 2022, Replication data for DAS4Microseism — Svalbard distributed acoustic sensing (DAS) strain data for oceanographic study: DataverseNO, V1, doi: 10.18710/VPRD2H.
Taweesintananon, K., M. Landrø, J. K. Brenne, and A. Haukanes, 2021, Distributed acoustic sensing for near-surface imaging using submarine telecommunication cable: A case study in the Trondheimsfjord, Norway: Geophysics, **86**, no. 5, B303–B320, doi: 10.1190/geo2020-0834.1.
Villas Bôas, A. B., F. Ardhuin, A. Ayet, M. A. Bourassa, P. Brandt, B. Chapron, B. D. Cornuelle, J. T. Farrar, M. R. Fewings, B. Fox-Kemper, S. T. Gille, C. Gommenginger, P. Heimbach, M. C. Hell, Q. Li, M. R. Mazloff, S. T. Merrifield, A. Mouche, M. H. Rio, E. Rodriguez, J. D. Shutler, A. C. Subramanian, E. J. Terrill, M. Tsamados, C. Ubelmann, and E. van Sebille, 2019, Integrated observations of global surface winds, currents, and waves: Requirements and challenges for the next decade: Frontiers in Marine Science, **6**, 425, doi: 10.3389/fmars.2019.00425.
Waagaard, O. H., E. Rønnekleiv, A. Haukanes, F. Stabo-Eeg, D. Thingbø, S. Forbord, S. E. Aasen, and J. K. Brenne, 2021, Real-time low noise distributed acoustic sensing in 171 km low loss fiber: OSA Continuum, **4**, 688–701, doi: 10.1364/OSAC.408761.
Webb, S. C., 1998, Broadband seismology and noise under the ocean: Reviews of Geophysics, **36**, 105–142, doi: 10.1029/97RG02287.
Westwood, E. K., C. T. Tindle, and N. R. Chapman, 1996, A normal mode model for acousto-elastic ocean environments: The Journal of the Acoustical Society of America, **100**, 3631–3645, doi: 10.1121/1.417226.
Williams, E. F., M. R. Fernández-Ruiz, R. Magalhaes, R. Vanthillo, Z. Zhan, M. González-Herráez, and H. F. Martins, 2019, Distributed sensing of microseisms and teleseisms with submarine dark fibers: Nature Communications, **10**, 5778, doi: 10.1038/s41467-019-13262-7.
Williams, E. F., Z. Zhan, H. F. Martins, M. R. Fernández-Ruiz, S. Martín-López, M. González-Herráez, and J. Callies, 2022, Surface gravity wave interferometry and ocean current monitoring with ocean-bottom DAS: Journal of Geophysical Research: Oceans, **127**, e2021JC018375, doi: 10.1029/2021JC018375.
WMO, 2016, The global observing system for climate: Implementation needs: Technical Report GCOS-200 (GOOS-214), World Meteorological Organization.
Wu, L., Ø. Breivik, and A. Rutgersson, 2019, Ocean-wave-atmosphere interaction processes in a fully coupled modeling system: Journal of Advances in Modeling Earth Systems, **11**, 3852–3874, doi: 10.1029/2019MS001761.
Wunsch, C., 2021, The rise of dynamical oceanography — A fragmentary historical note: The Stommel-Munk correspondence, 1947–1953: Oceanography, **34**, 249–253, doi: 10.5670/oceanog.2021.101.
Yang, X., and K. Cai, 2022, Limitations of the Yang's breaking wave force formula and its improvement under a wider range of breaker conditions: Open Geosciences, **14**, 1538–1546, doi: 10.1515/geo-2022-0445.
You, Z.-J., 2008, A close approximation of wave dispersion relation for direct calculation of wavelength in any coastal water depth: Applied Ocean Research, **30**, 113–119, doi: 10.1016/j.apor.2008.08.001.
Zhan, Z., M. Cantono, V. Kamalov, A. Mecozzi, R. Müller, S. Yin, and J. C. Castellanos, 2021, Optical polarization-based seismic and water wave sensing on transoceanic cables: Science, **371**, 931–936, doi: 10.1126/science.abe6648.

Biographies and photographs of the authors are not available.

Paper IV

Citation information:

K. Taweesintananon, M. Landrø, S. Narongsirikul and P. G. Folstad, 'Angle-dependent 4D seismic time-strain inversion for estimating subsurface thickness and velocity changes,' en, Unpublished manuscript, Trondheim, Norway, 2023

Summary:

Taweesintananon et al. propose a method to estimate thickness and velocity strains simultaneously from angle-dependent 4D seismic time strains. The method is applicable for elliptical vertical transverse isotropic (VTI) media.

Contributions:

K.T. conceived and designed the research methods. S.N. and P.G.F. collected field data. K.T. processed the data and prepared the visualisations. K.T. and M.L. analysed the data with support from S.N. and P.G.F. M.L. validated the research outputs, acquired funding, and managed the project. K.T. wrote the original draft of the manuscript. All the authors reviewed and edited the manuscript.

About the Author

Kittinat Taweesintananon received a B.Sc. (2009) in physics from Chulalongkorn University, Thailand, and an M.S. (2011) in geophysics from Stanford University, USA. Since 2009, he has been a geophysicist at PTT Exploration and Production Public Company Limited (PTTEP), where he worked as a seismic processing QC representative and a seismic processing geophysicist. In 2020, he also joined the Norwegian University of Science and Technology (NTNU) as a Ph.D. candidate. His research interests include seismic data acquisition, seismic imaging, time-lapse (4D) seismic analysis, and geophysical applications of fibre-optic distributed acoustic sensing (DAS). He is a member of the Society of Exploration Geophysicists (SEG) and the European Association of Geoscientists & Engineers (EAGE).

ISBN 978-82-326-7260-8 (printed ver.)
ISBN 978-82-326-7259-2 (electronic ver.)
ISSN 1503-8181 (printed ver.)
ISSN 2703-8084 (online ver.)

NTNU

Norwegian University of
Science and Technology